UCRL-ID-140313-APP

The $^{235}U(n,2n\gamma)$ Yrast Partial Gamma-Ray Cross Sections: A Report on the 1998 – 1999 GEANIE Data and Analysis Techniques Appendix

W. Younes, J. A. Becker, L. A. Bernstein, P. E. Garrett, C. A. Mc Grath, D. P. McNabb, R. O. Nelson, M. Devlin, N. Fotiades, and G. D. Johns

U.S. Department of Energy

Lawrence Livermore National Laboratory

September 1, 2000

Approved for public release; further dissemination unlimited

DISCLAIMER

This document was prepared as an account of work sponsored by an agency of the United States Government. Neither the United States Government nor the University of California nor any of their employees, makes any warranty, express or implied, or assumes any legal liability or responsibility for the accuracy, completeness, or usefulness of any information, apparatus, product, or process disclosed, or represents that its use would not infringe privately owned rights. Reference herein to any specific commercial product, process, or service by trade name, trademark, manufacturer, or otherwise, does not necessarily constitute or imply its endorsement, recommendation, or favoring by the United States Government or the University of California. The views and opinions of authors expressed herein do not necessarily state or reflect those of the United States Government or the University of California, and shall not be used for advertising or product endorsement purposes.

This work was performed under the auspices of the U. S. Department of Energy by the University of California, Lawrence Livermore National Laboratory under Contract No. W-7405-Eng-48.

This report has been reproduced directly from the best available copy.

Available electronically at http://www.doc.gov/bridge

Available for a processing fee to U.S. Department of Energy
And its contractors in paper from
U.S. Department of Energy
Office of Scientific and Technical Information
P.O. Box 62
Oak Ridge, TN 37831-0062
Telephone: (865) 576-8401
Facsimile: (865) 576-5728
E-mail: reports@adonis.osti.gov

Available for the sale to the public from
U.S. Department of Commerce
National Technical Information Service
5285 Port Royal Road
Springfield, VA 22161
Telephone: (800) 553-6847
Facsimile: (703) 605-6900
E-mail: orders@ntis.fedworld.gov
Online ordering: http://www.ntis.gov/ordering.htm

OR

Lawrence Livermore National Laboratory
Technical Information Department's Digital Library
http://www.llnl.gov/tid/Library.html

The $^{235}U(n,2n\gamma)$ Yrast Partial Gamma-Ray Cross Sections:

A Report on the 1998 – 1999 GEANIE Data and Analysis Techniques

W. Younes, J.A. Becker, L.A. Bernstein, P.E. Garrett,. C.A. Mc Grath*, D.P. McNabb
Lawrence Livermore National Laboratory, Livermore, CA 94551-0808
**Present address: Idaho National Engineering and Environmental Lab, Idaho Falls, ID 83415*

R.O. Nelson, M. Devlin, N. Fotiades, G.D. Johns
Los Alamos National Laboratory, Los Alamos, NM 87545-1663

Appendix

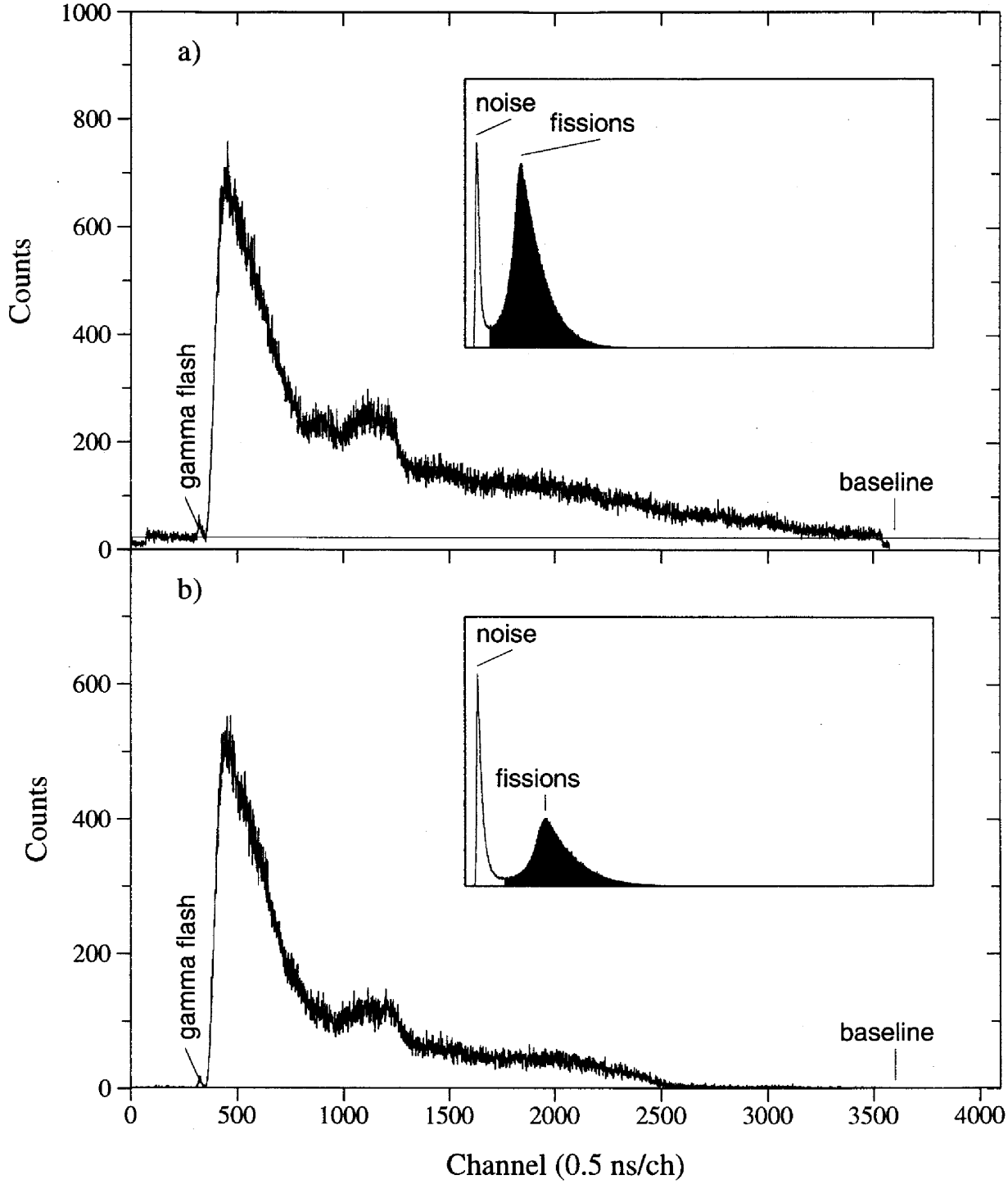

FIG. 3: TOF spectra for a) ^{235}U and b) ^{238}U fission foils from 1998 thin-target data. The baseline background, deduced from the "random" TOF region (before the gamma flash) is drawn and labeled in each case. The baseline is negligible in the case of the ^{238}U foil. The inset shows the pulse-height spectra for the fission foils and the range used to generate the corresponding TOF spectrum is shaded in red.

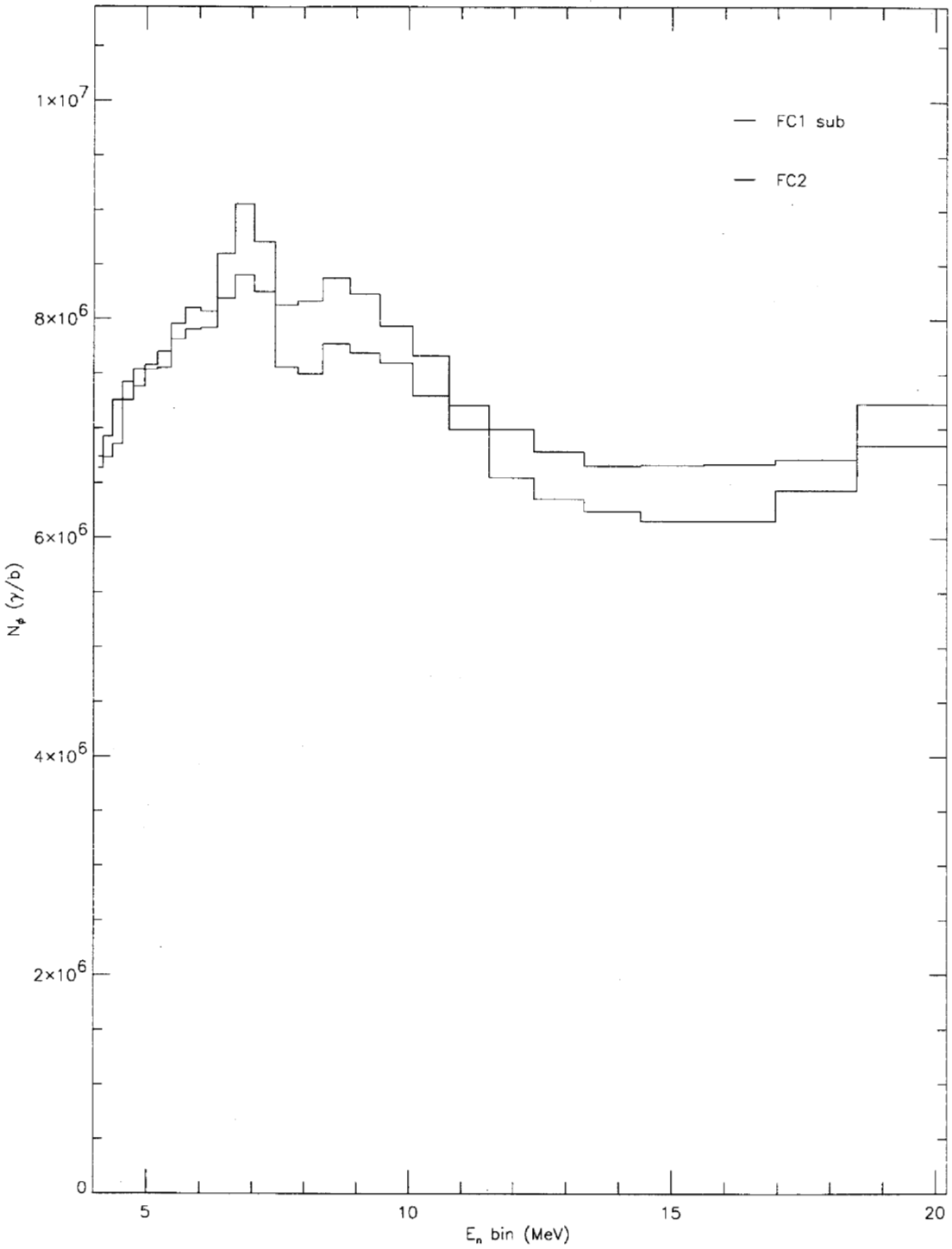

FIG. 4: Comparison between the flux normalizations N_ϕ deduced from the ^{235}U foil with baseline subtraction (denoted by "FC1 sub") and from the ^{238}U without baseline subtraction (denoted by "FC2").

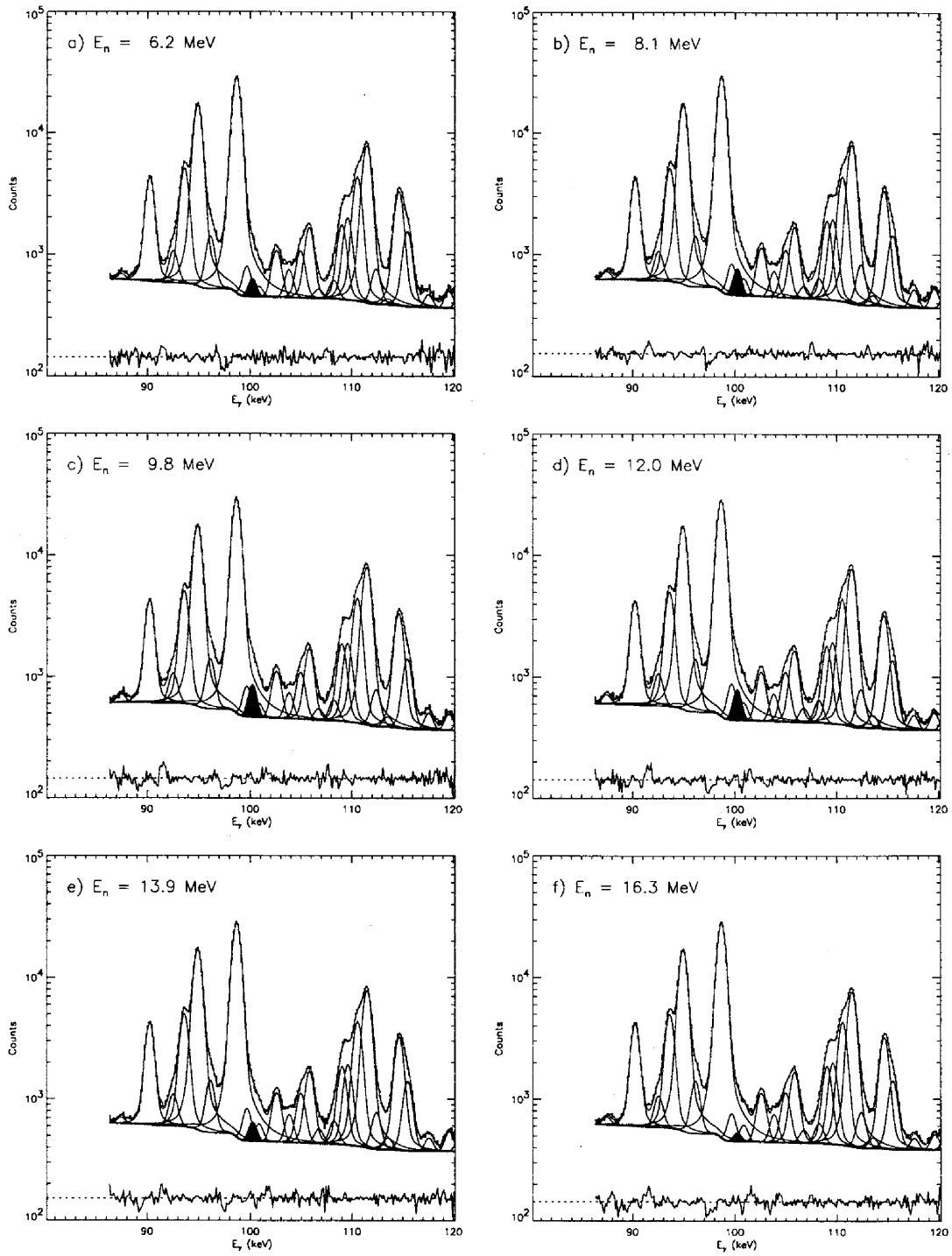

FIG. 6: Fits for the ^{234}U $4_1^+ \rightarrow 2_1^+$ transition in selected neutron-energy cuts of the GEANIE 1998 thin-target data. The $4_1^+ \rightarrow 2_1^+$ peak is shaded in red. The relative fit residual is plotted on an arbitrary scale.

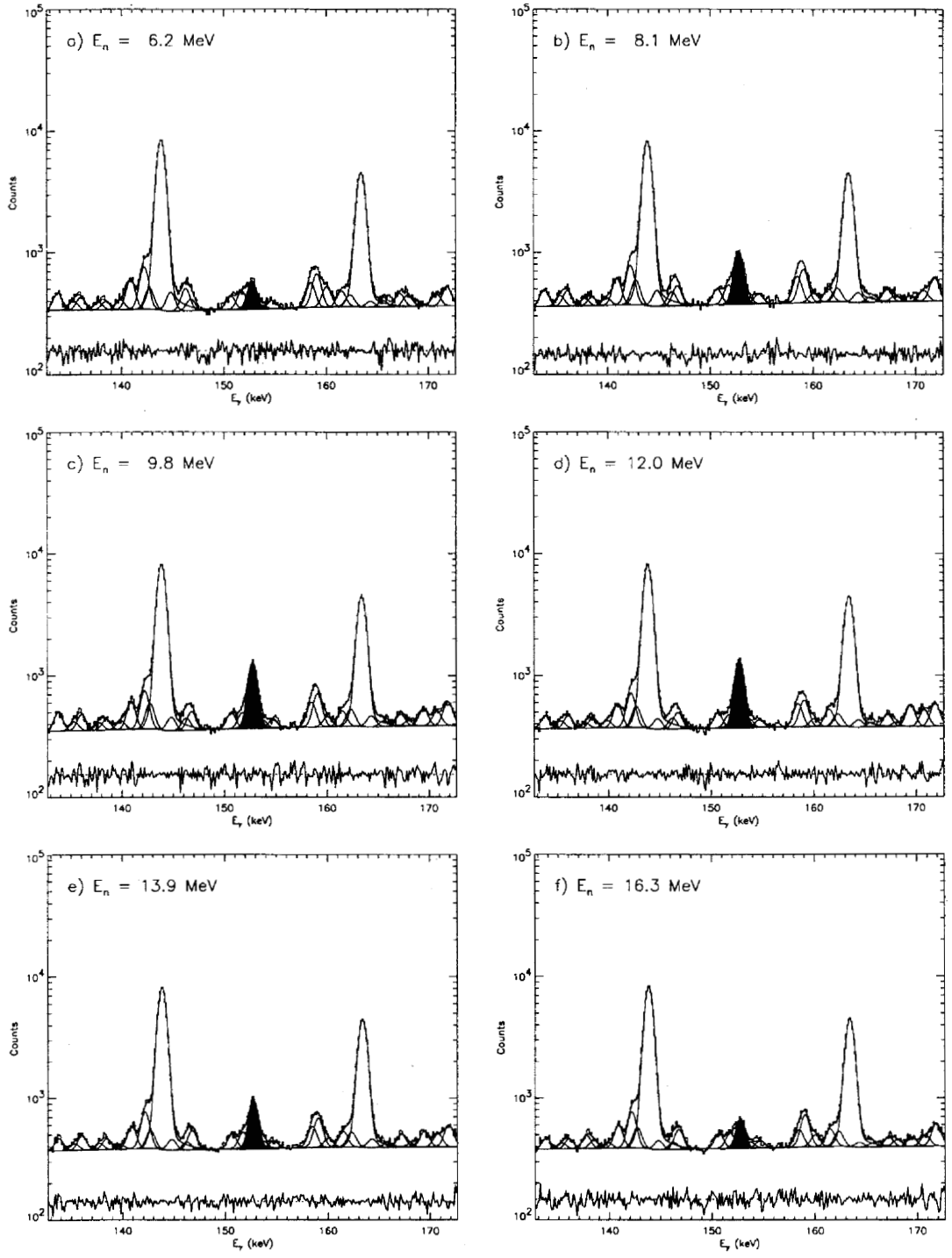

FIG. 7: Fits for the ^{234}U $6_1^+ \rightarrow 4_1^+$ transition in selected neutron-energy cuts of the GEANIE 1998 thin-target data. The $6_1^+ \rightarrow 4_1^+$ peak is shaded in red. The relative fit residual is plotted on an arbitrary scale.

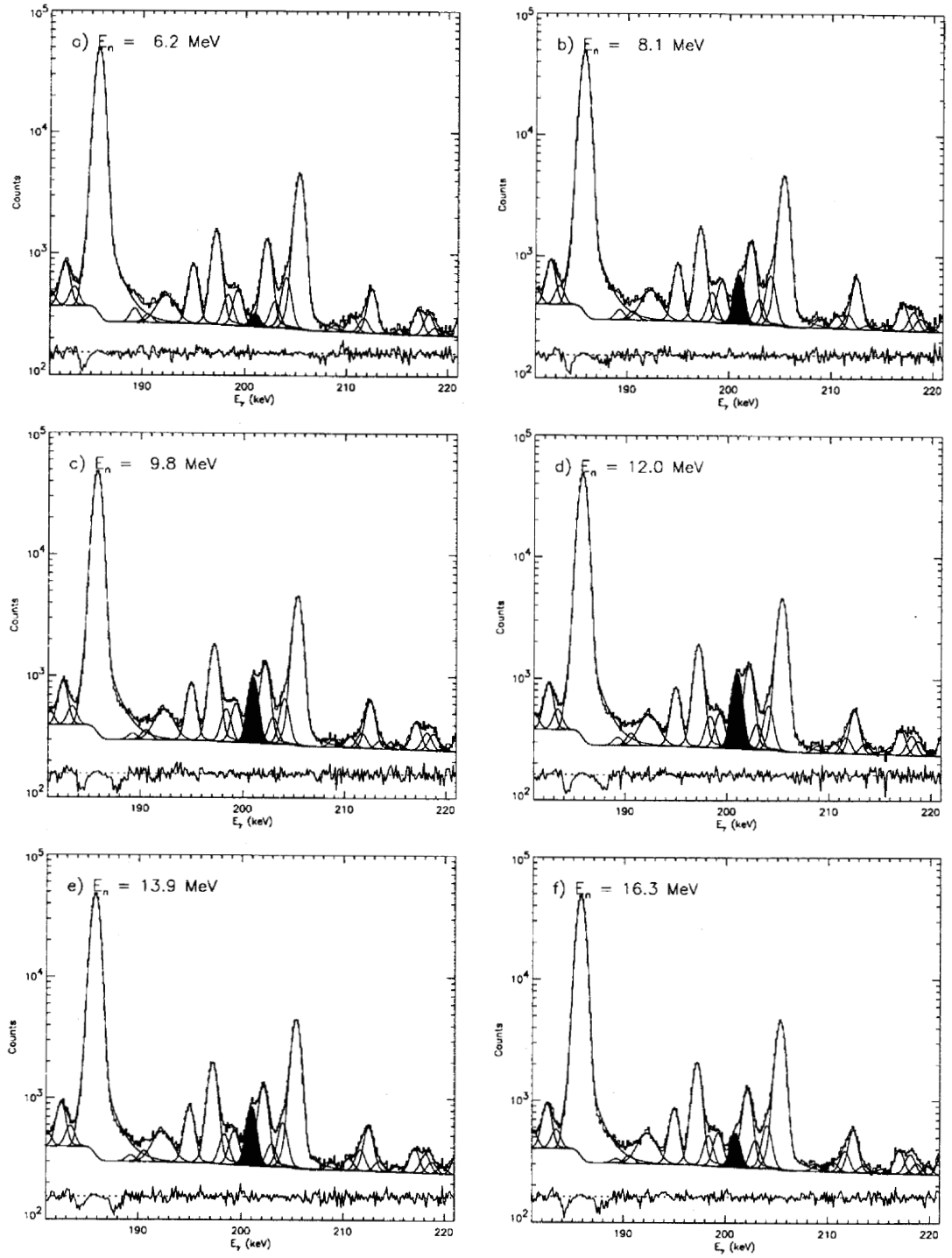

FIG. 8: Fits for the ^{234}U $8_1^+ \rightarrow 6_1^+$ transition in selected neutron-energy cuts of the GEANIE 1998 thin-target data. The $8_1^+ \rightarrow 6_1^+$ peak is shaded in red. The relative fit residual is plotted on an arbitrary scale.

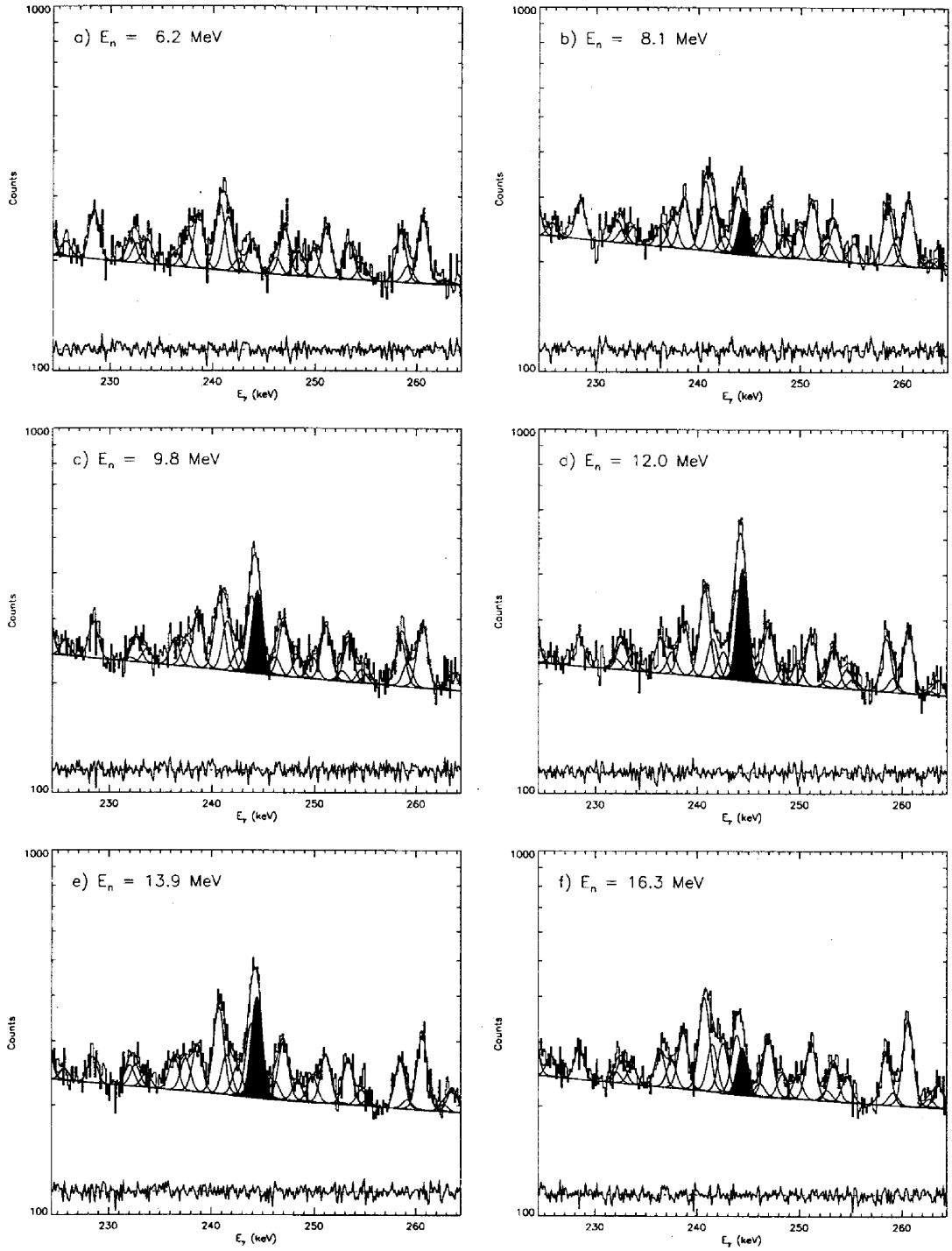

FIG. 9: Fits for the ^{234}U $10_1^+ \rightarrow 8_1^+$ transition in selected neutron-energy cuts of the GEANIE 1998 thin-target data. The $10_1^+ \rightarrow 8_1^+$ peak is shaded in red. The relative fit residual is plotted on an arbitrary scale.

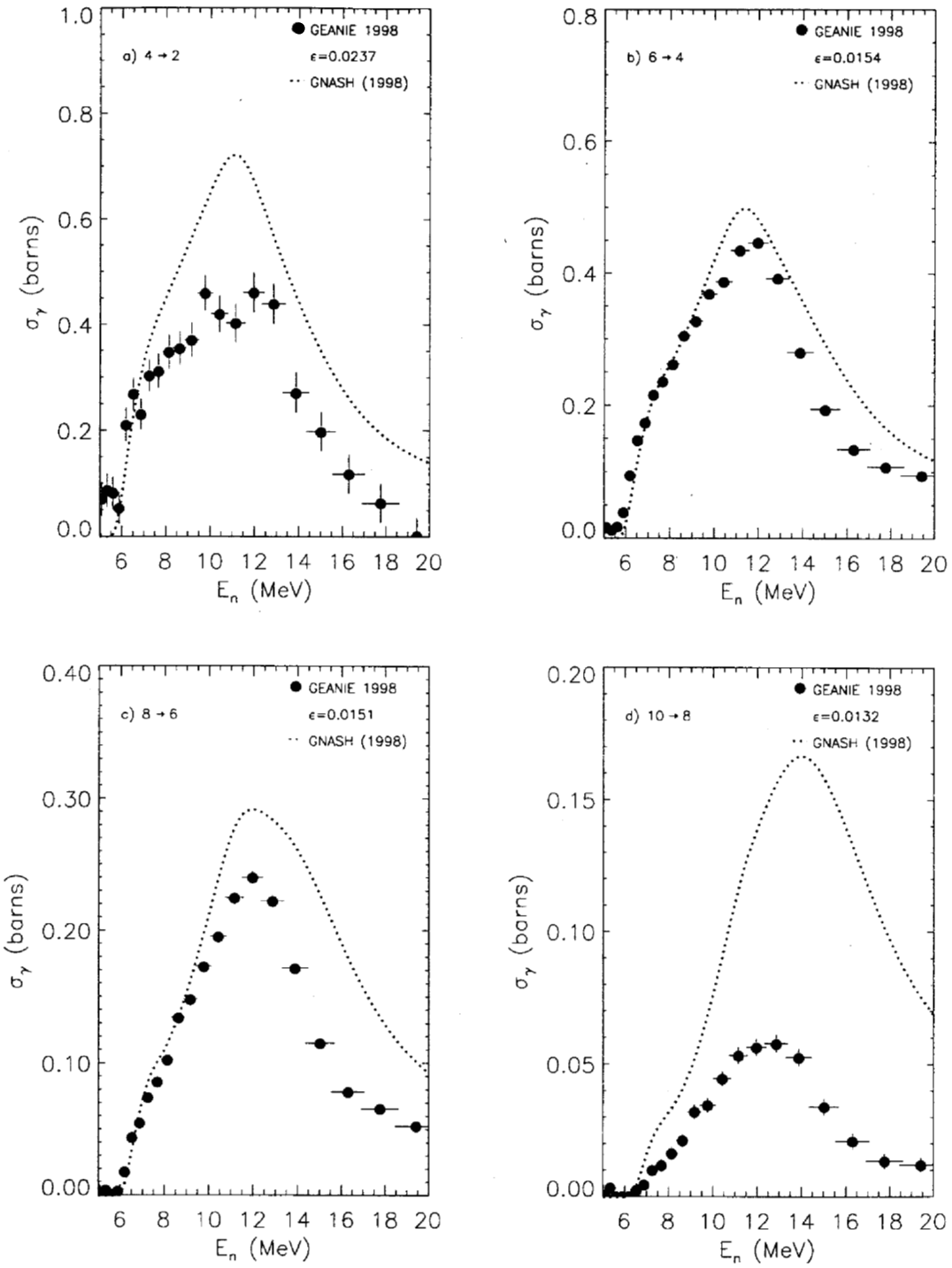

FIG. 10: Excitation functions for the ^{234}U a) $4_1^+ \rightarrow 2_1^+$, b) $6_1^+ \rightarrow 4_1^+$, c) $8_1^+ \rightarrow 6_1^+$ and d) $10_1^+ \rightarrow 8_1^+$ transitions, constructed from the GEANIE 1998 thin-target data. Only statistical errors are included. Fission-chamber data from the ^{235}U foil with a flat baseline subtraction were used to generate these yields. The detector efficiency used is quoted in each case.

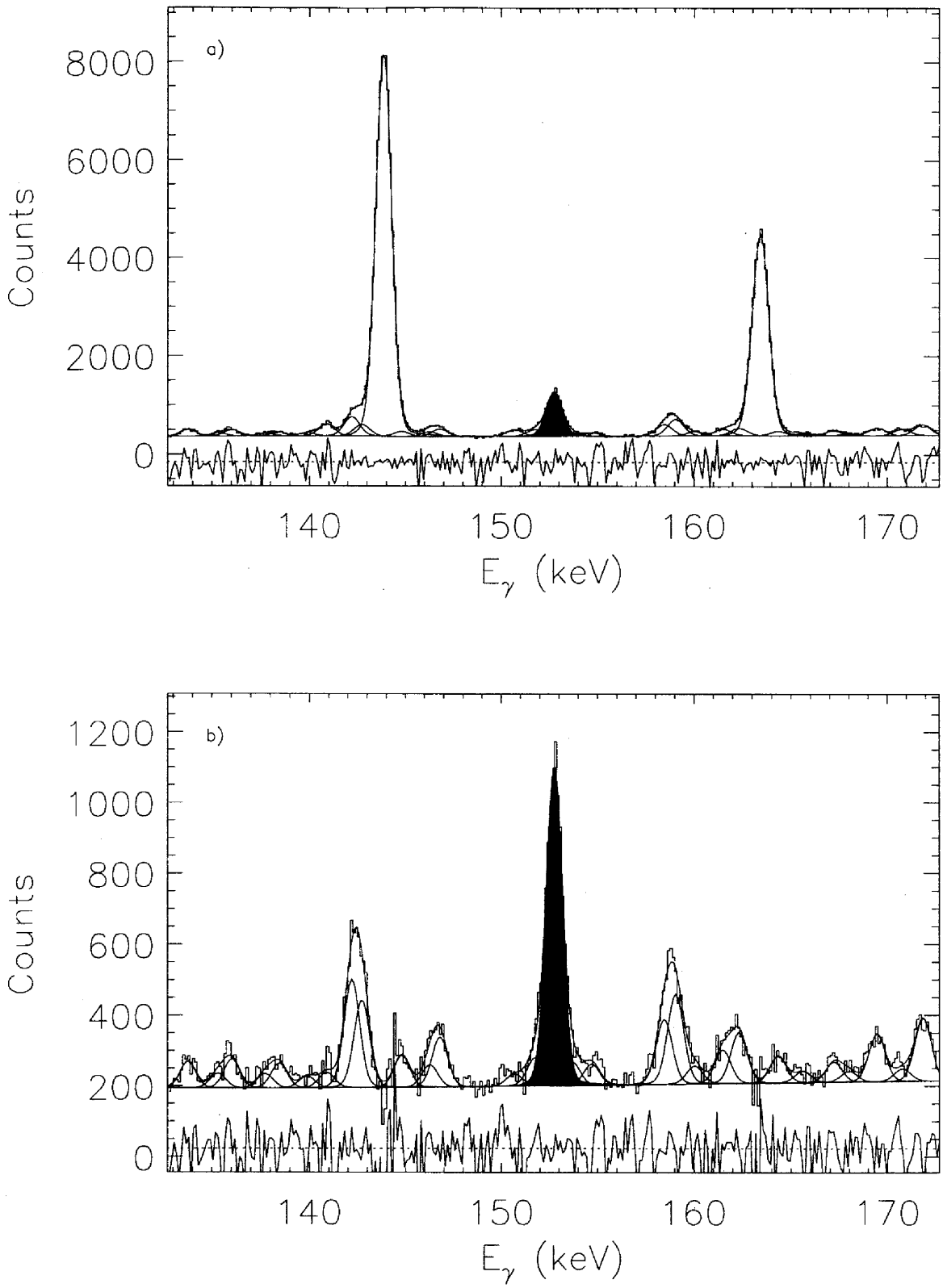

FIG. 11: Comparison of fits to a) the raw (unsubtracted) spectrum and b) the random-TOF-subtracted spectrum corresponding to $E_n = 12.0$ MeV in the region of the $6 \rightarrow 4$ peak (shaded in red).

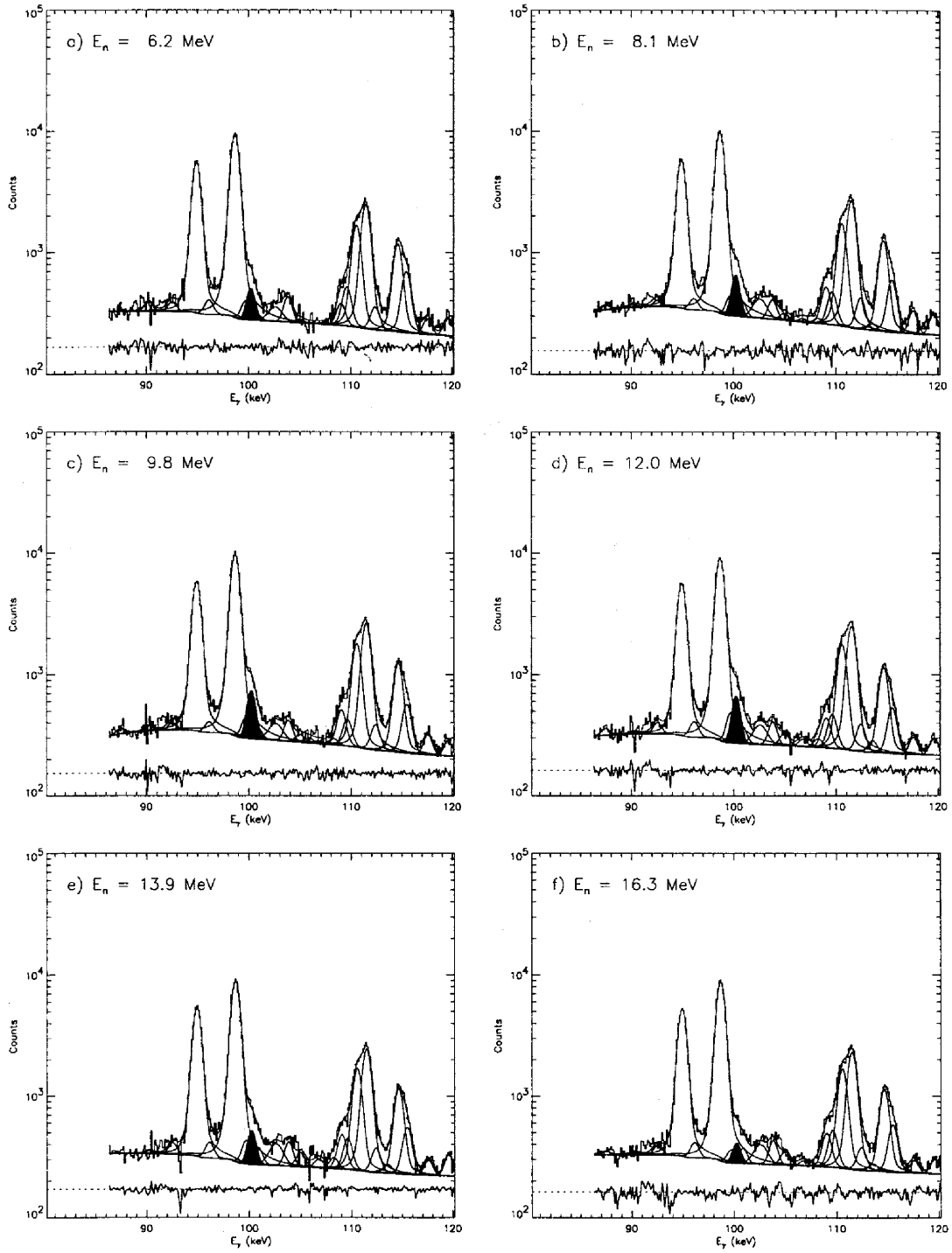

FIG. 12: Fits for the ^{234}U $4_1^+ \rightarrow 2_1^+$ transition in selected neutron-energy cuts of the GEANIE 1998 background-subtracted thin-target data. The $4_1^+ \rightarrow 2_1^+$ peak is shaded in red. The relative fit residual is plotted on an arbitrary scale.

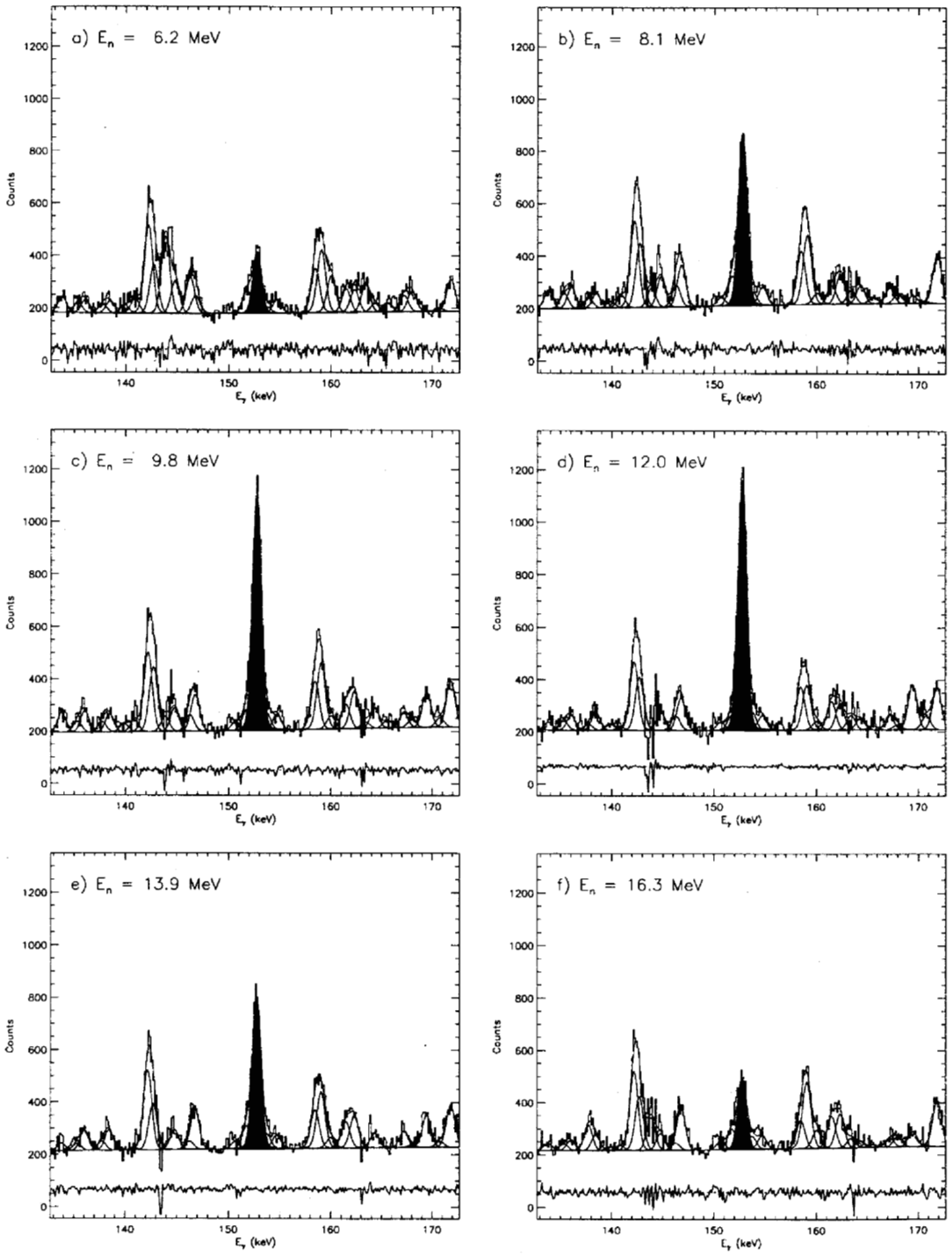

FIG. 13: Fits for the ^{234}U $6_1^+ \rightarrow 4_1^+$ transition in selected neutron-energy cuts of the GEANIE 1998 background-subtracted thin-target data. The $6_1^+ \rightarrow 4_1^+$ peak is shaded in red. The relative fit residual is plotted on an arbitrary scale.

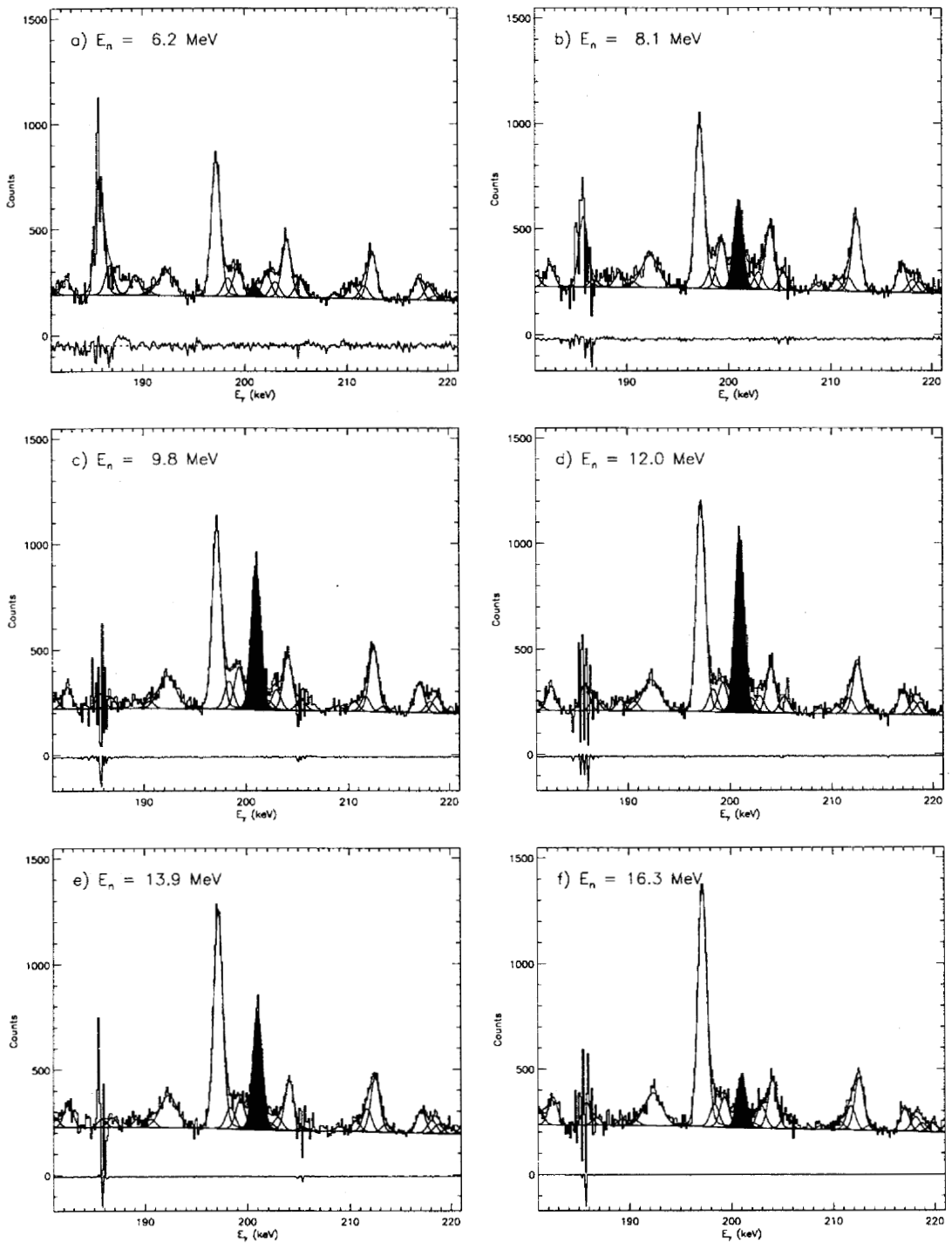

FIG. 14: Fits for the ^{234}U $8_1^+ \rightarrow 6_1^+$ transition in selected neutron-energy cuts of the GEANIE 1998 background-subtracted thin-target data. The $8_1^+ \rightarrow 6_1^+$ peak is shaded in red. The relative fit residual is plotted on an arbitrary scale.

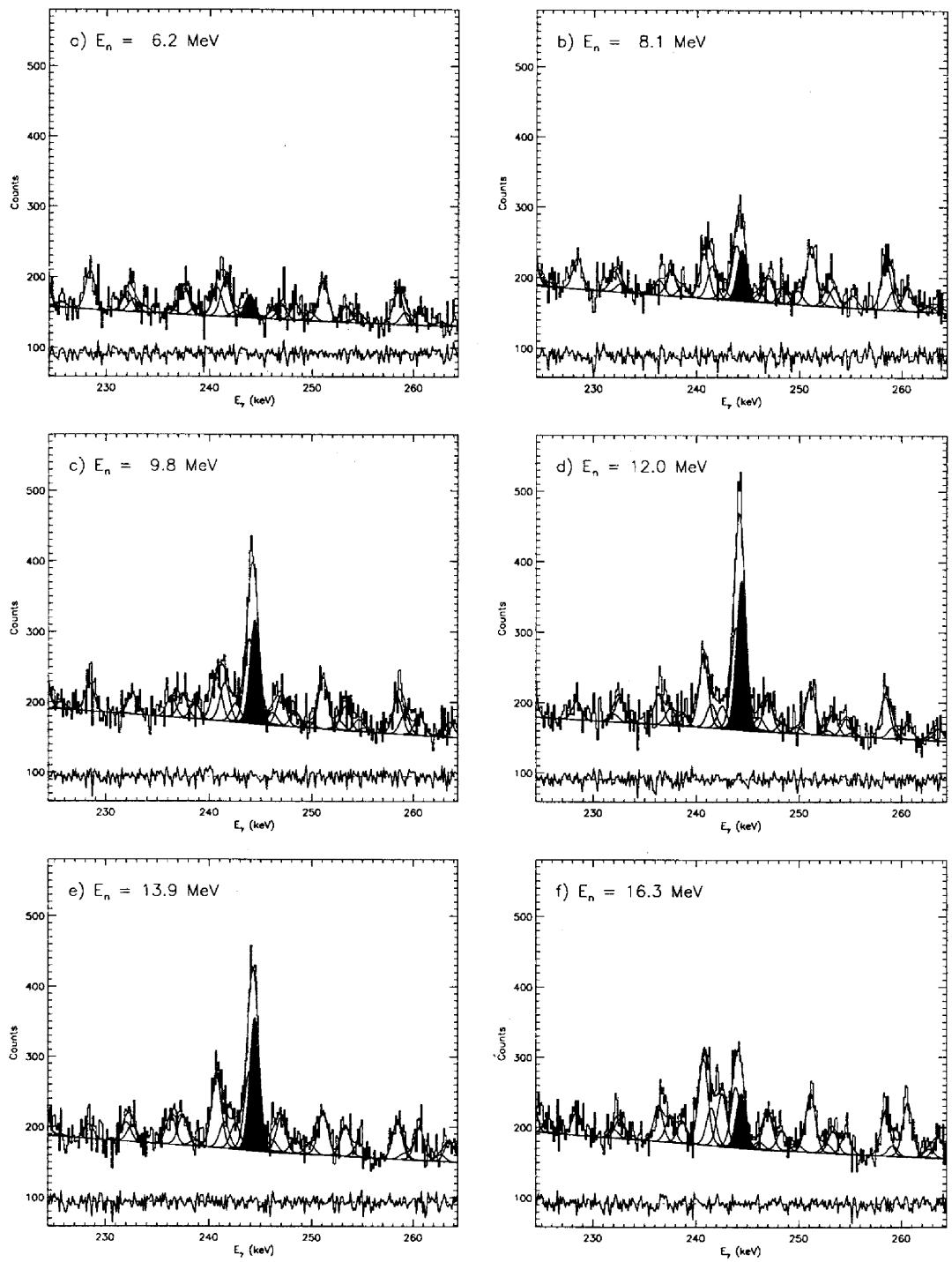

FIG. 15: Fits for the ^{234}U $10_1^+ \rightarrow 8_1^+$ transition in selected neutron-energy cuts of the GEANIE 1998 background-subtracted thin-target data. The $10_1^+ \rightarrow 8_1^+$ peak is shaded in red. The relative fit residual is plotted on an arbitrary scale.

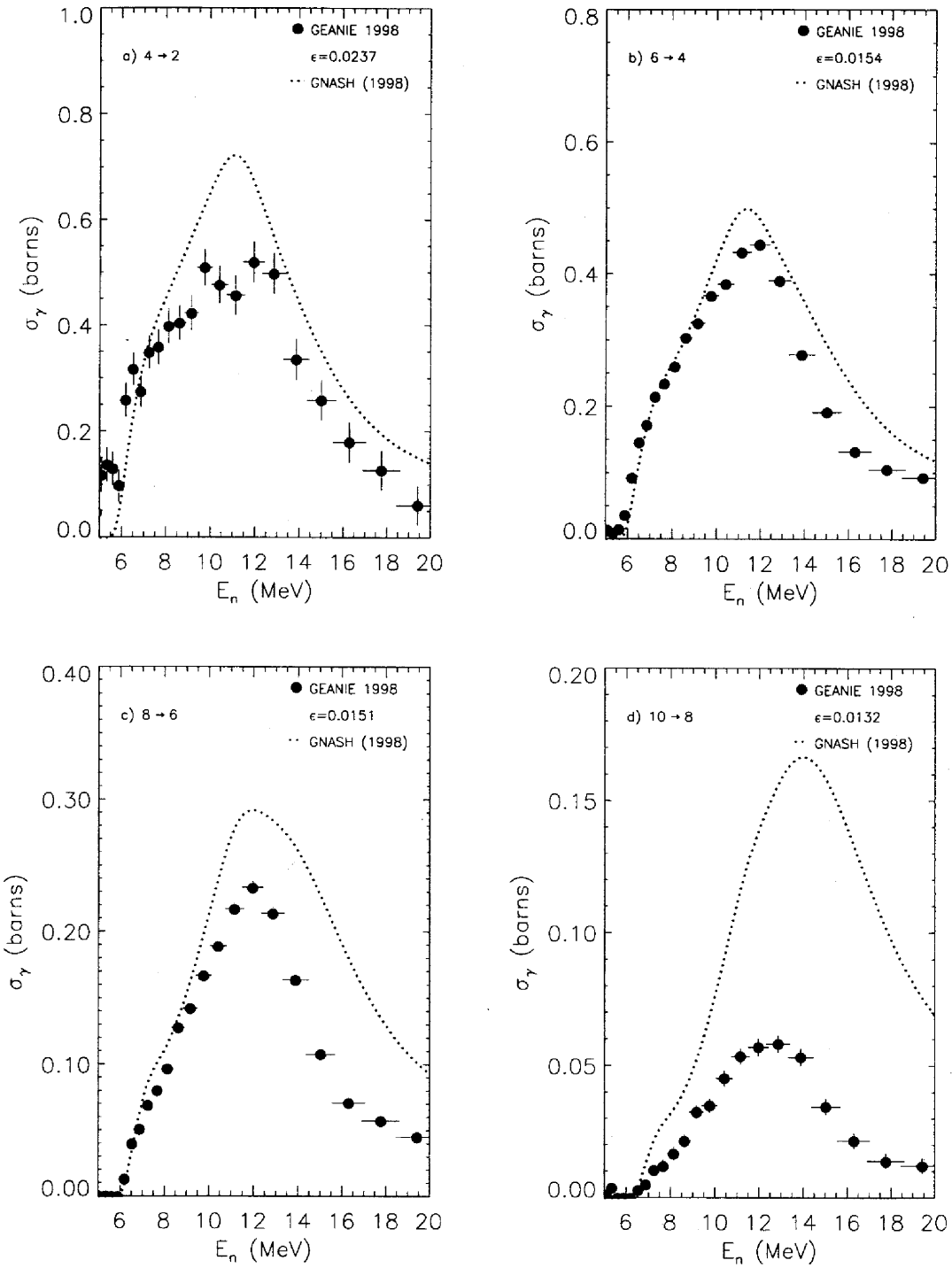

FIG. 16: Excitation functions for the ^{234}U a) $4_1^+ \rightarrow 2_1^+$, b) $6_1^+ \rightarrow 4_1^+$, c) $8_1^+ \rightarrow 6_1^+$ and d) $10_1^+ \rightarrow 8_1^+$ transitions, constructed from the GEANIE 1998 background-subtracted thin-target data. Only statistical errors are included. Fission-chamber data from the ^{235}U foil with a flat baseline subtraction were used to generate these yields. The detector efficiency used is quoted in each case.

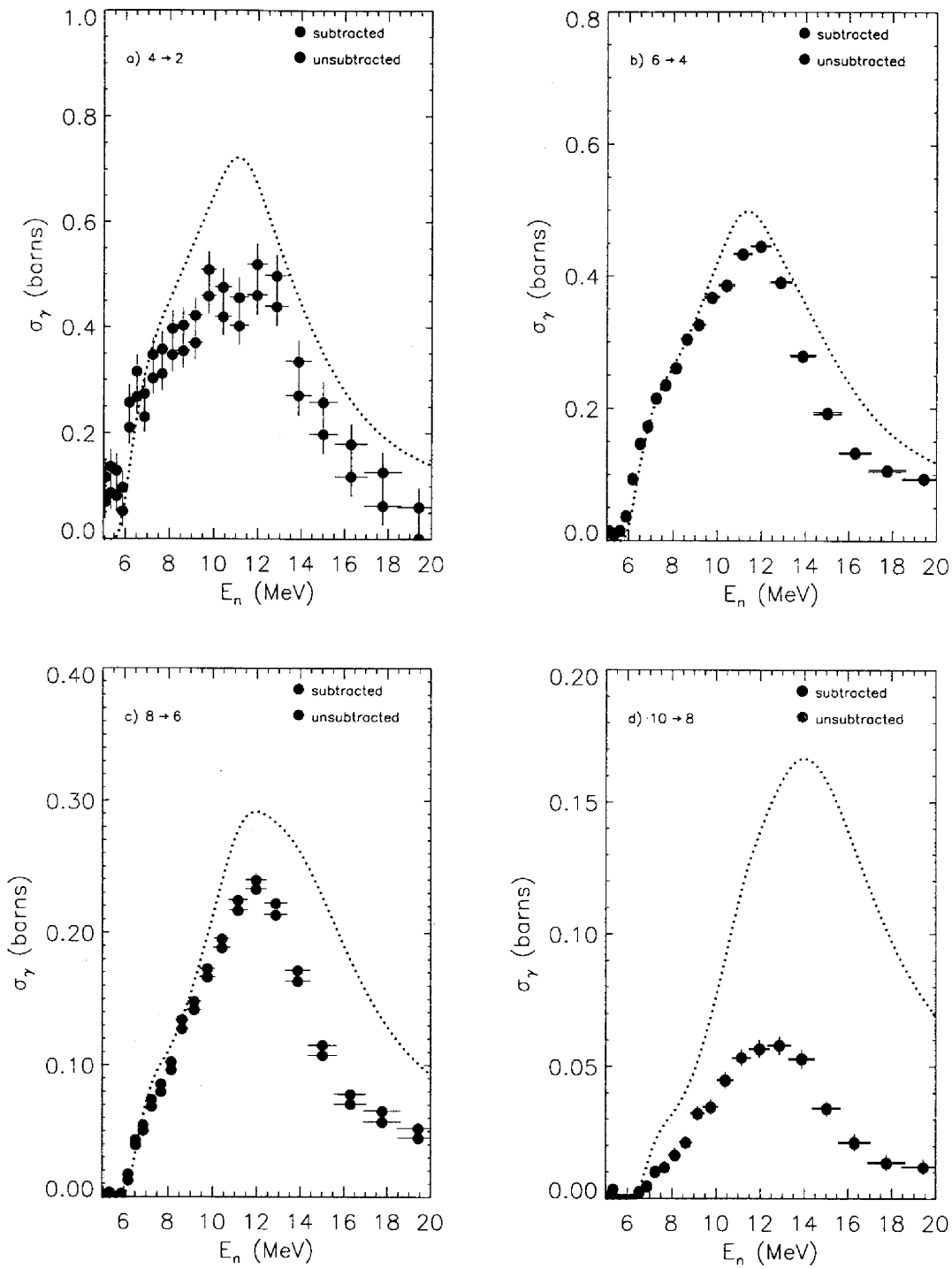

FIG. 17: Comparison of excitation functions for the ^{234}U a) $4_1^+ \rightarrow 2_1^+$, b) $6_1^+ \rightarrow 4_1^+$, c) $8_1^+ \rightarrow 6_1^+$ and d) $10_1^+ \rightarrow 8_1^+$ transitions, with and without random-TOF background subtraction for the GEANIE 1998 thin-target data. The GNASH prediction is shown as a dotted green curve. Only statistical errors are included. Fission-chamber data from the ^{235}U foil with a flat baseline subtraction were used to generate these yields.

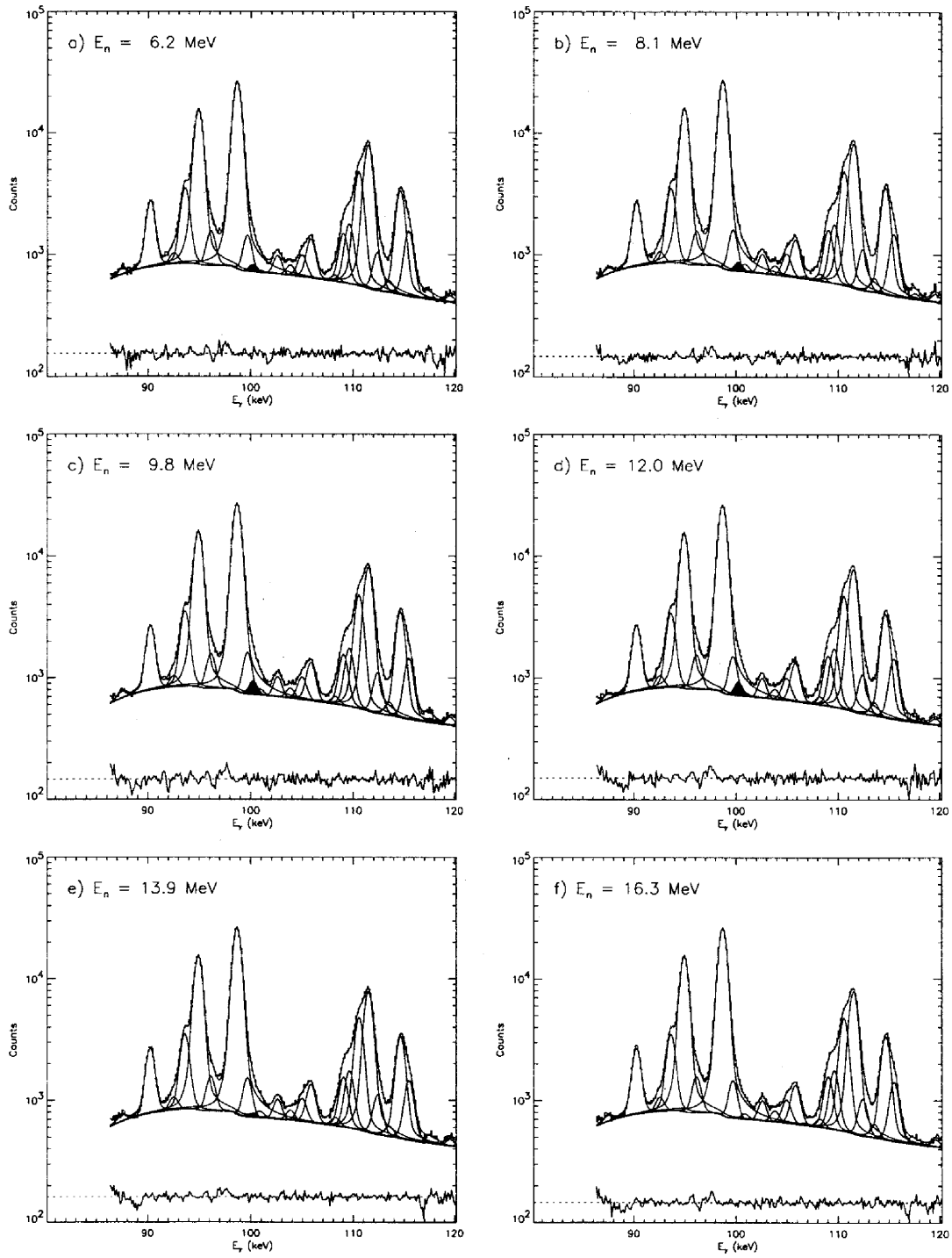

FIG. 19: Fits for the ^{234}U $4_1^+ \rightarrow 2_1^+$ transition in selected neutron-energy cuts of the GEANIE 1998 thick-target data. The $4_1^+ \rightarrow 2_1^+$ peak is shaded in red. The relative fit residual is plotted on an arbitrary scale.

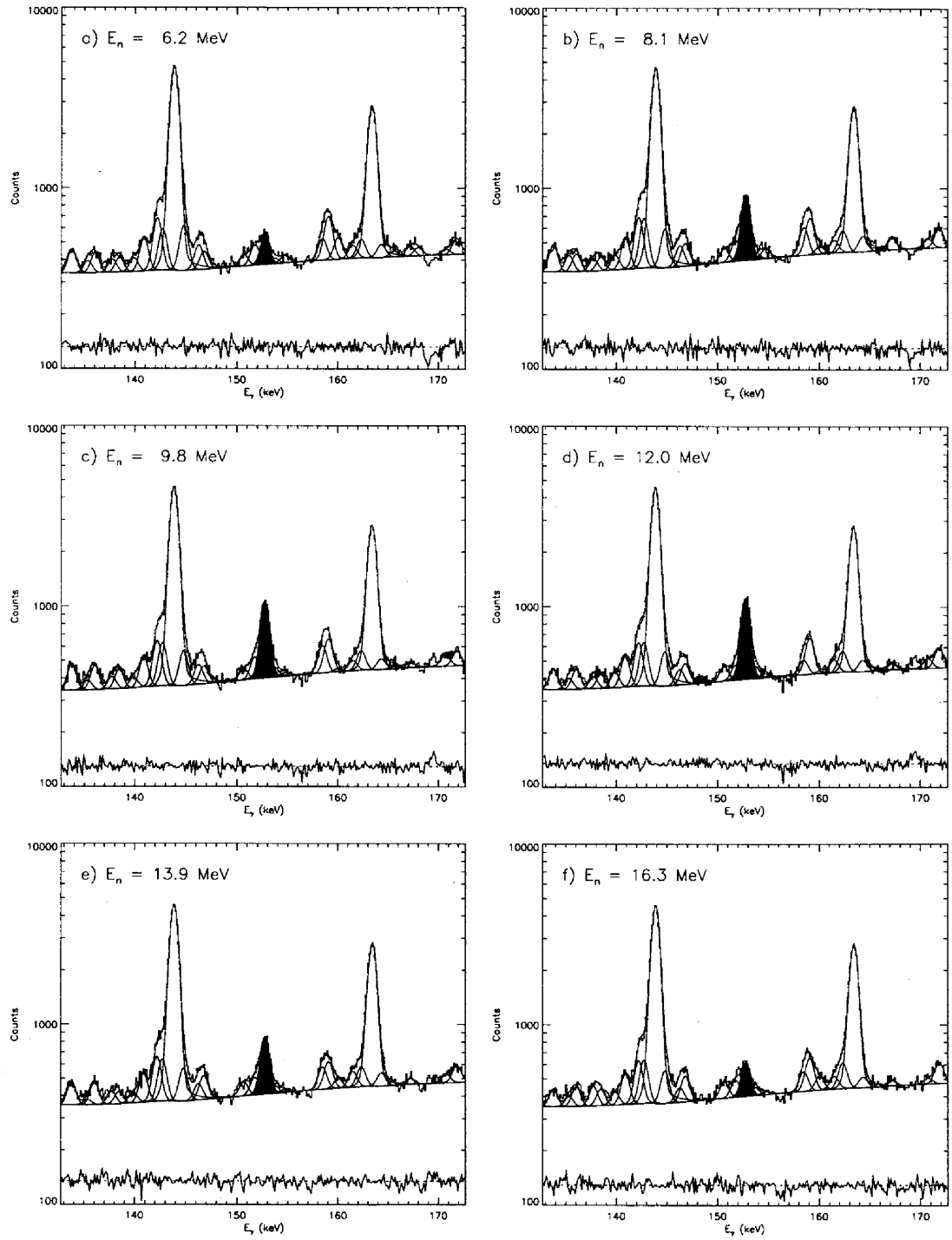

FIG. 20: Fits for the ^{234}U $6_1^+ \rightarrow 4_1^+$ transition in selected neutron-energy cuts of the GEANIE 1998 thick-target data. The $6_1^+ \rightarrow 4_1^+$ peak is shaded in red. The relative fit residual is plotted on an arbitrary scale.

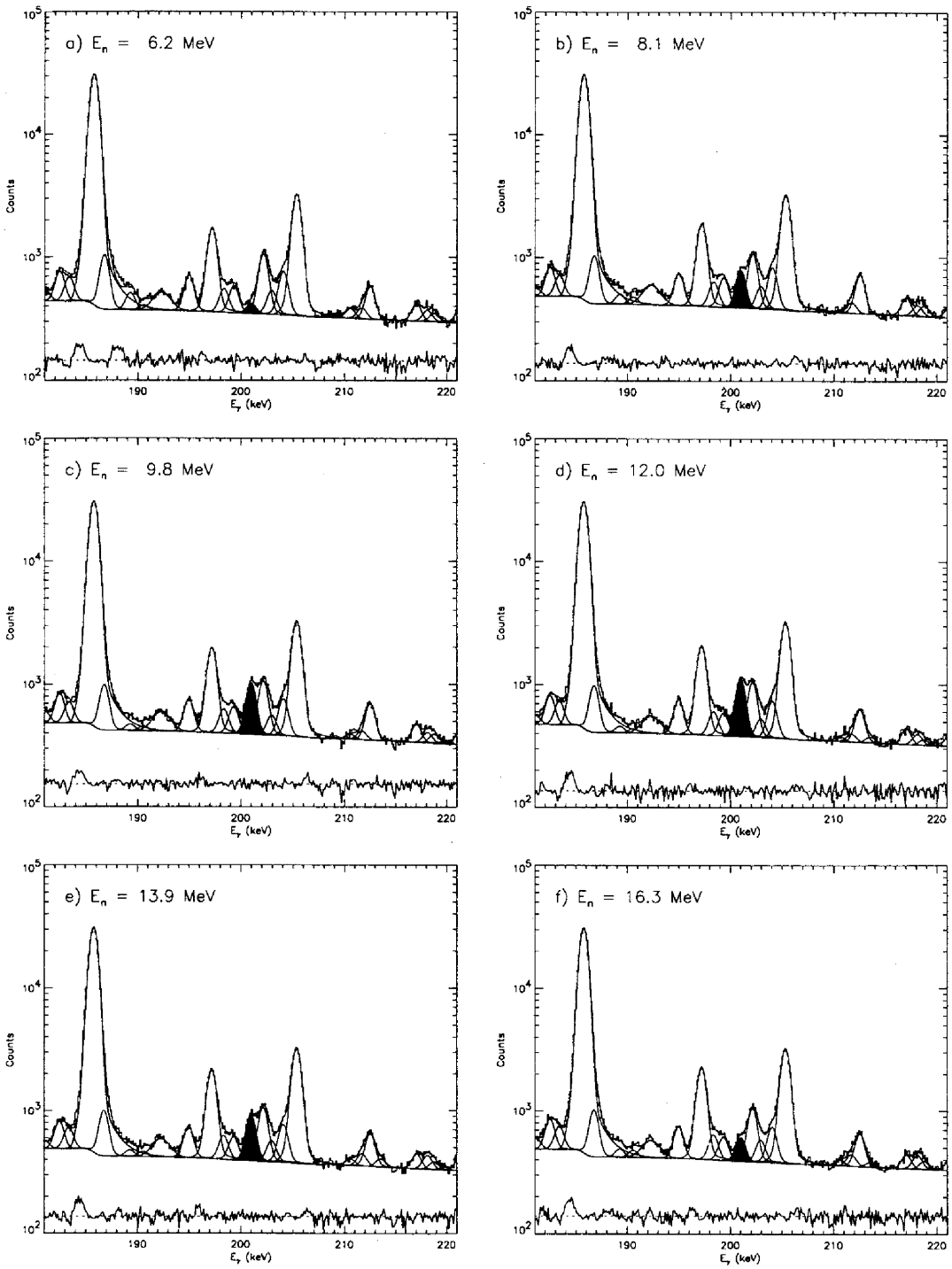

FIG. 21: Fits for the ^{234}U $8_1^+ \rightarrow 6_1^+$ transition in selected neutron-energy cuts of the GEANIE 1998 thick-target data. The $8_1^+ \rightarrow 6_1^+$ peak is shaded in red. The relative fit residual is plotted on an arbitrary scale.

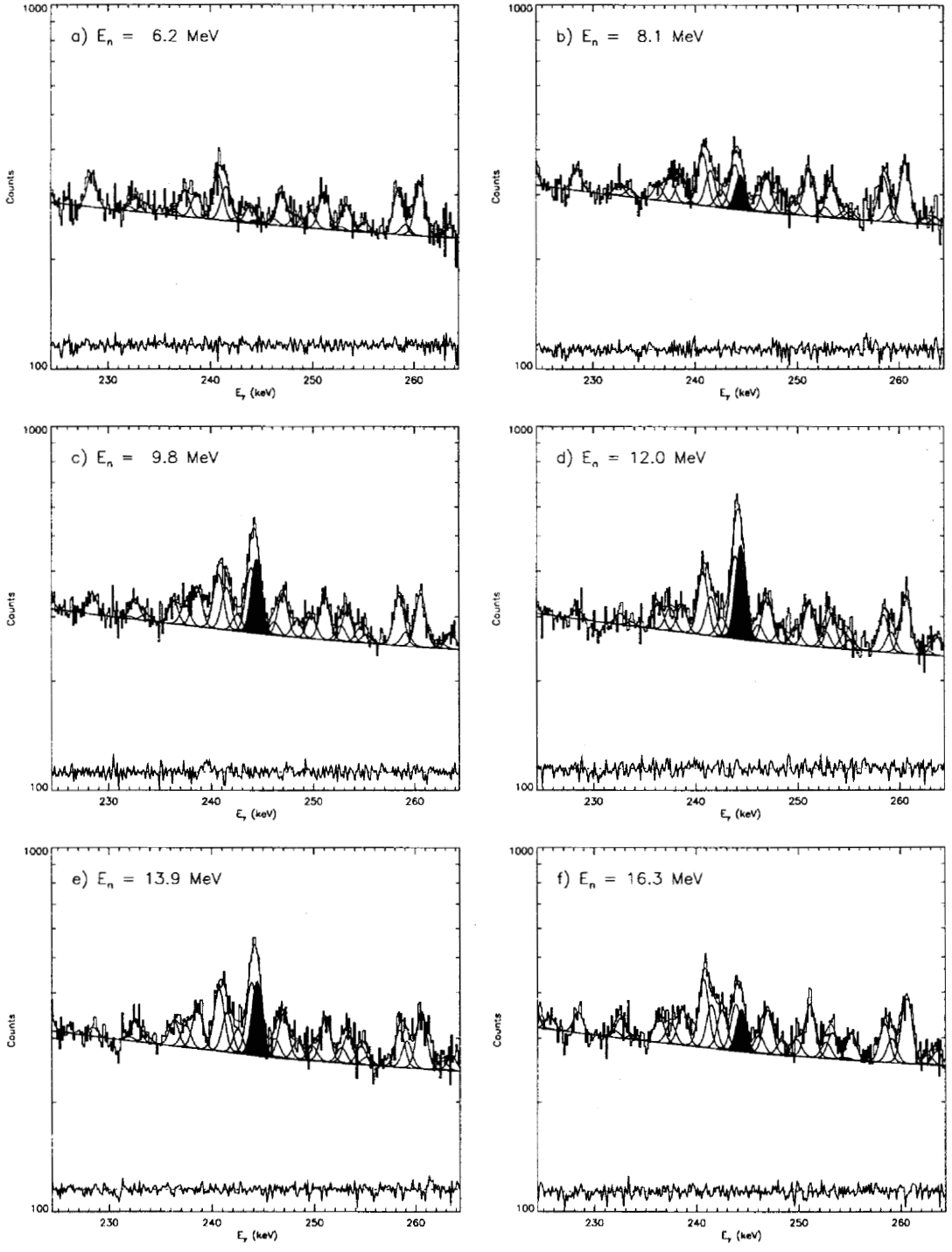

FIG. 22: Fits for the ^{234}U $10_1^+ \rightarrow 8_1^+$ transition in selected neutron-energy cuts of the GEANIE 1998 thick-target data. The $10_1^+ \rightarrow 8_1^+$ peak is shaded in red. The relative fit residual is plotted on an arbitrary scale.

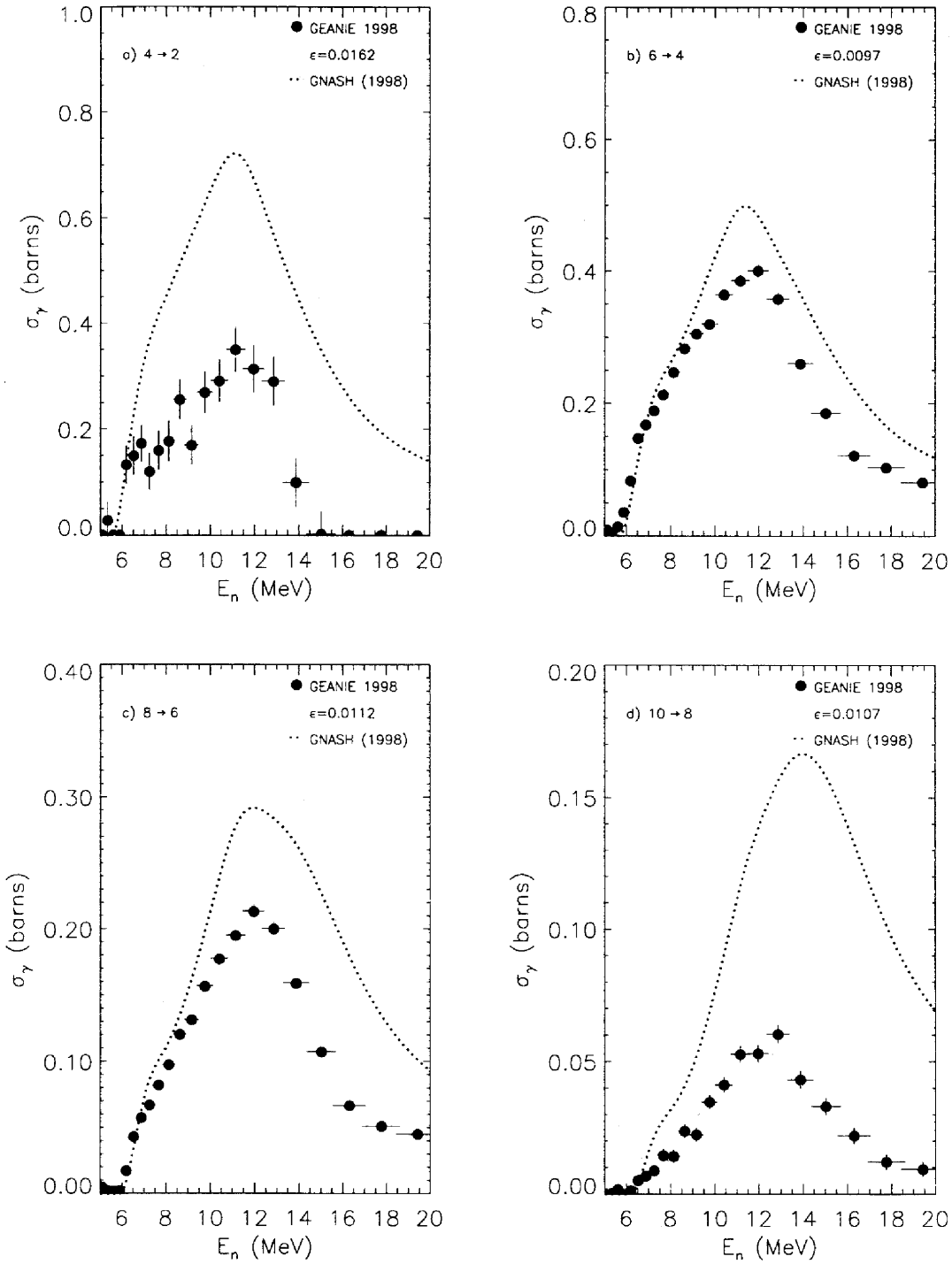

FIG. 23: Excitation functions for the ^{234}U a) $4_1^+ \rightarrow 2_1^+$, b) $6_1^+ \rightarrow 4_1^+$, c) $8_1^+ \rightarrow 6_1^+$ and d) $10_1^+ \rightarrow 8_1^+$ transitions, constructed from the GEANIE 1998 thick-target data. Only statistical errors are included. Fission-chamber data from the ^{235}U foil with a flat baseline subtraction were used to generate these yields. The detector efficiency used is quoted in each case.

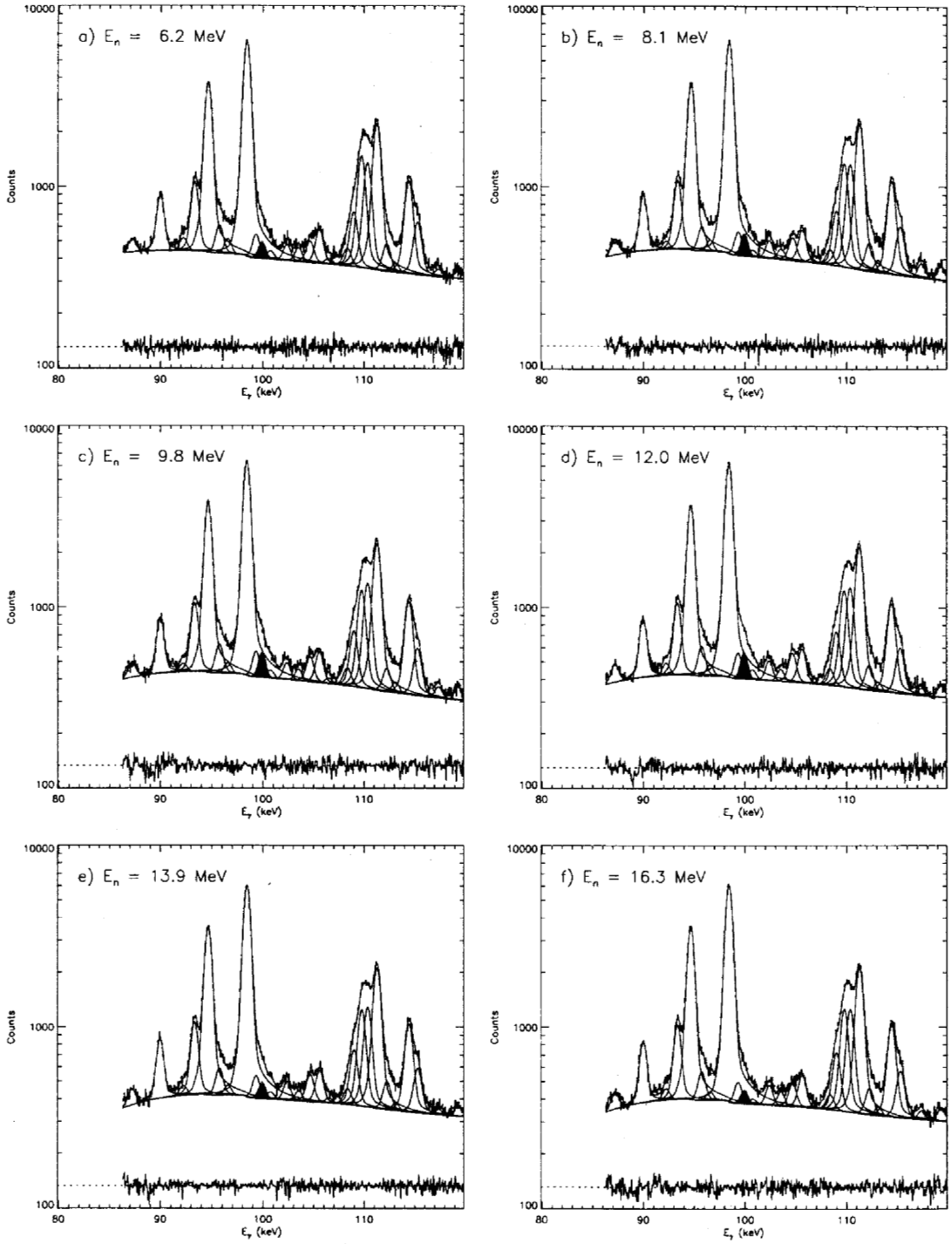

FIG. 25: Fits for the ^{234}U $4_1^+ \rightarrow 2_1^+$ transition in selected neutron-energy cuts of the GEANIE 1999 data. The $4_1^+ \rightarrow 2_1^+$ peak is shaded in red. The relative residual is plotted on an arbitrary scale.

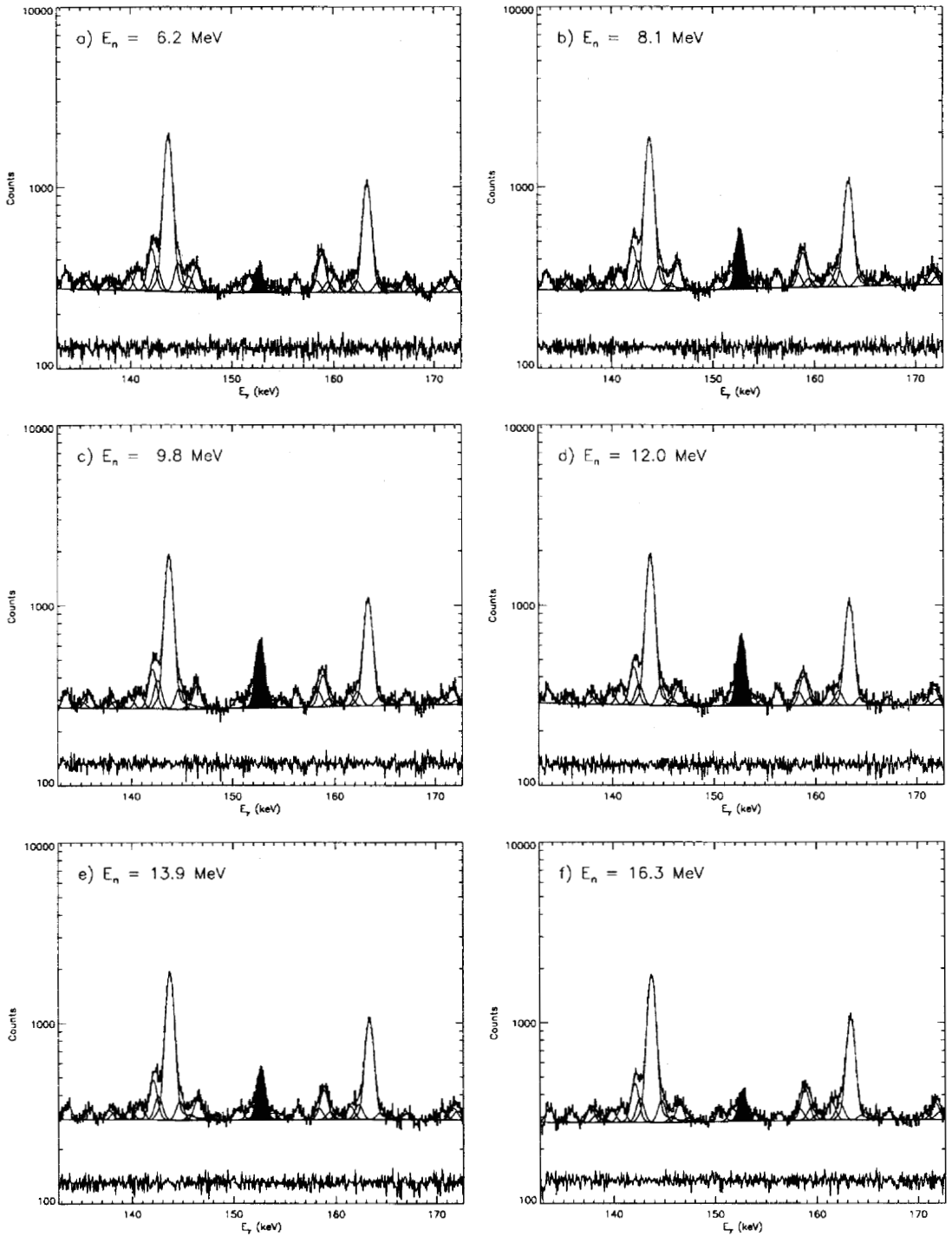

FIG. 26: Fits for the ^{234}U $6_1^+ \rightarrow 4_1^+$ transition in selected neutron-energy cuts of the GEANIE 1999 data. The $6_1^+ \rightarrow 4_1^+$ peak is shaded in red. The relative residual is plotted on an arbitrary scale.

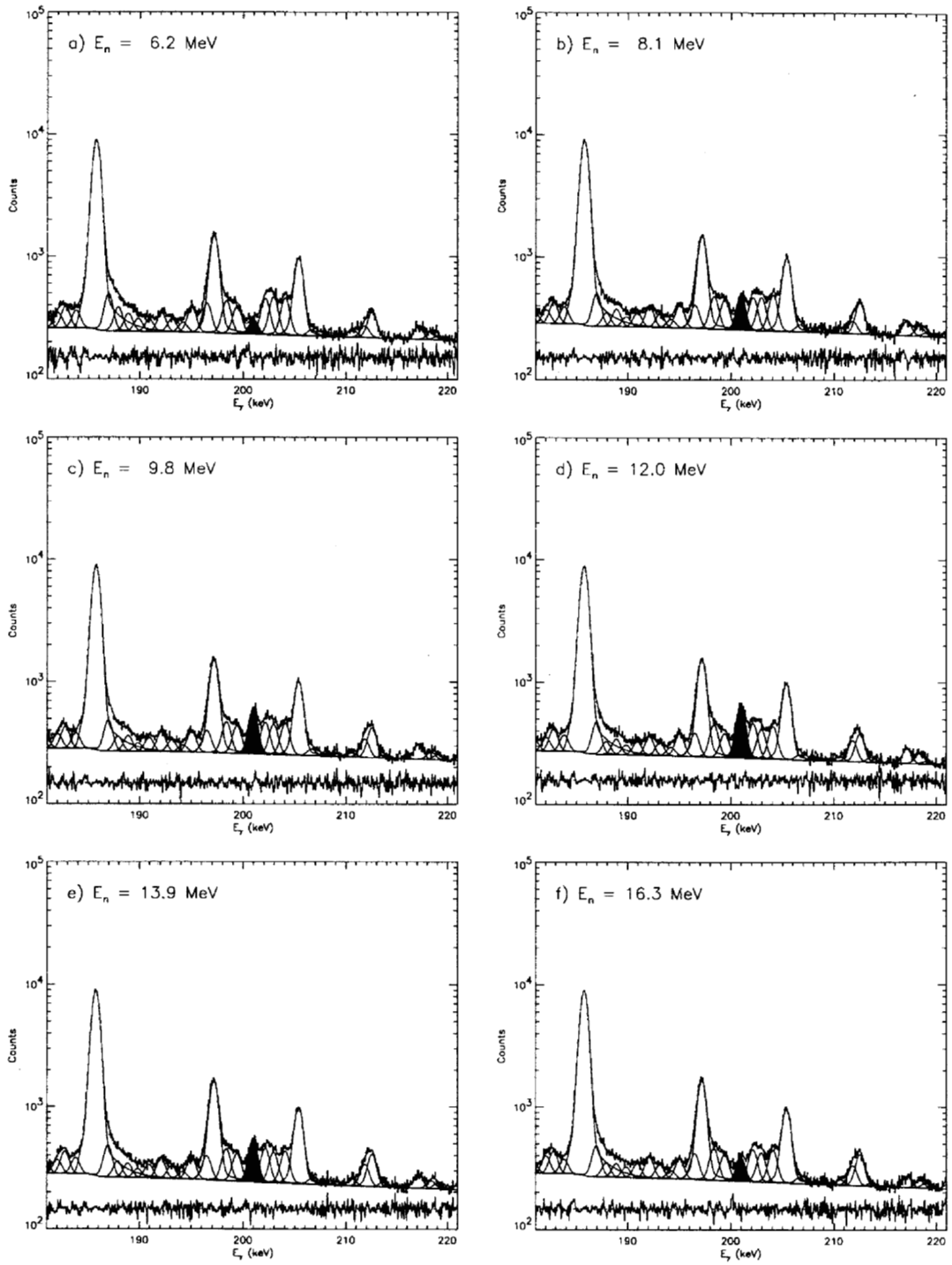

FIG. 27: Fits for the ^{234}U $8_1^+ \rightarrow 6_1^+$ transition in selected neutron-energy cuts of the GEANIE 1999 data. The $8_1^+ \rightarrow 6_1^+$ peak is shaded in red. The relative residual is plotted on an arbitrary scale.

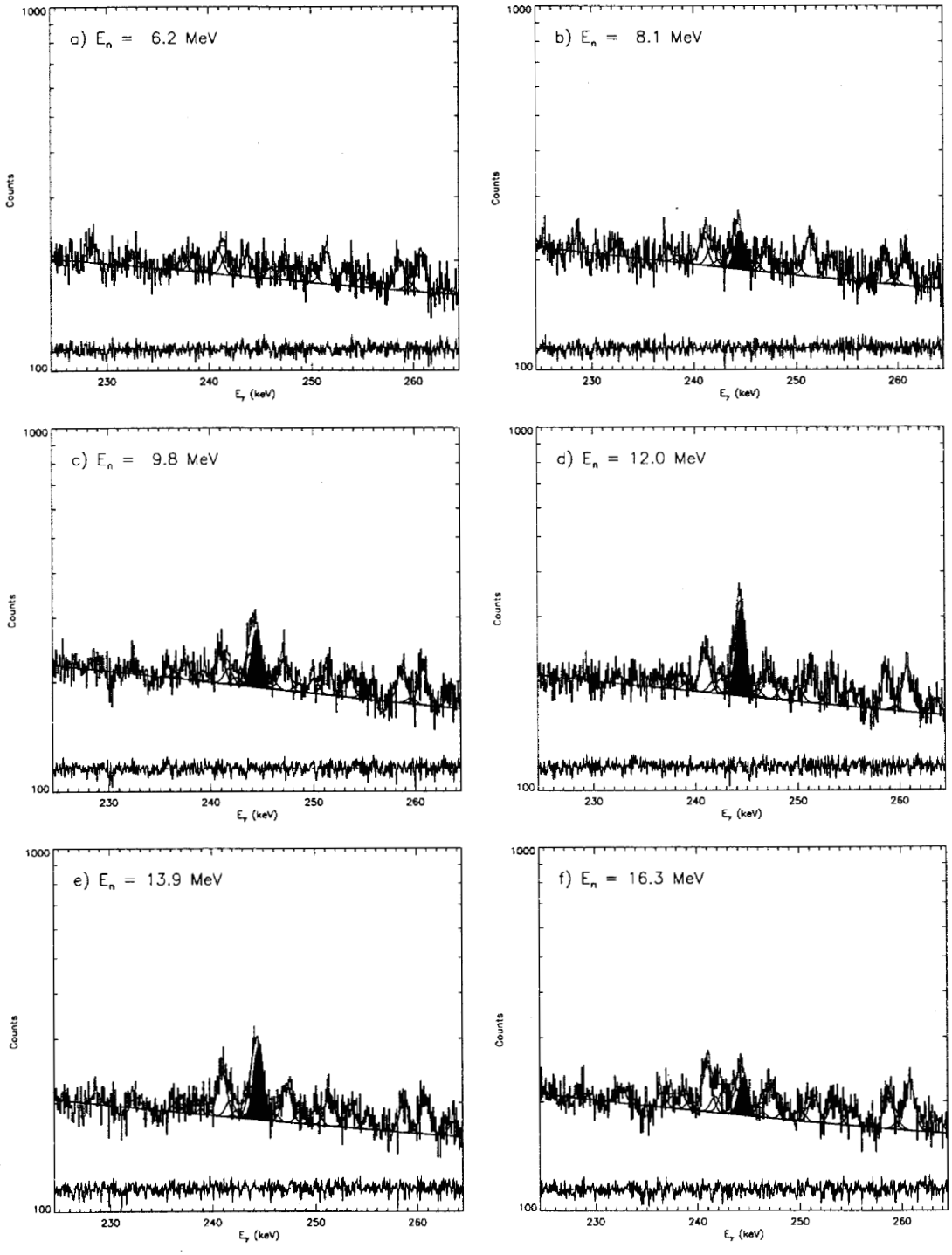

FIG. 28: Fits for the ^{234}U $10_1^+ \rightarrow 8_1^+$ transition in selected neutron-energy cuts of the GEANIE 1999 data. The $10_1^+ \rightarrow 8_1^+$ peak is shaded in red. The relative residual is plotted on an arbitrary scale.

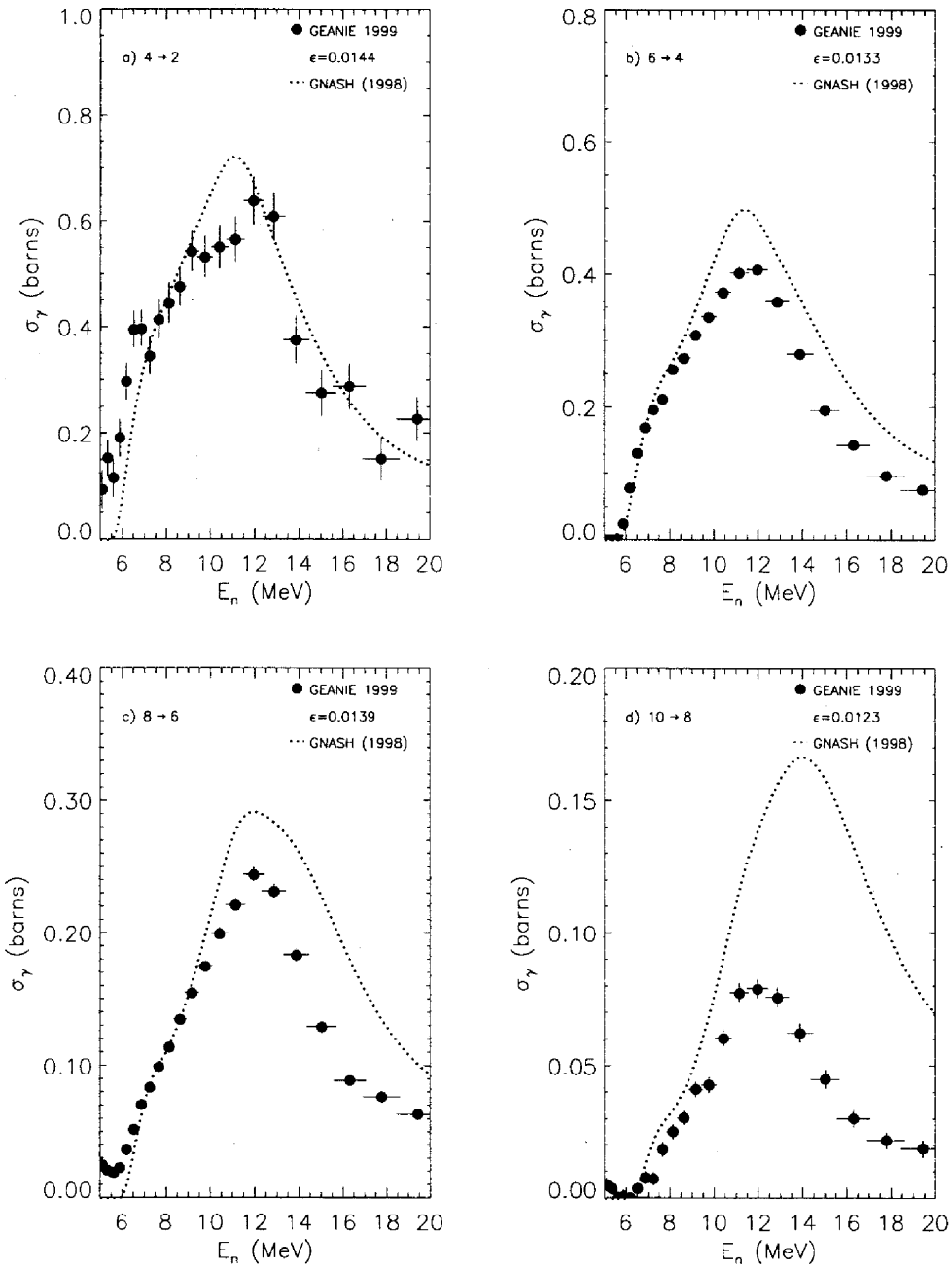

FIG. 29: a)-d): Excitation functions for the ^{234}U $4_1^+ \rightarrow 2_1^+$, $6_1^+ \rightarrow 4_1^+$, $8_1^+ \rightarrow 6_1^+$ and $10_1^+ \rightarrow 8_1^+$ transitions, constructed from the GEANIE 1999 data. Only statistical errors are included. Fission-chamber data from the ^{235}U foil with a flat baseline subtraction was used to generate these yields. The detector efficiency used is quoted in each case.

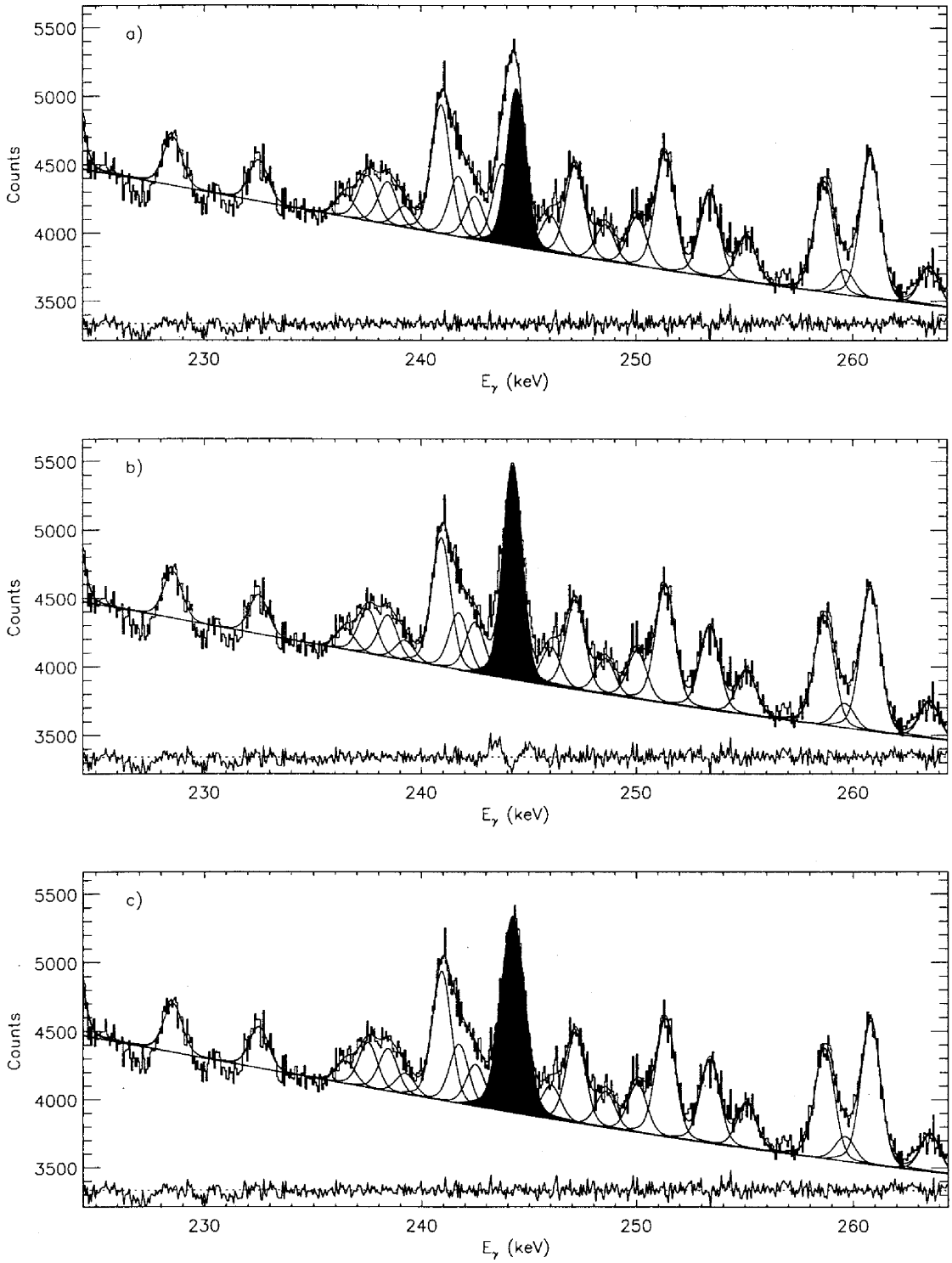

FIG. 30: Fits of the 244-keV peak assuming: a) a pair of lines, b) a single line with peak width determined from the global spectrum fit, and c) a single line with locally-fit peak width. The relative residual spectrum is plotted on an arbitrary scale.

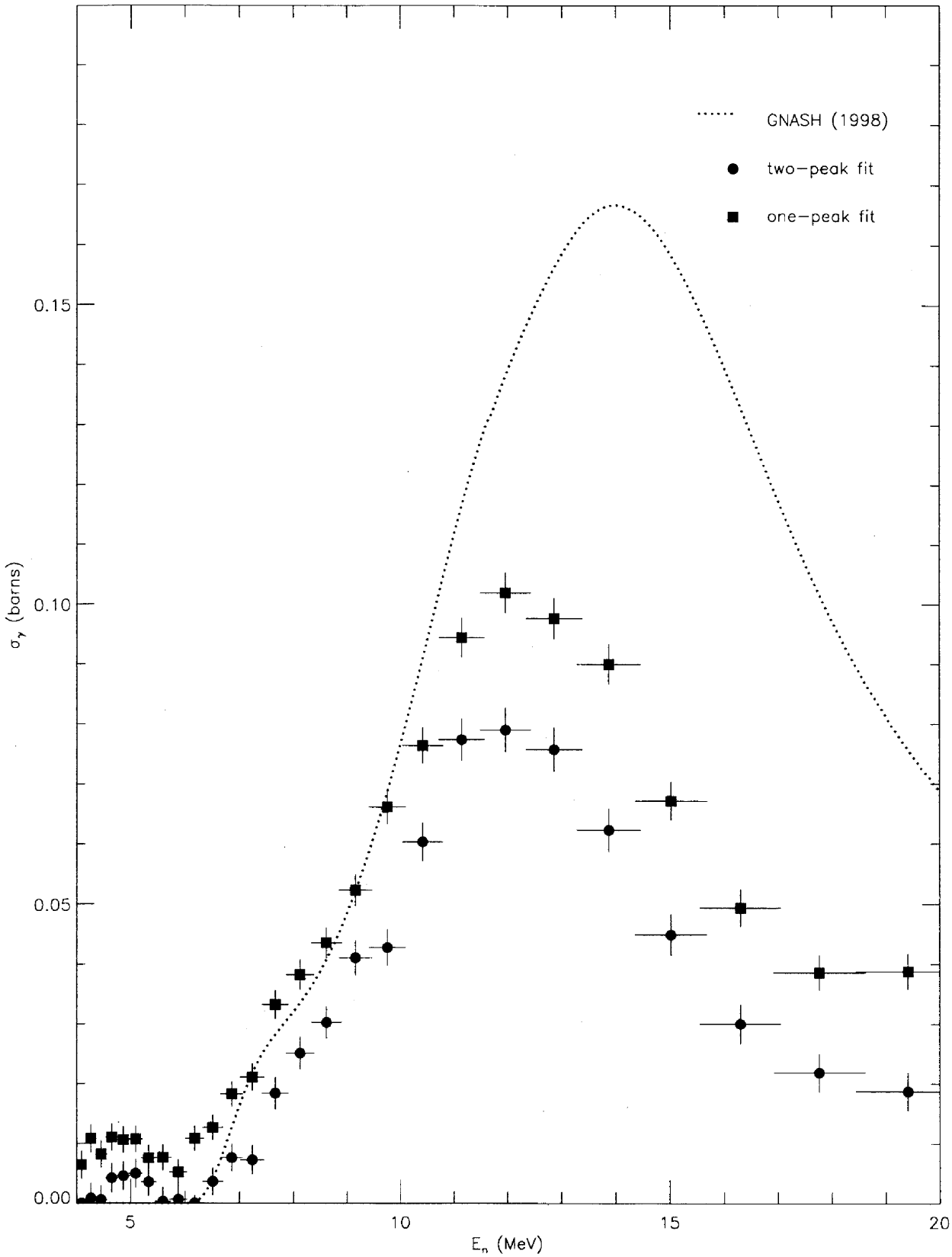

FIG. 31: Partial cross sections constructed from the one-peak and two-peak fits, compared with the GNASH prediction.

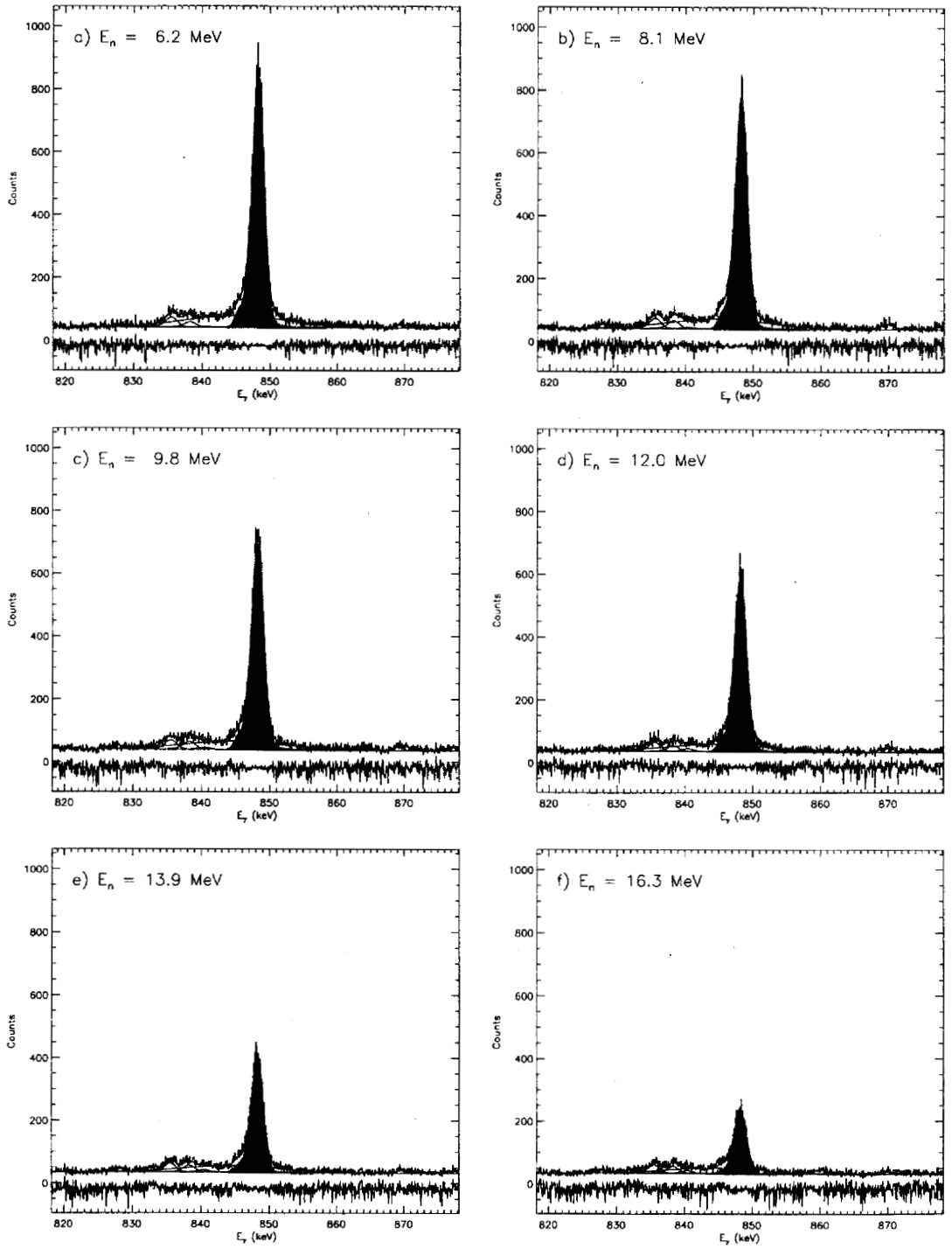

FIG. 32: Fits for the ^{56}Fe $2_1^+ \rightarrow 0_1^+$ transition in selected neutron-energy cuts of the GEANIE 1999 data. The $2_1^+ \rightarrow 0_1^+$ peak is shaded in red. The relative fit residual is plotted on an arbitrary scale.

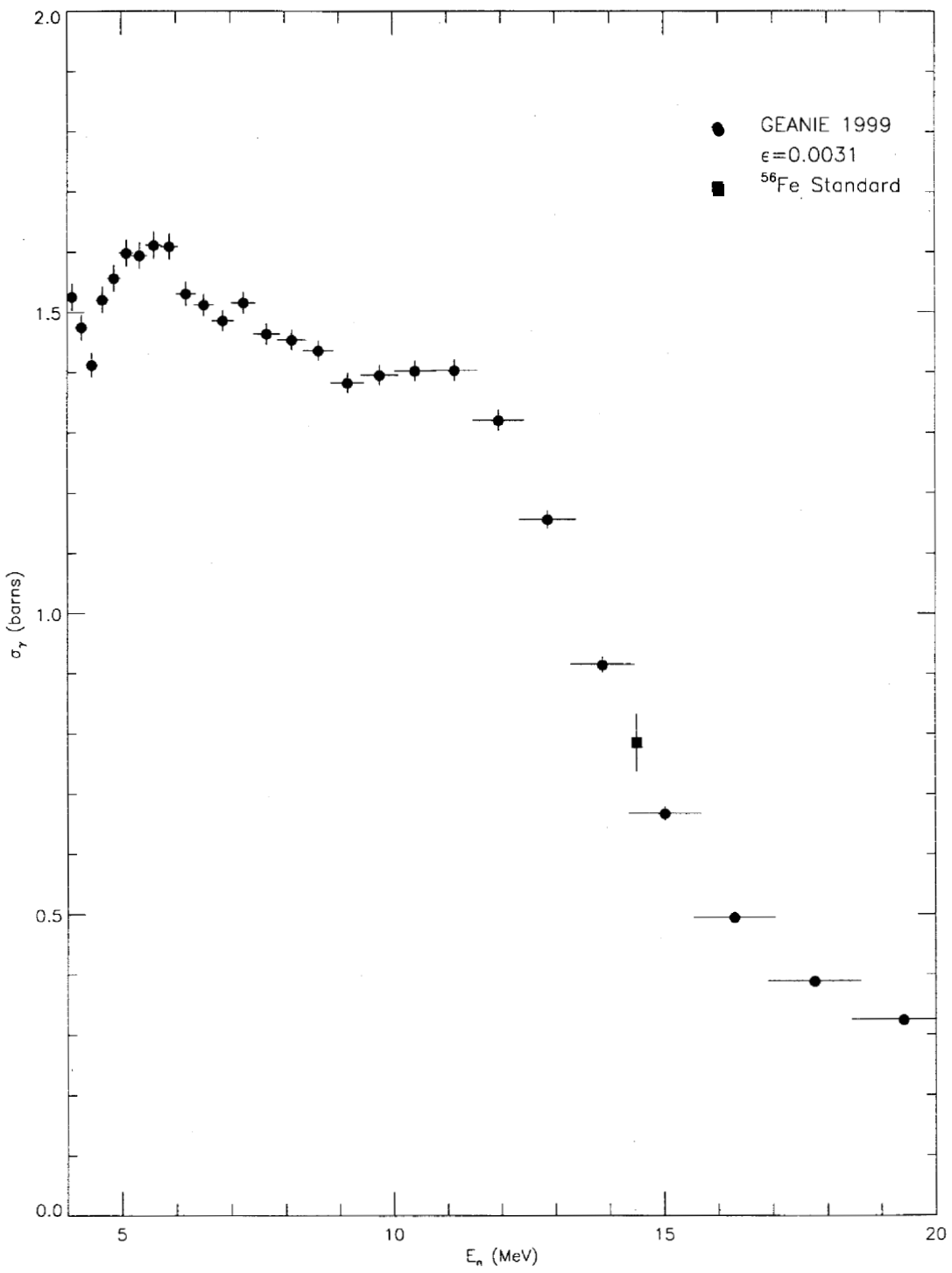

FIG. 33: Comparison of the ^{56}Fe(n,n′) $2_1^+ \rightarrow 0_1^+$ partial cross section extracted from the GEANIE 1999 data without background subtraction to the evaluated standard at $E_n = 14.5$ MeV. Data are flux-normalized using the ^{235}U fission foil with full baseline subtraction. The detector efficiency used is quoted in the legend.

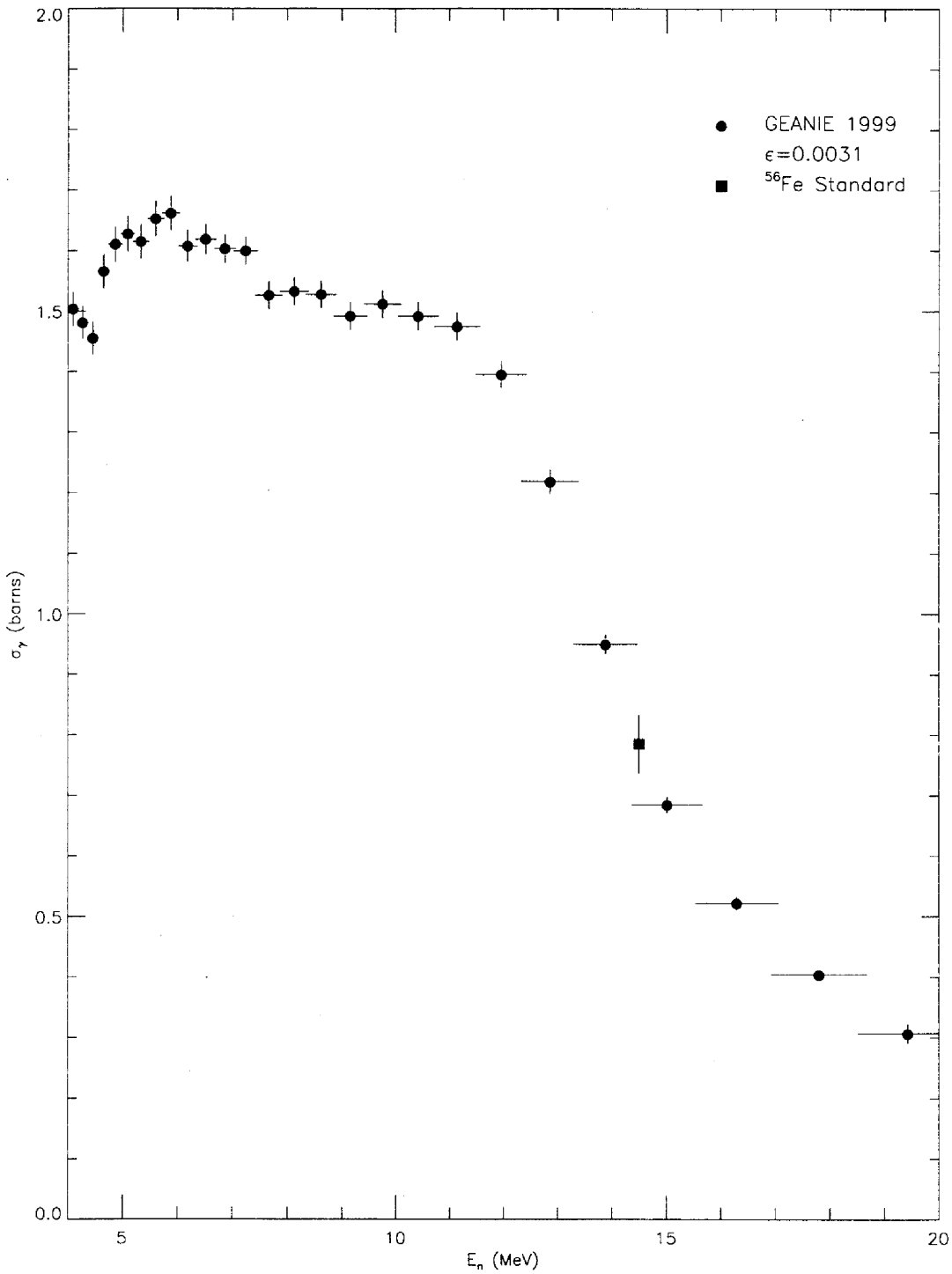

FIG. 34: Comparison of the ^{56}Fe(n,n′) $2_1^+ \rightarrow 0_1^+$ partial cross section extracted from the GEANIE 1999 data without background subtraction to the evaluated standard at $E_n = 14.5$ MeV. Data are flux-normalized using the ^{238}U fission foil without baseline subtraction. The detector efficiency used is quoted in the legend.

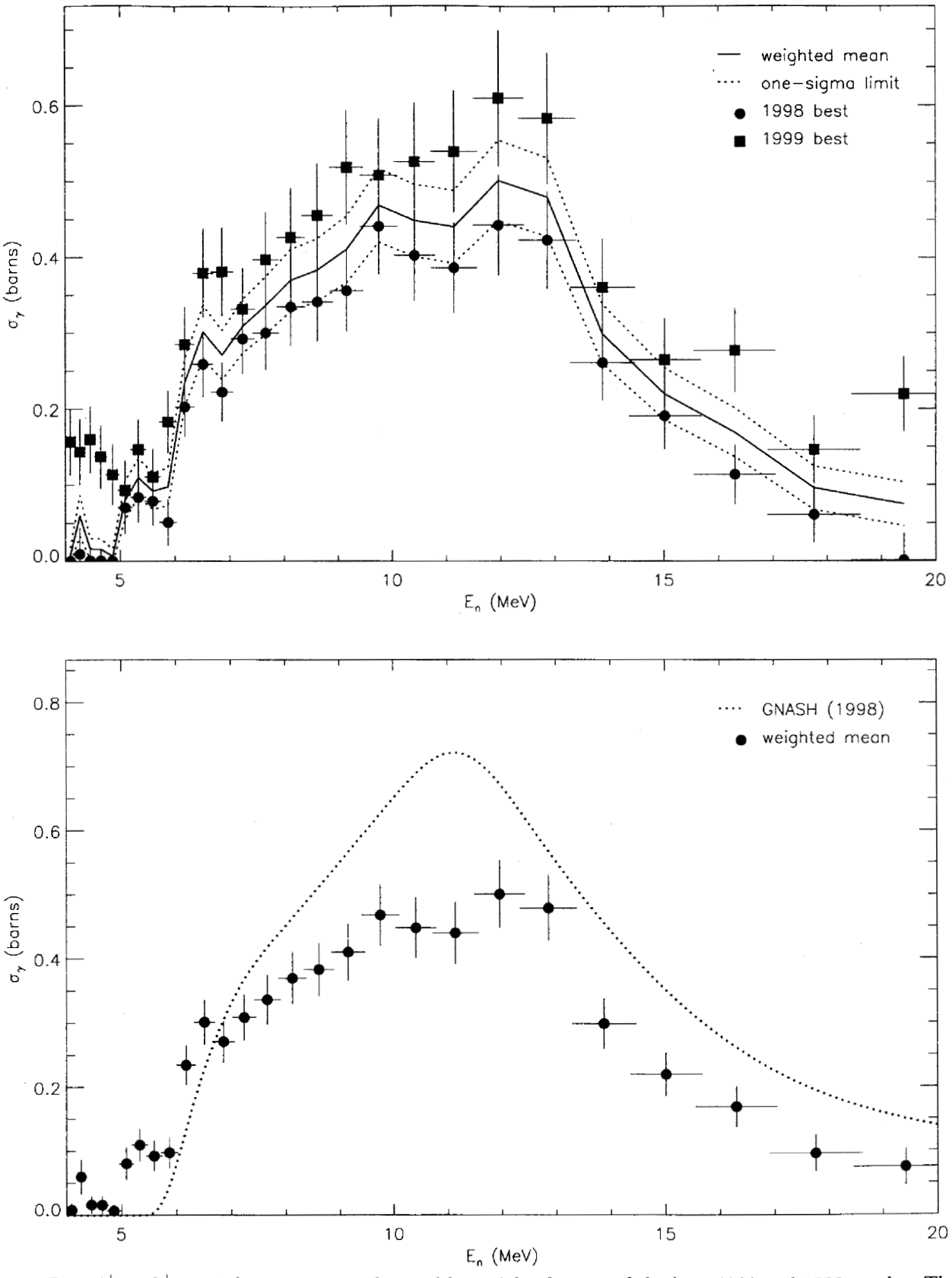

FIG. 41: Best $4_1^+ \rightarrow 2_1^+$ partial cross section obtained by weighted mean of the best 1998 and 1999 results. The top panel shows the 1998 and 1999 partial cross sections and the weighted mean, plotted as a solid line with a one-sigma confidence band. The bottom panel shows the same weighted-mean partial cross section compared to GNASH.

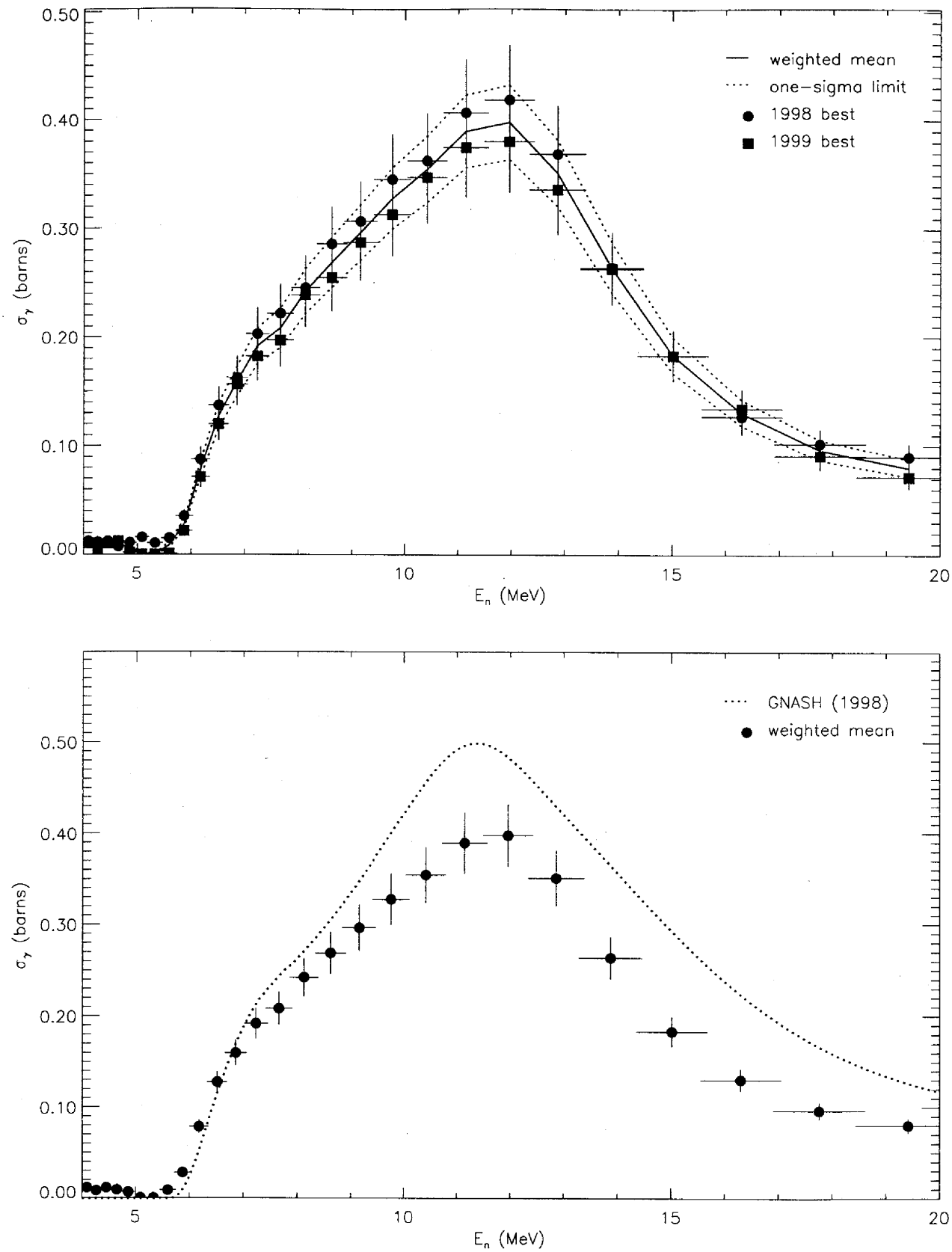

FIG. 42: Best $6_1^+ \rightarrow 4_1^+$ partial cross section obtained by weighted mean of the best 1998 and 1999 results. The top panel shows the 1998 and 1999 partial cross sections and the weighted mean, plotted as a solid line with a one-sigma confidence band. The bottom panel shows the same weighted-mean partial cross section compared to GNASH.

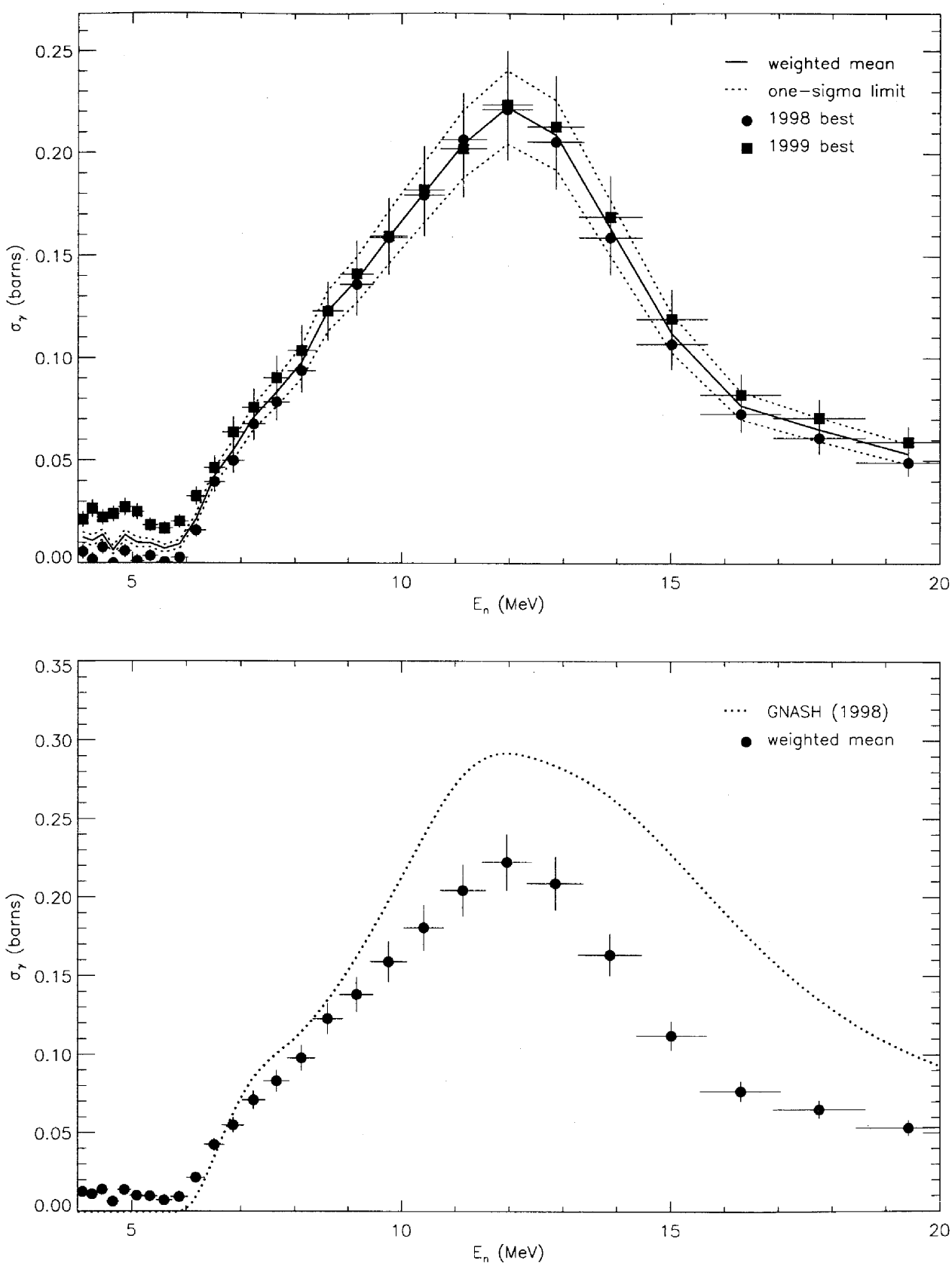

FIG. 43: Best $8_1^+ \rightarrow 6_1^+$ partial cross section obtained by weighted mean of the best 1998 and 1999 results. The top panel shows the 1998 and 1999 partial cross sections and the weighted mean, plotted as a solid line with a one-sigma confidence band. The bottom panel shows the same weighted-mean partial cross section compared to GNASH.

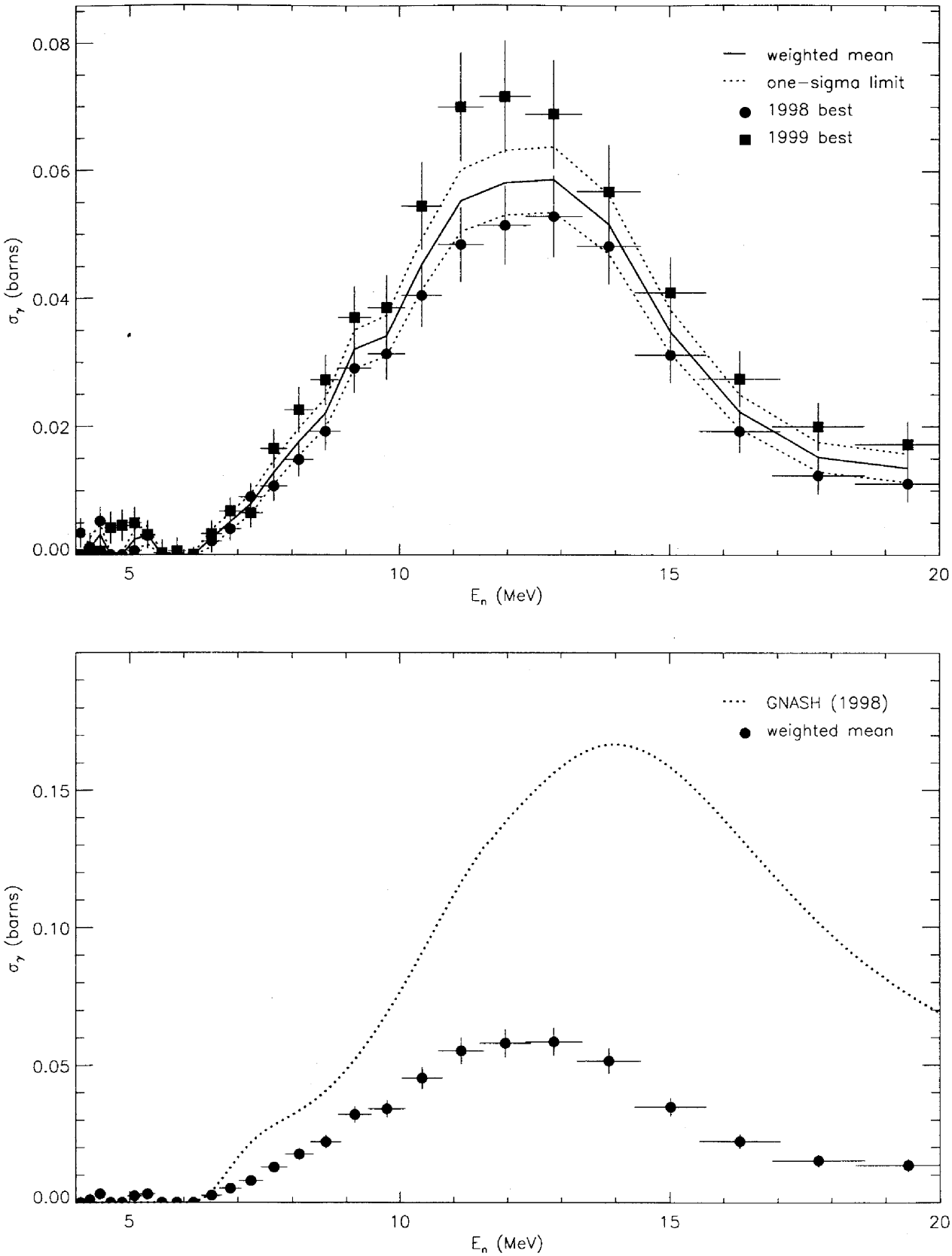

FIG. 44: Best $10_1^+ \rightarrow 8_1^+$ partial cross section obtained by weighted mean of the best 1998 and 1999 results. The top panel shows the 1998 and 1999 partial cross sections and the weighted mean, plotted as a solid line with a one-sigma confidence band. The bottom panel shows the same weighted-mean partial cross section compared to GNASH.

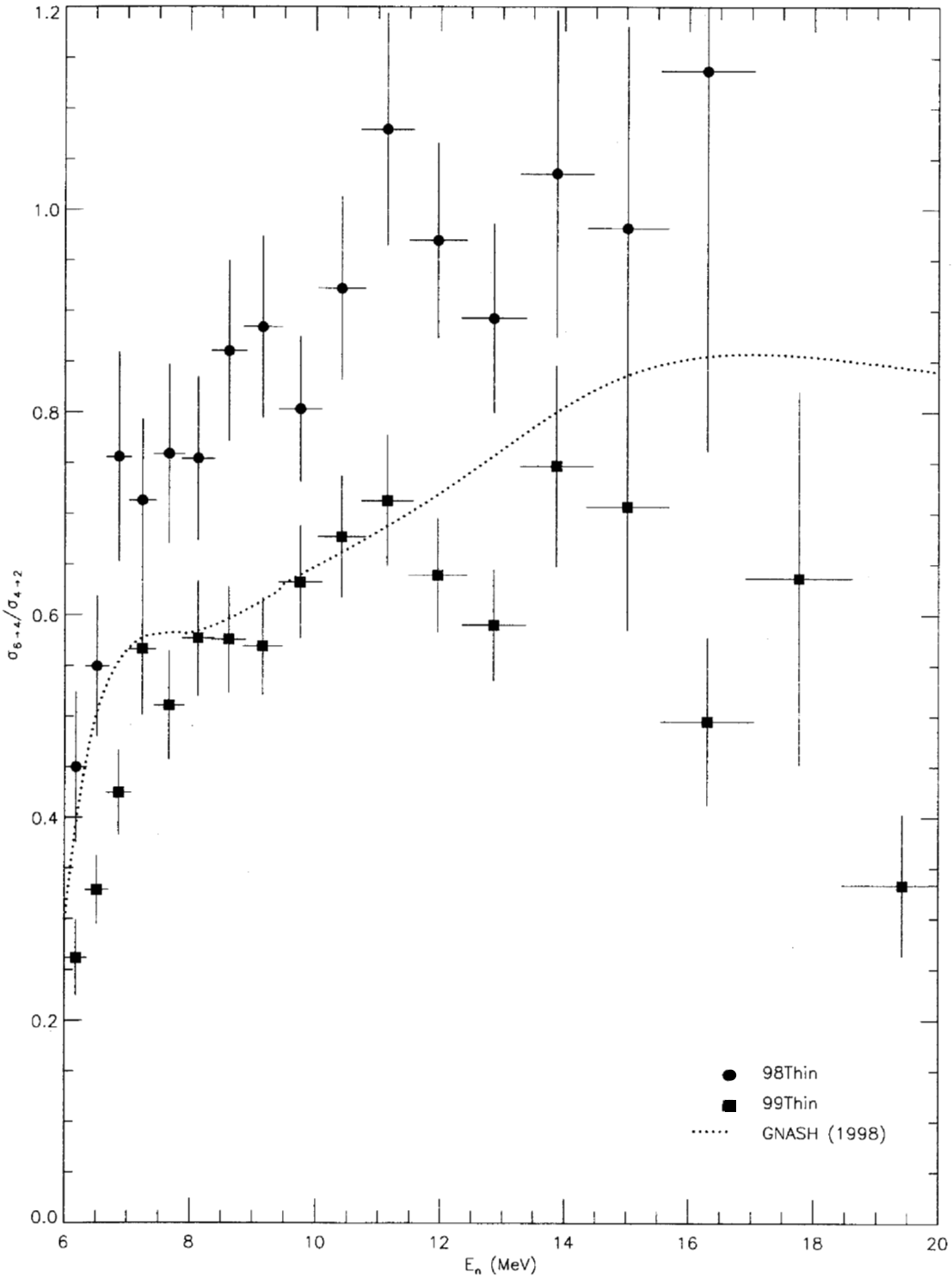

FIG. 45: Ratio of partial γ-ray cross sections $\sigma_{6\to4}/\sigma_{4\to2}$ plotted for the **98Thin** and **99Thin** GEANIE data sets and compared to the GNASH prediction. Angular–distribution corrections are not included.

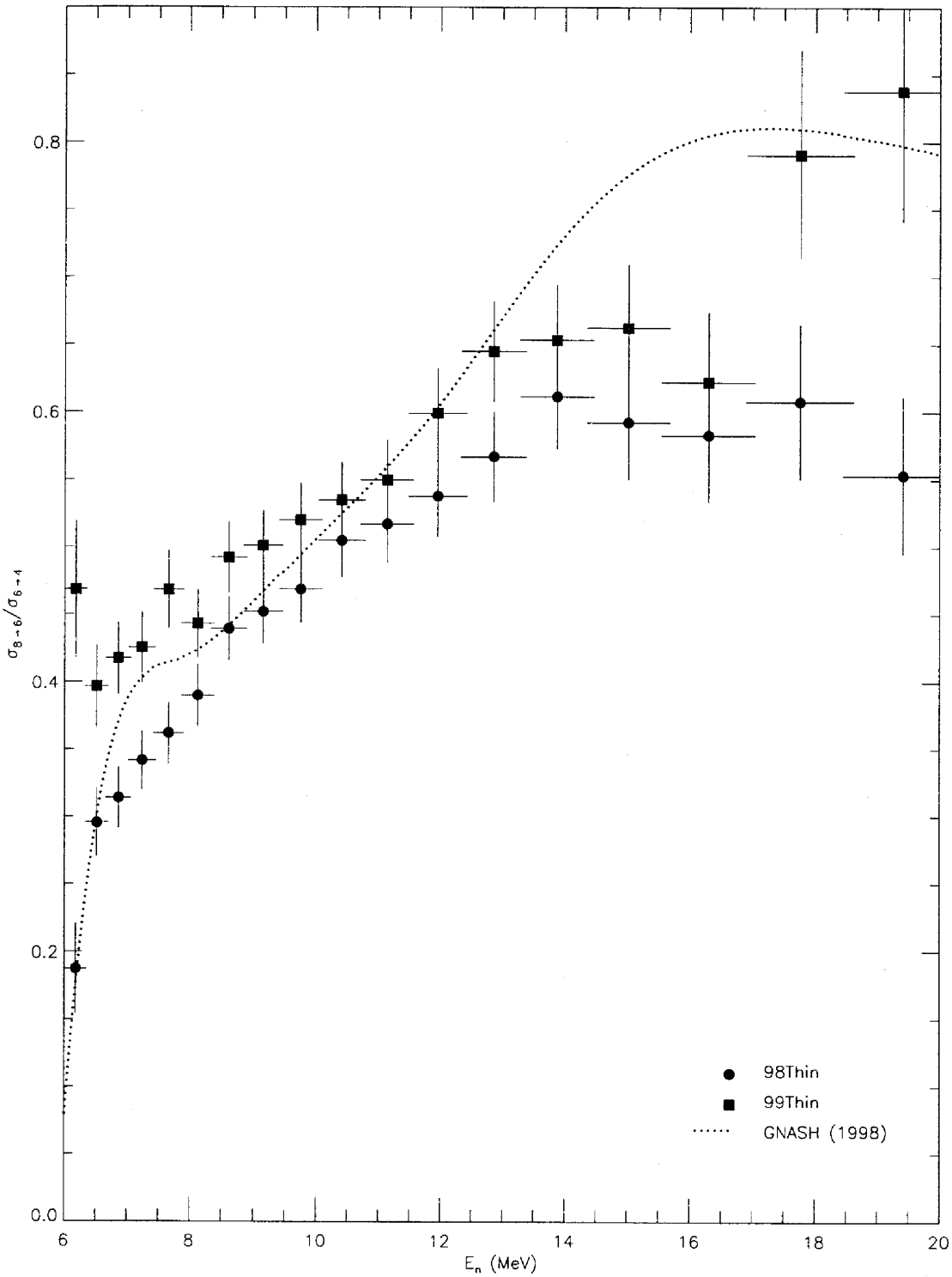

FIG. 46: Ratio of partial γ-ray cross sections $\sigma_{8\to6}/\sigma_{6\to4}$ plotted for the **98Thin** and **99Thin** GEANIE data sets and compared to the GNASH prediction. Angular–distribution corrections are not included.

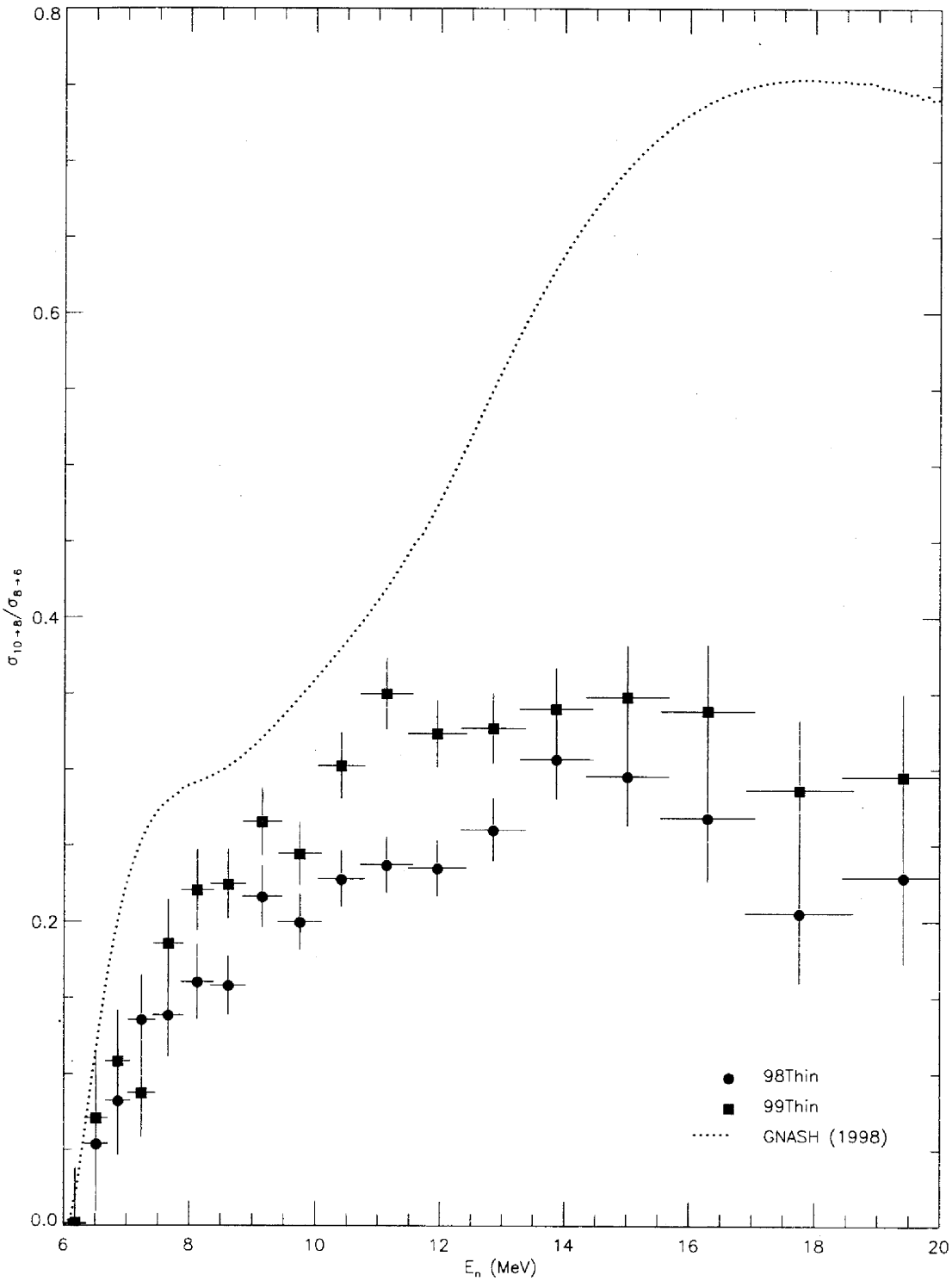

FIG. 47: Ratio of partial γ-ray cross sections $\sigma_{10\to8}/\sigma_{8\to6}$ plotted for the **98Thin** and **99Thin** GEANIE data sets and compared to the GNASH prediction. Angular–distribution corrections are not included.

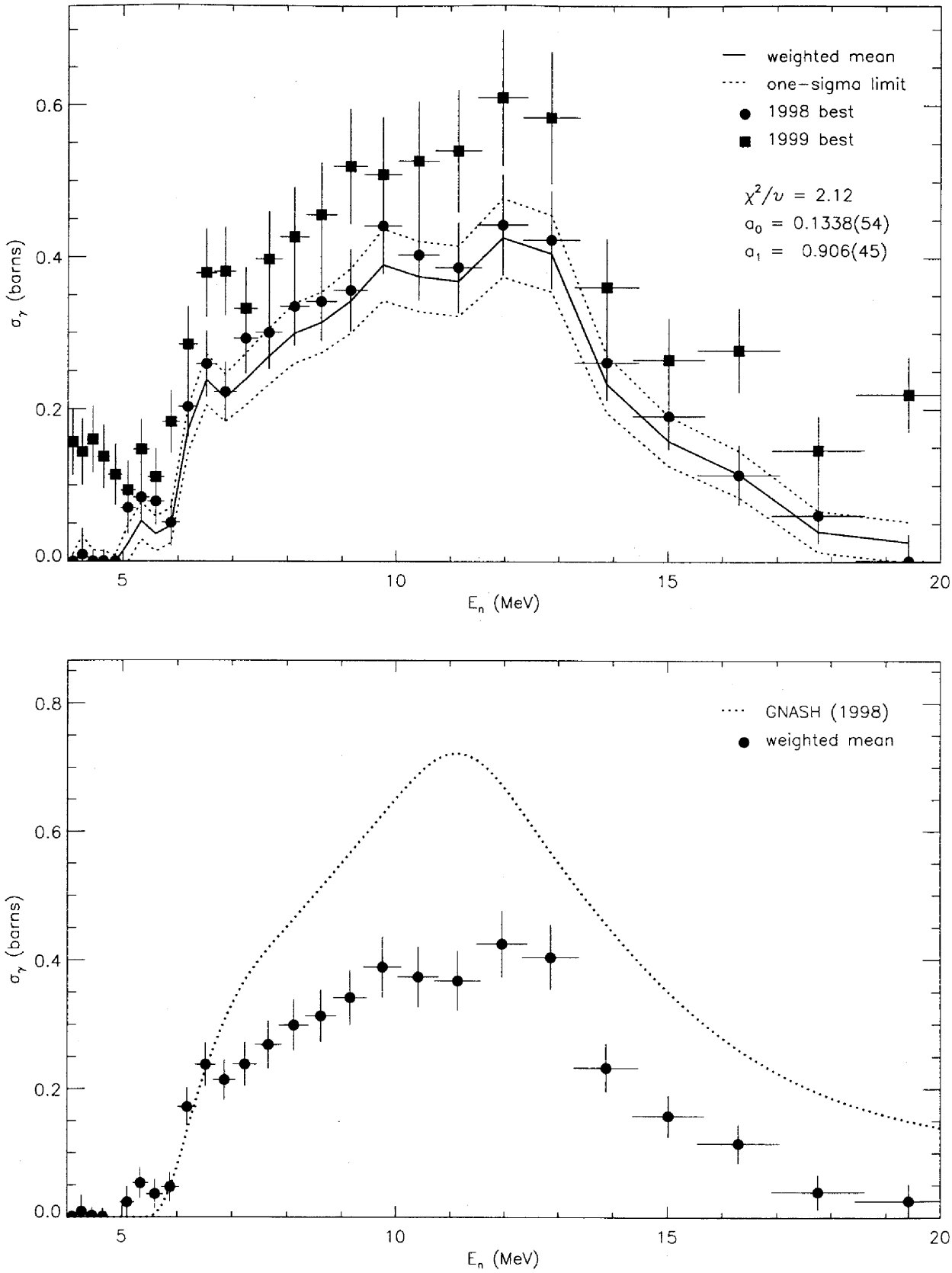

FIG. 48: Best $4_1^+ \rightarrow 2_1^+$ partial cross section obtained by weighted mean of the best 1998 and 1999 results optimized according to equation 23. The top panel shows the adjusted 1998 and 1999 partial cross sections and the weighted mean, plotted as a solid line with a one-sigma confidence band. The bottom panel shows the same weighted-mean partial cross section compared to GNASH.

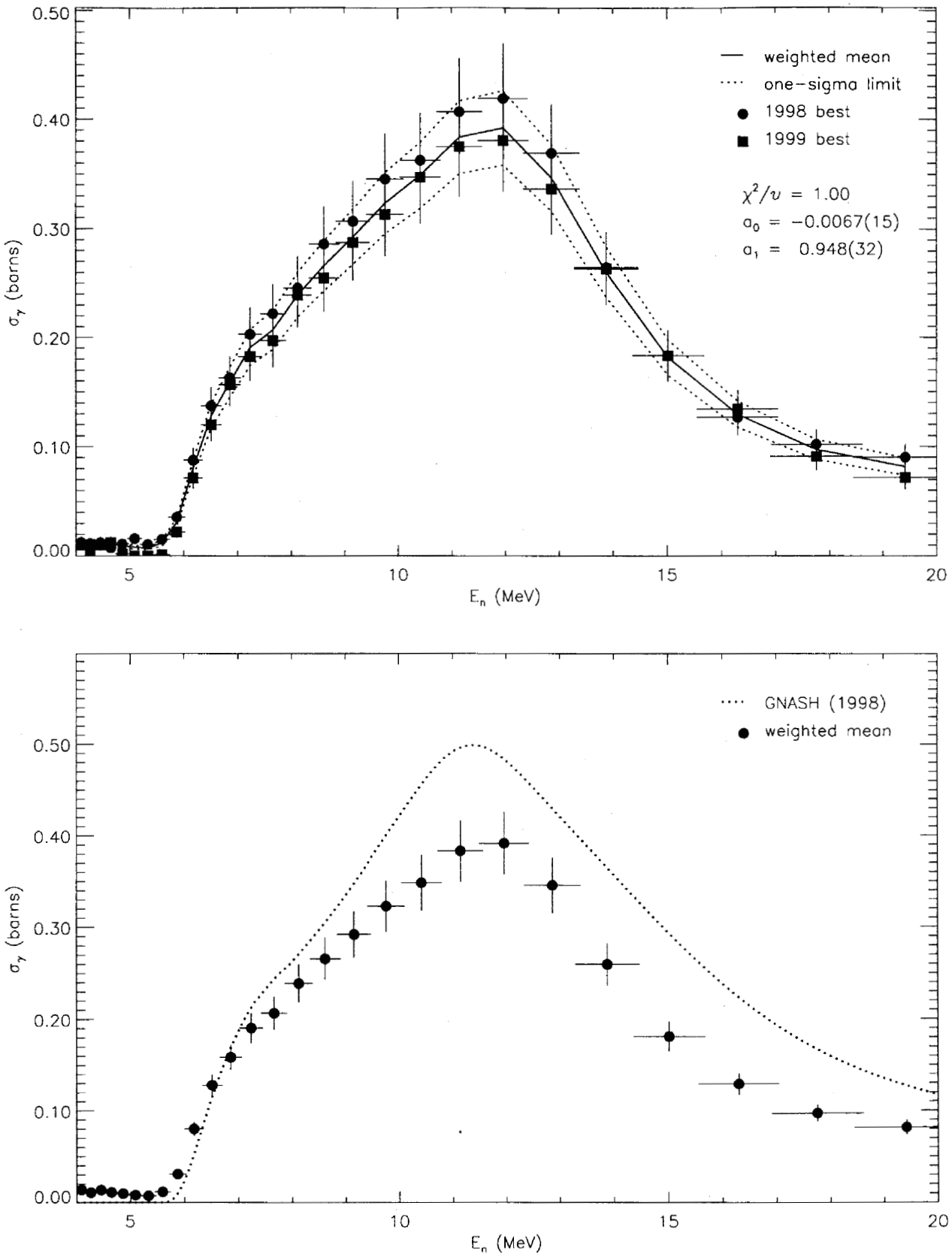

FIG. 49: Best $6_1^+ \rightarrow 4_1^+$ partial cross section obtained by weighted mean of the best 1998 and 1999 results optimized according to equation 23. The top panel shows the adjusted 1998 and 1999 partial cross sections and the weighted mean, plotted as a solid line with a one-sigma confidence band. The bottom panel shows the same weighted-mean partial cross section compared to GNASH.

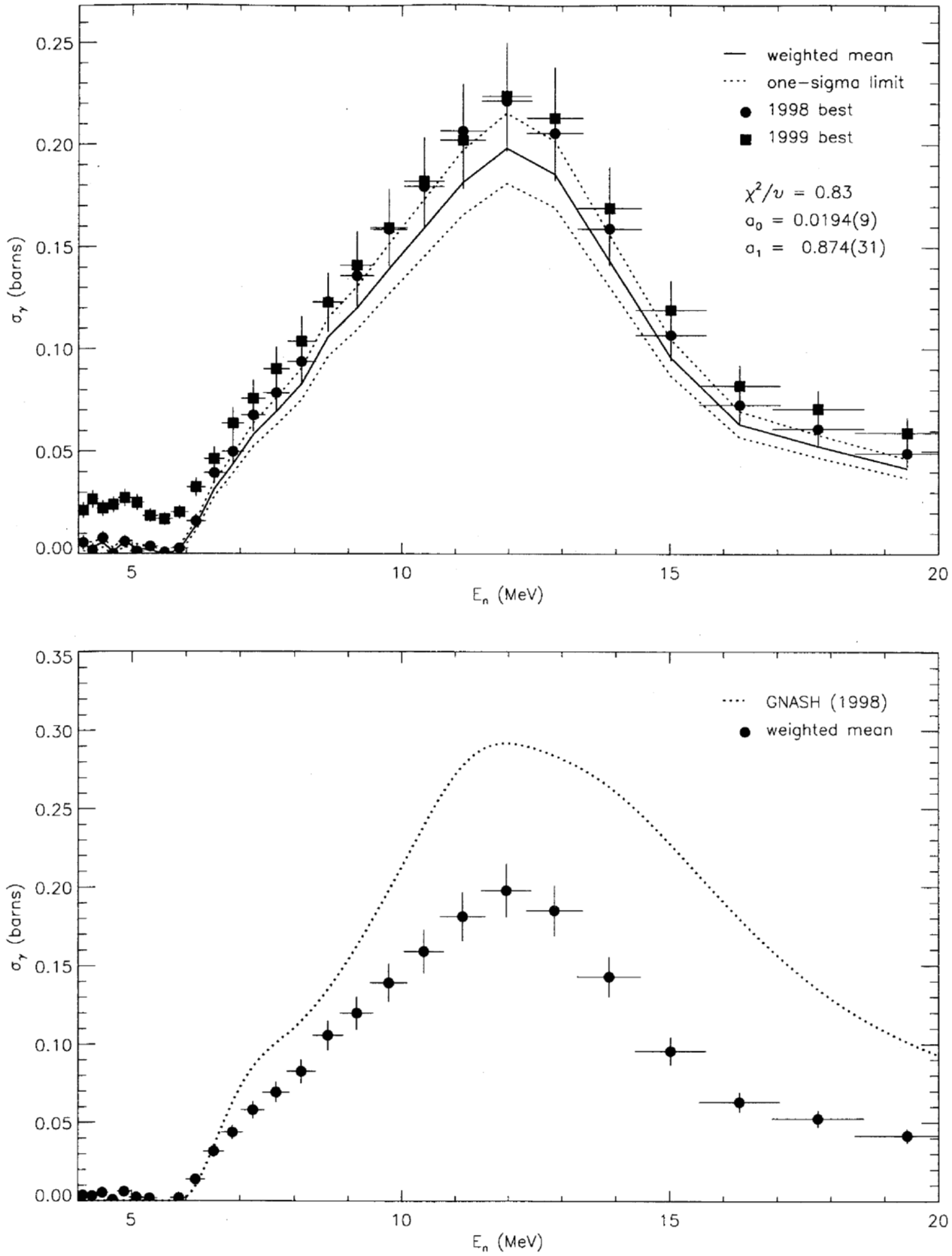

FIG. 50: Best $8_1^+ \rightarrow 6_1^+$ partial cross section obtained by weighted mean of the best 1998 and 1999 results optimized according to equation 23. The top panel shows the adjusted 1998 and 1999 partial cross sections and the weighted mean, plotted as a solid line with a one-sigma confidence band. The bottom panel shows the same weighted-mean partial cross section compared to GNASH.

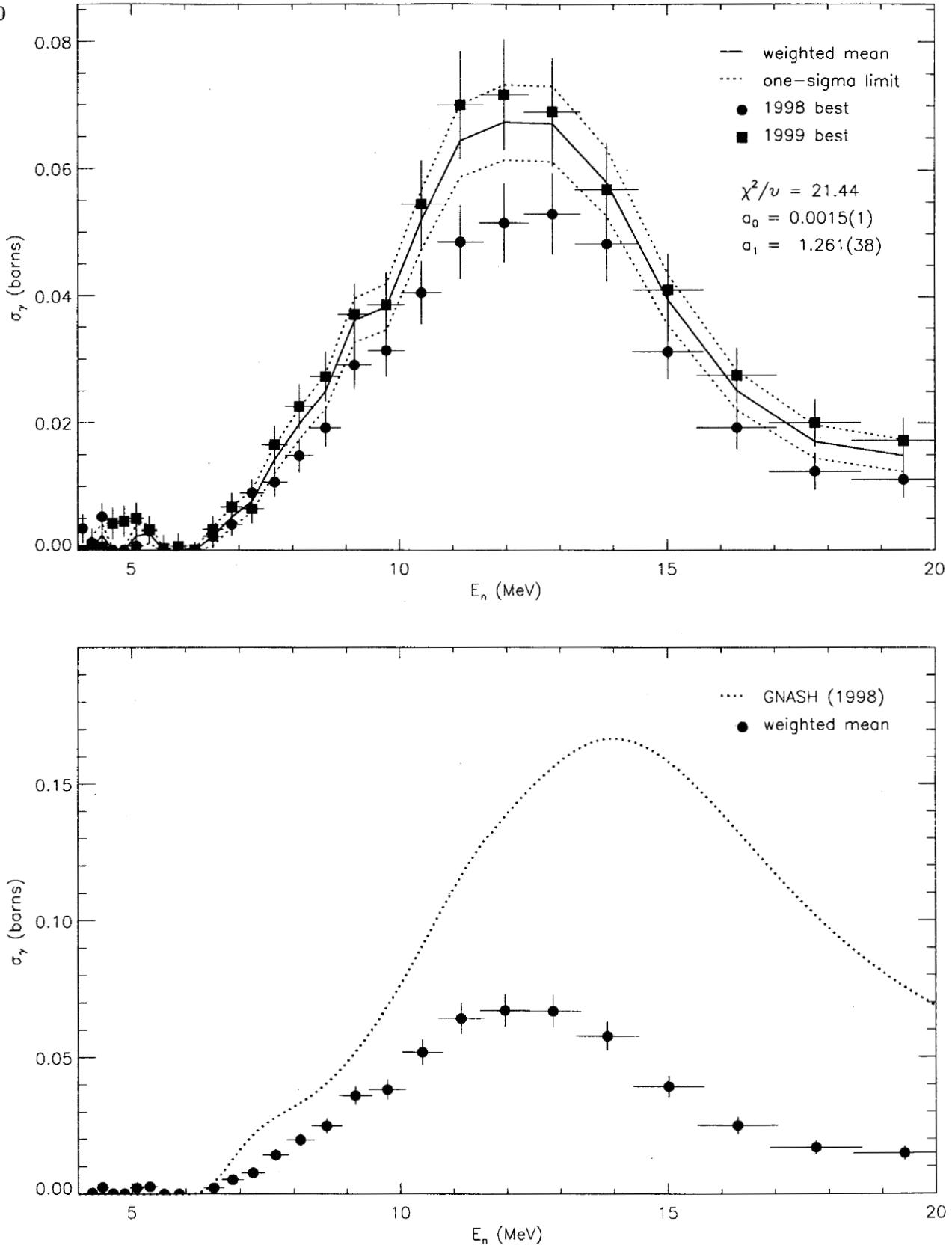

FIG. 51: Best $10_1^+ \rightarrow 8_1^+$ partial cross section obtained by weighted mean of the best 1998 and 1999 results optimized according to equation 23. The top panel shows the adjusted 1998 and 1999 partial cross sections and the weighted mean, plotted as a solid line with a one-sigma confidence band. The bottom panel shows the same weighted-mean partial cross section compared to GNASH.

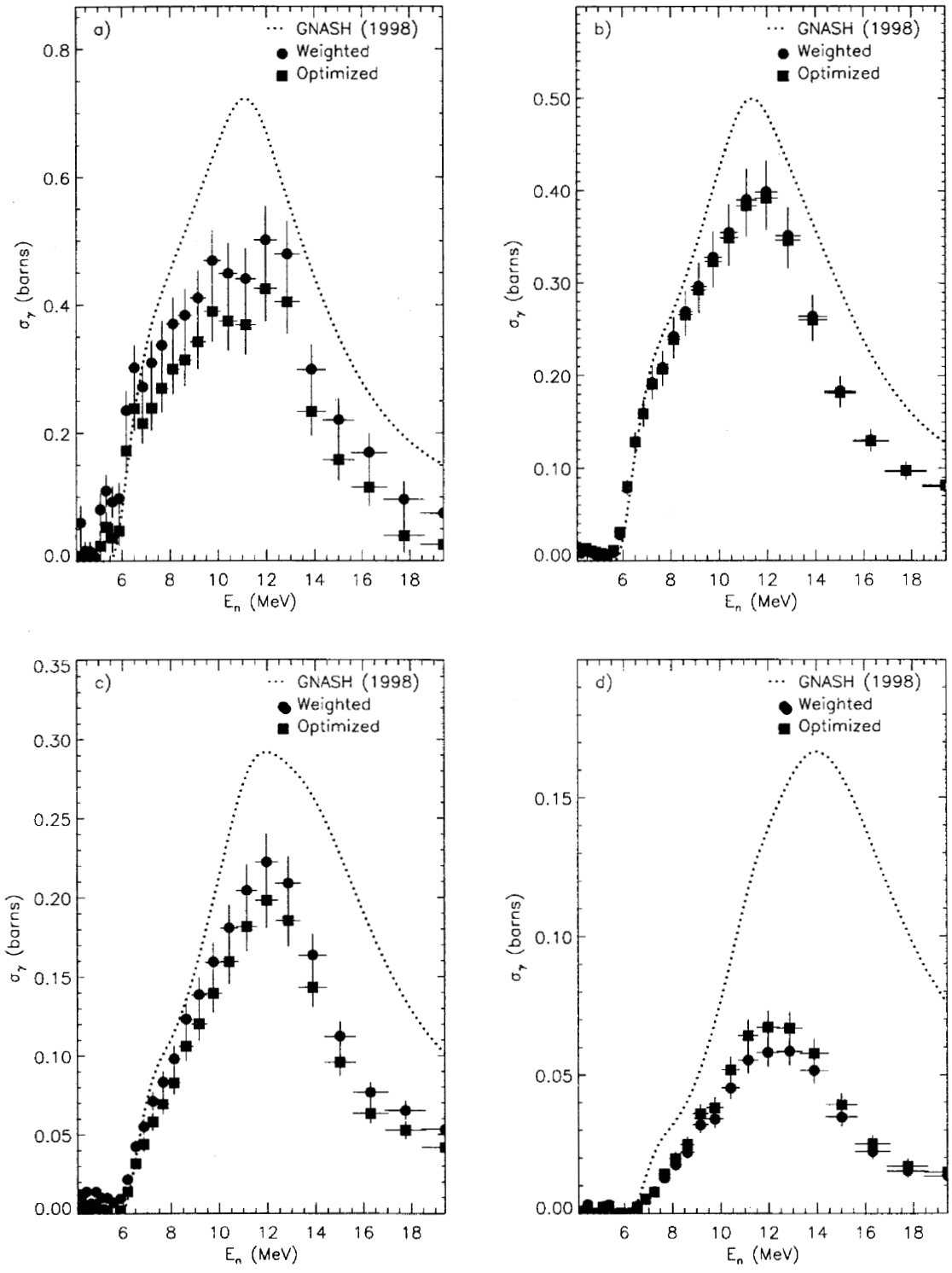

FIG. 52: Comparison of recommended partial γ-ray cross sections obtained from either the weighted **98Thin** and **99Thin**, as discussed in section XII A or from the optimized data, as discussed in section XII B. The data shown are for the a) $4 \rightarrow 2$, b) $6 \rightarrow 4$, c) $8 \rightarrow 6$, and d) $10 \rightarrow 8$ transitions.

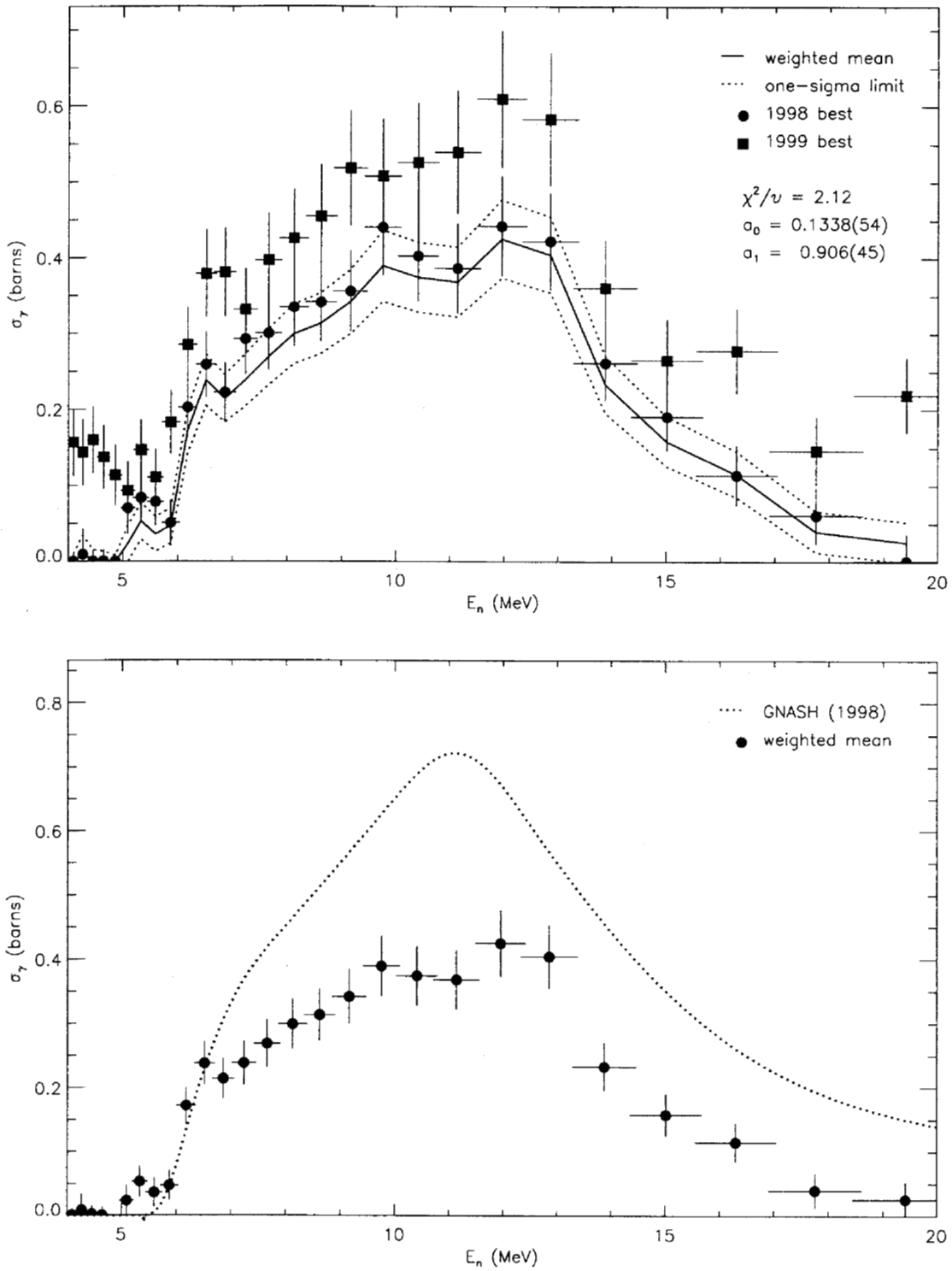

FIG. 54: Adopted E_γ = 100.0–keV partial cross section corresponding to the data in table LXIV. The top panel shows the 1998 and 1999 partial cross sections (corrected for angular–distribution effects) and the recommended value, plotted as a solid line with a one-sigma confidence band (dotted lines). The bottom panel shows this recommended partial cross section (solid circles) compared to GNASH.

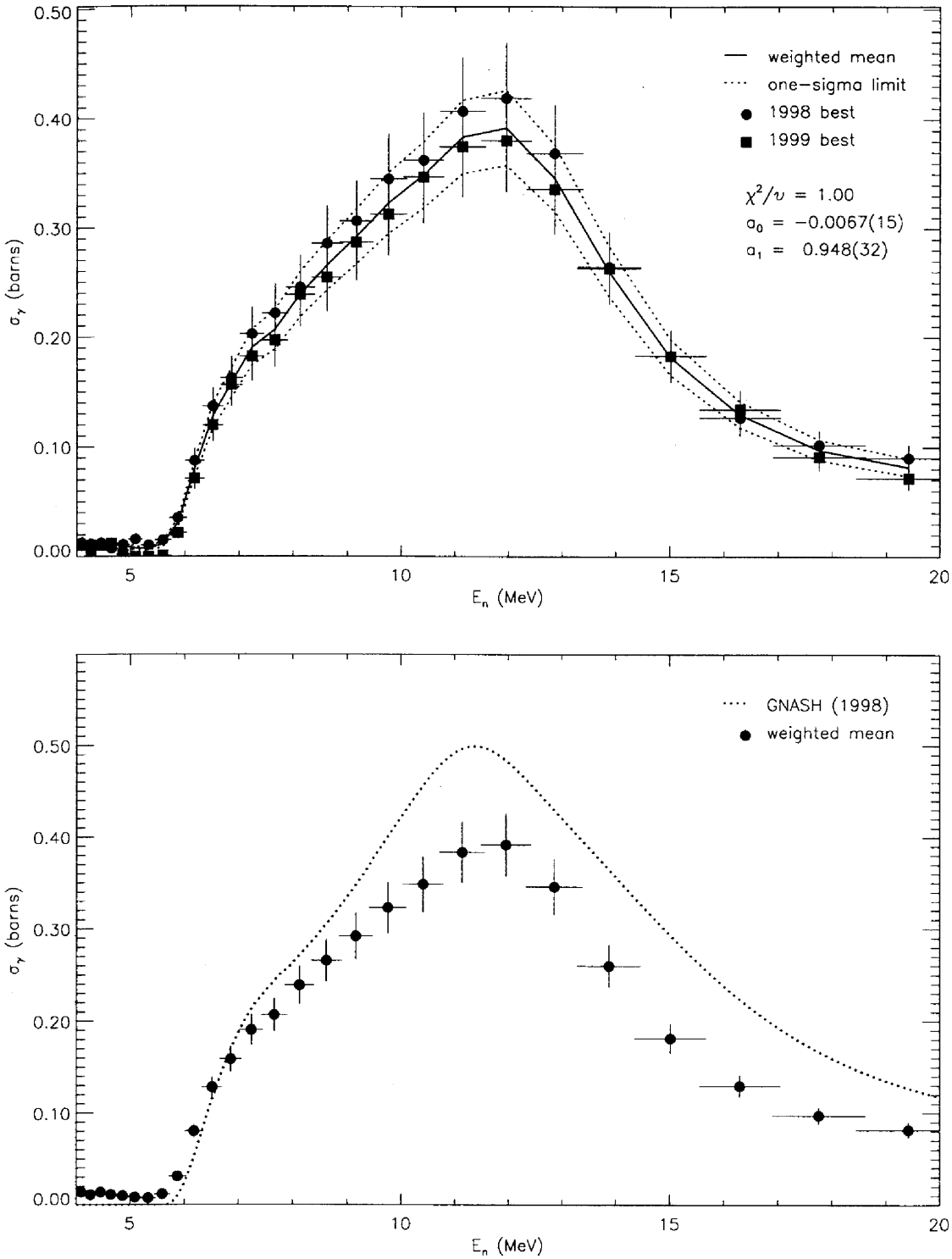

FIG. 56: Adopted E_γ = 152.7–keV partial cross section corresponding to the data in table LXVI. The top panel shows the 1998 and 1999 partial cross sections (corrected for angular–distribution effects) and the recommended value, plotted as a solid line with a one-sigma confidence band (dotted lines). The bottom panel shows this recommended partial cross section (solid circles) compared to GNASH.

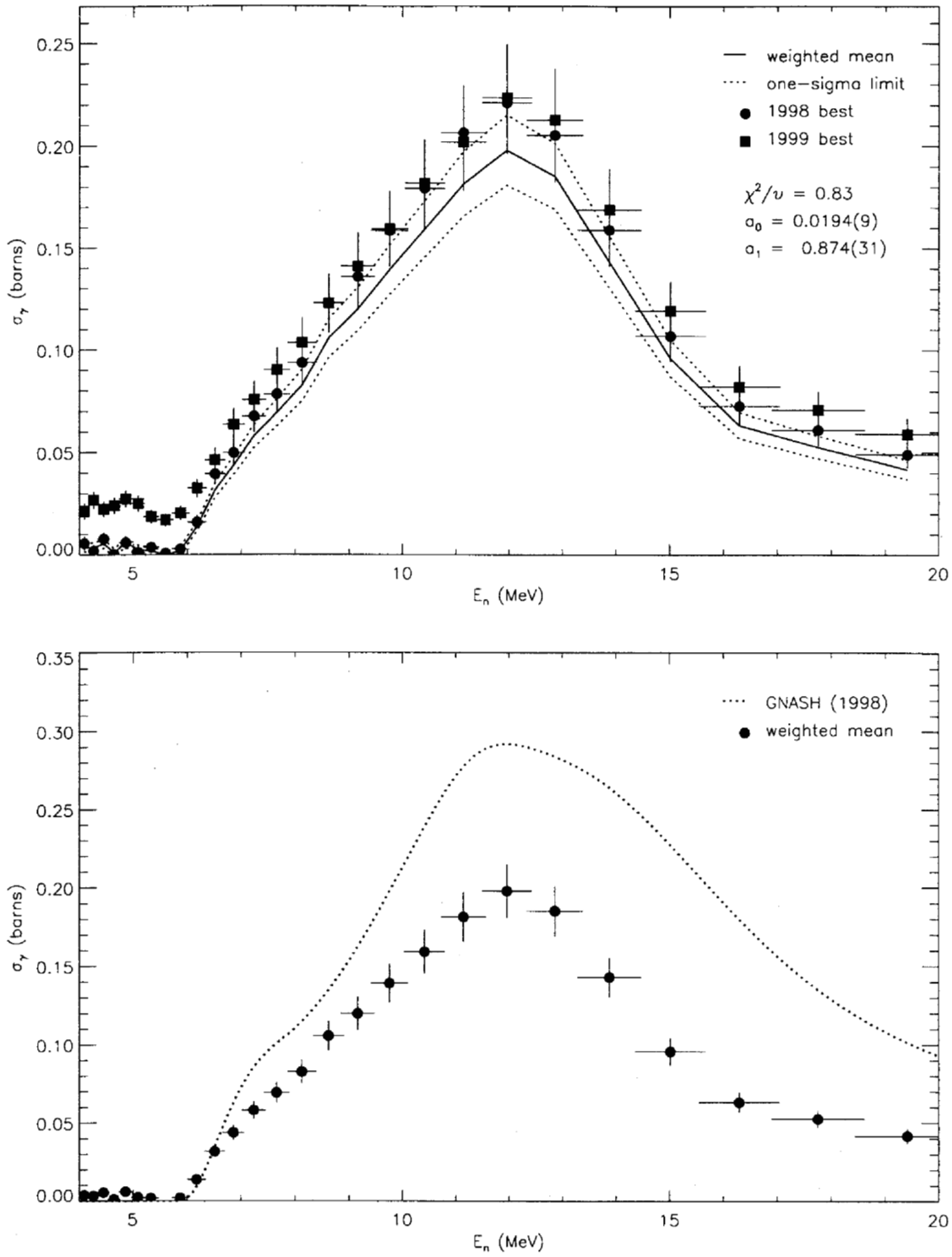

FIG. 57: Adopted E_γ = 201.0–keV partial cross section corresponding to the data in table LXVII. The top panel shows the 1998 and 1999 partial cross sections (corrected for angular–distribution effects) and the recommended value, plotted as a solid line with a one-sigma confidence band (dotted lines). The bottom panel shows this recommended partial cross section (solid circles) compared to GNASH.

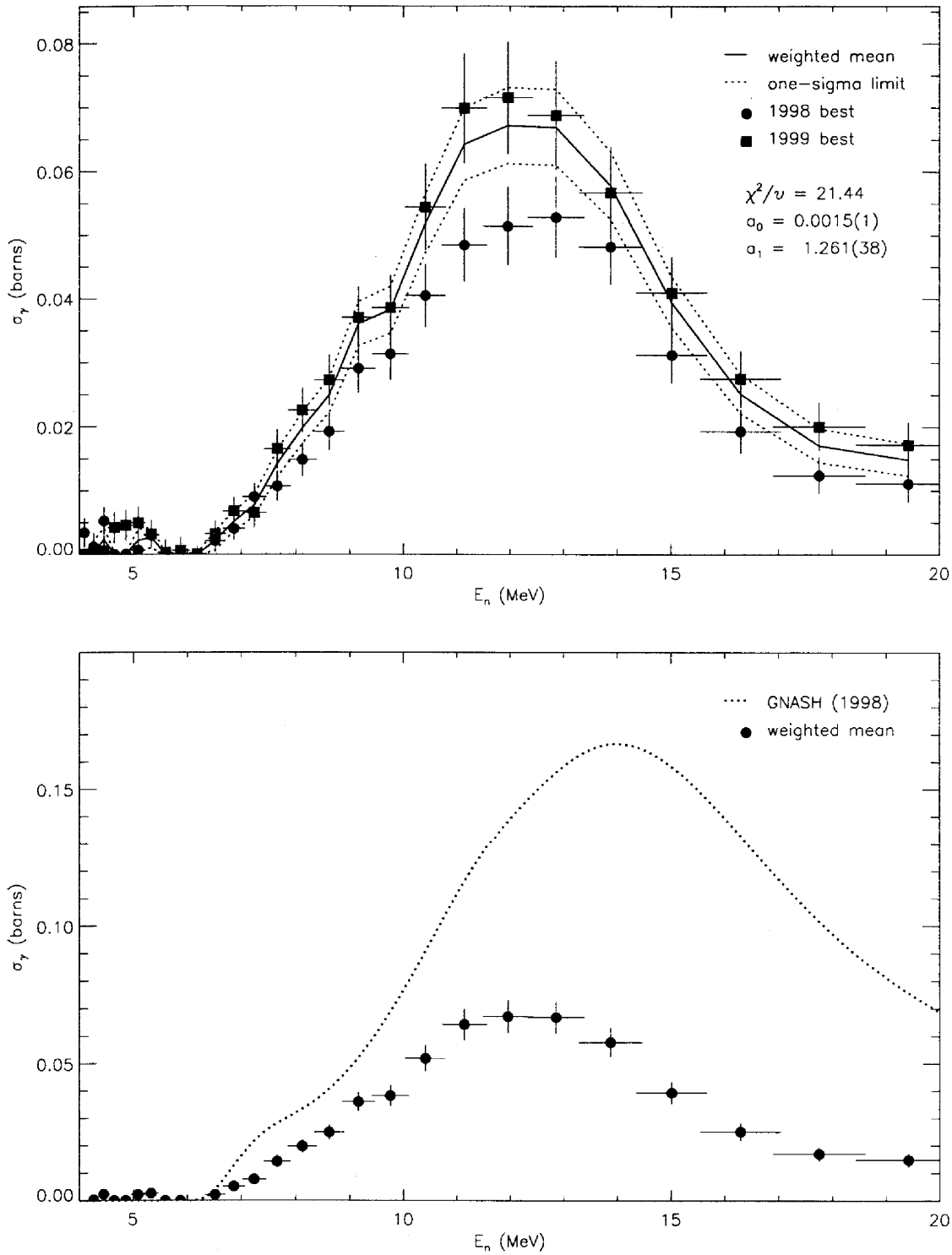

FIG. 58: Adopted E_γ = 244.4–keV partial cross section corresponding to the data in table LXVIII. The top panel shows the 1998 and 1999 partial cross sections (corrected for angular–distribution effects) and the recommended value, plotted as a solid line with a one-sigma confidence band (dotted lines). The bottom panel shows this recommended partial cross section (solid circles) compared to GNASH.

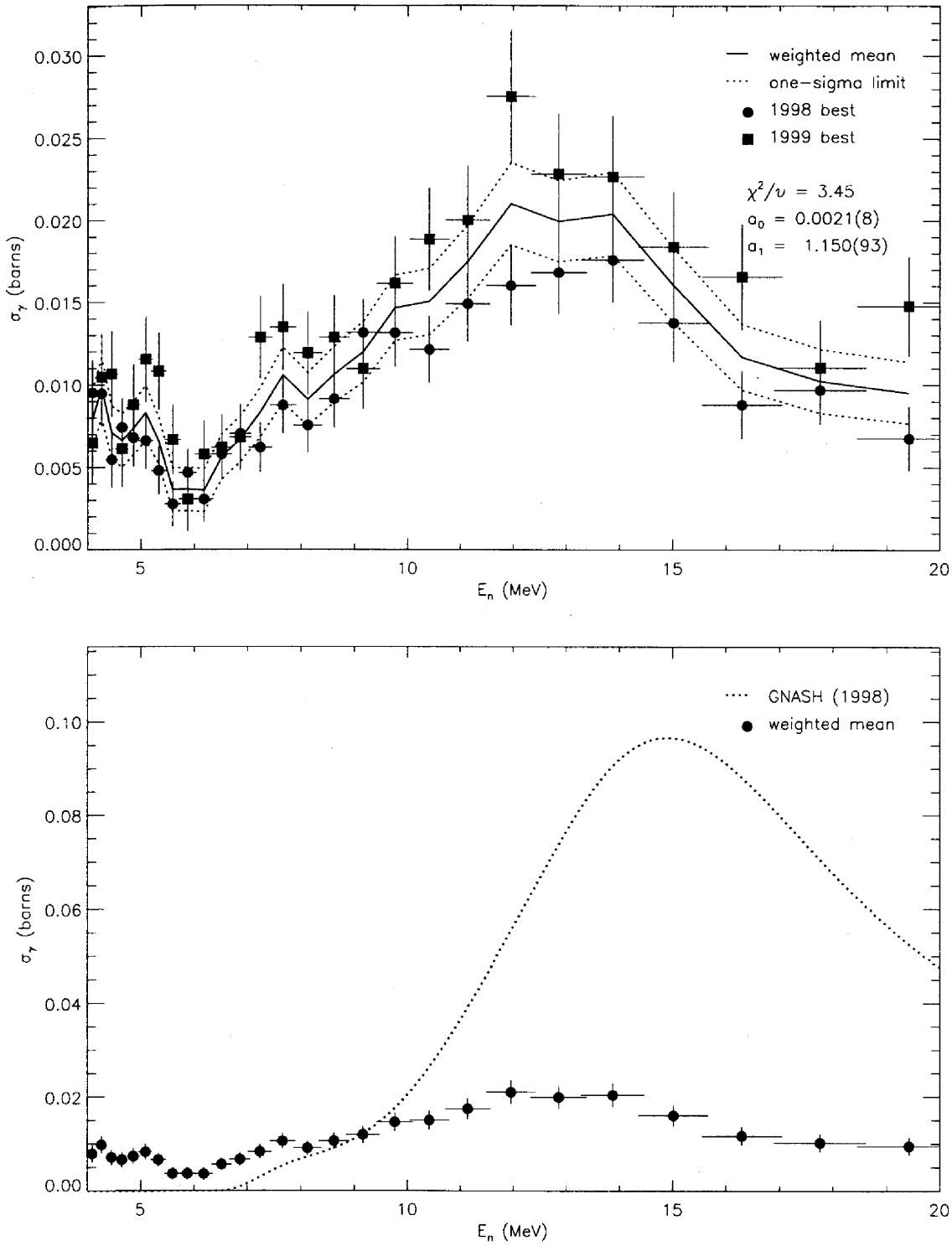

FIG. 59: Adopted E_γ = 282.2-keV partial cross section corresponding to the data in table LXIX. The top panel shows the 1998 and 1999 partial cross sections (corrected for angular–distribution effects) and the recommended value, plotted as a solid line with a one-sigma confidence band (dotted lines). The bottom panel shows this recommended partial cross section (solid circles) compared to GNASH.

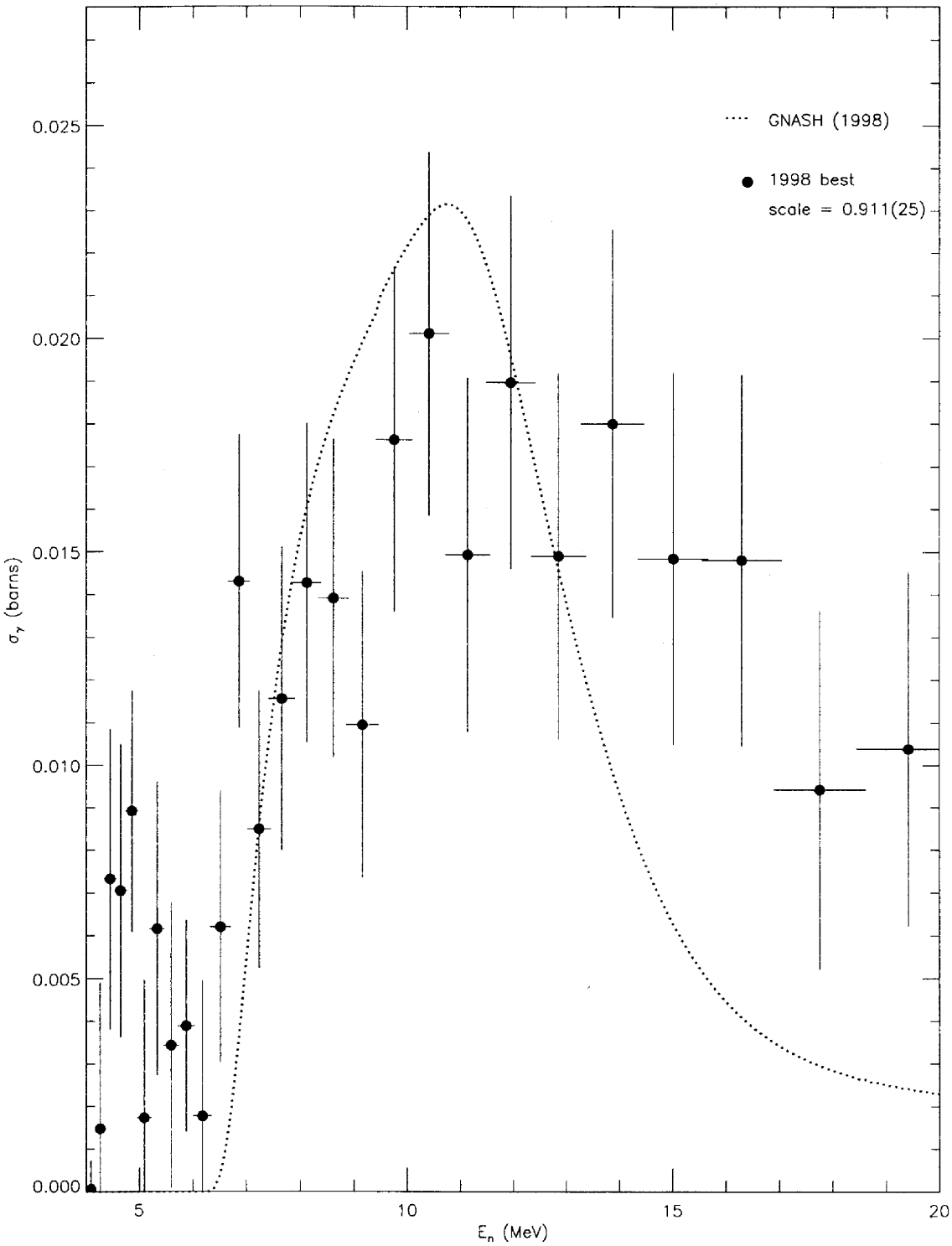

FIG. 60: Adopted E_γ = 666.7–keV partial cross section corresponding to the data in table LXX, and corrected for angular–distribution effects. The target–thickness correction factor is shown, and the recommended partial cross section (solid circles) is compared to GNASH.

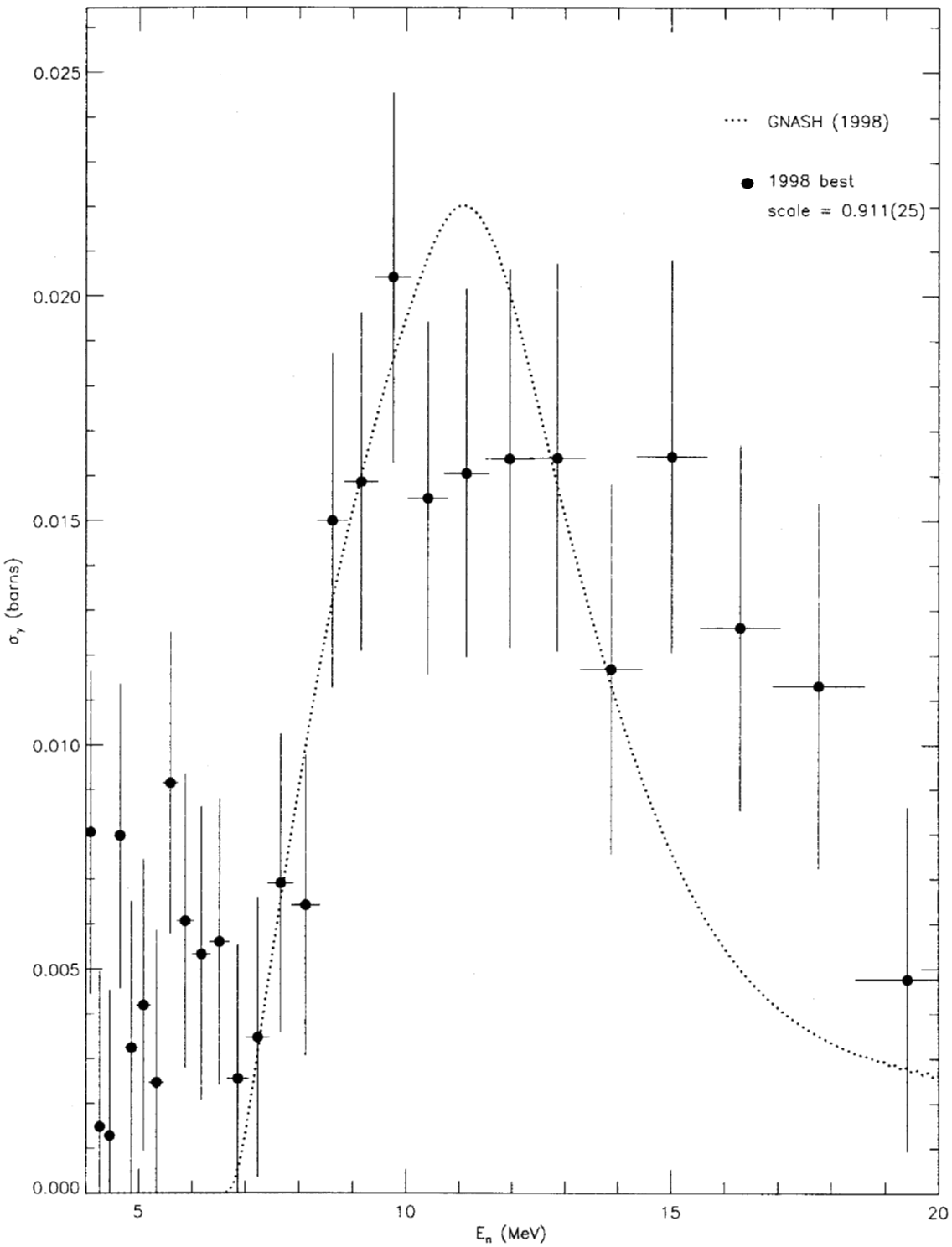

FIG. 61: Adopted E_γ = 780.8–keV partial cross section corresponding to the data in table LXXI, and corrected for angular–distribution effects. The target–thickness correction factor is shown, and the recommended partial cross section (solid circles) is compared to GNASH.

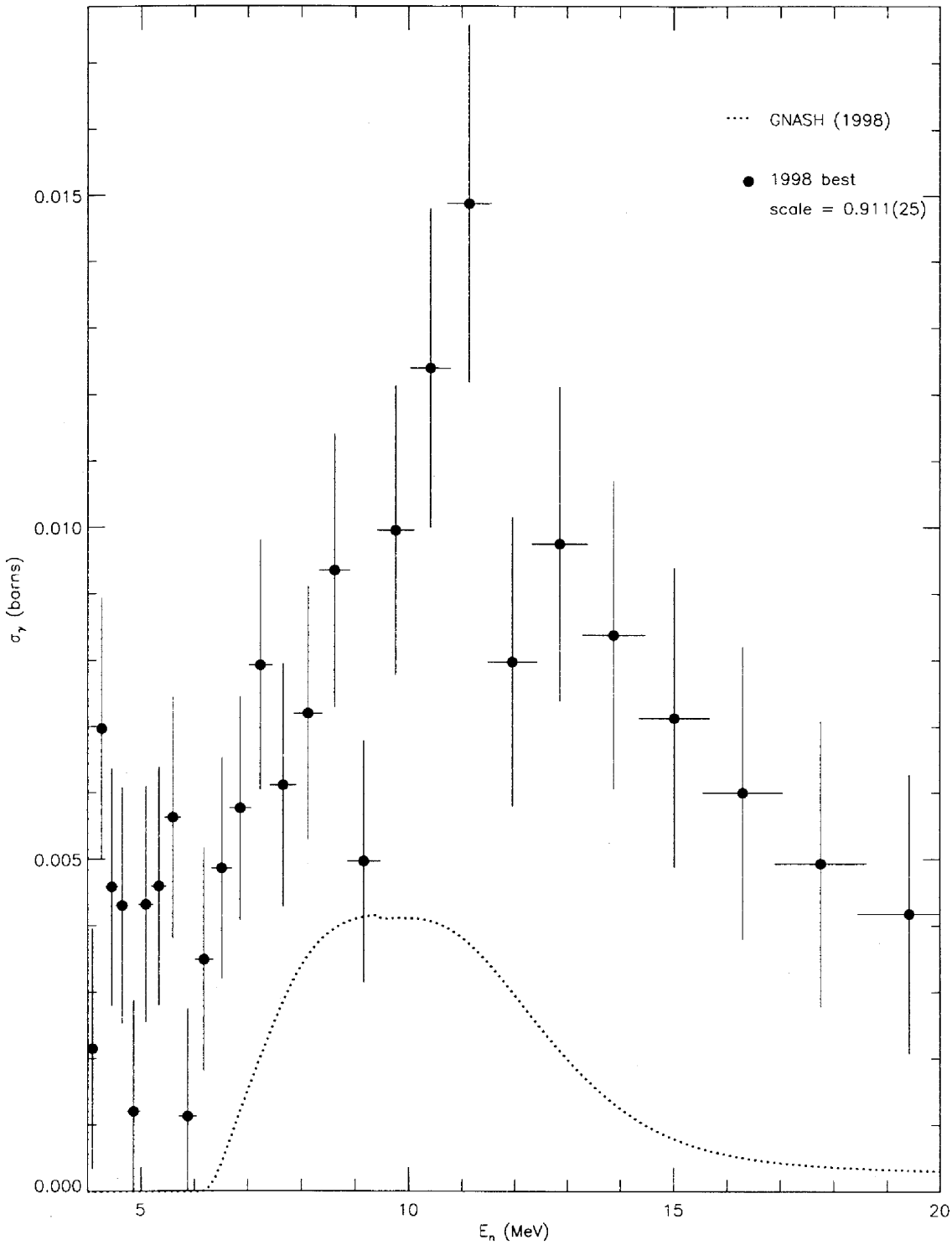

FIG. 62: Adopted E_γ = 786.8–keV partial cross section corresponding to the data in table LXXII, and corrected for angular–distribution effects. The target–thickness correction factor is shown, and the recommended partial cross section (solid circles) is compared to GNASH.

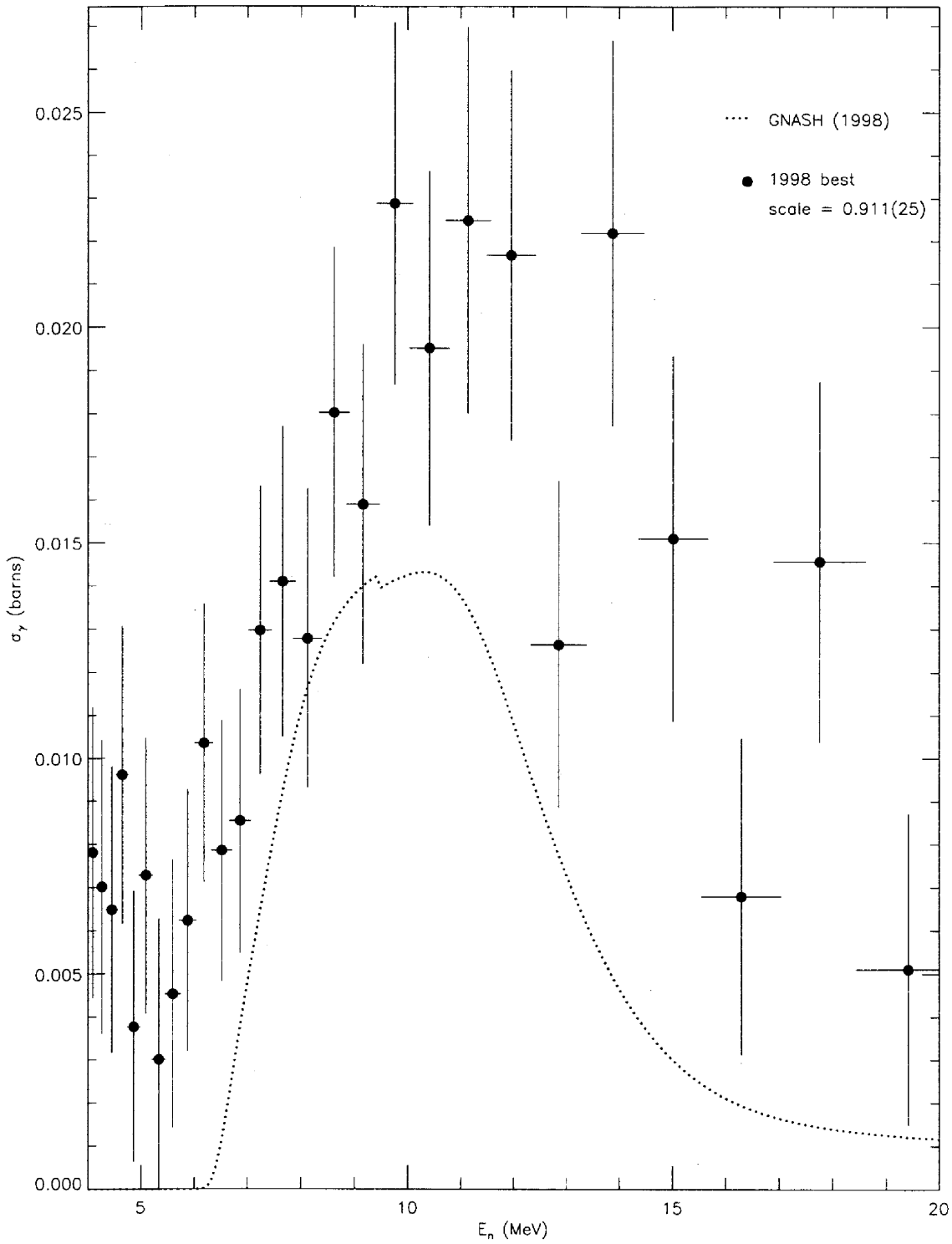

FIG. 63: Adopted E_γ = 806.1–keV partial cross section corresponding to the data in table LXXIII, and corrected for angular–distribution effects. The target–thickness correction factor is shown, and the recommended partial cross section (solid circles) is compared to GNASH.

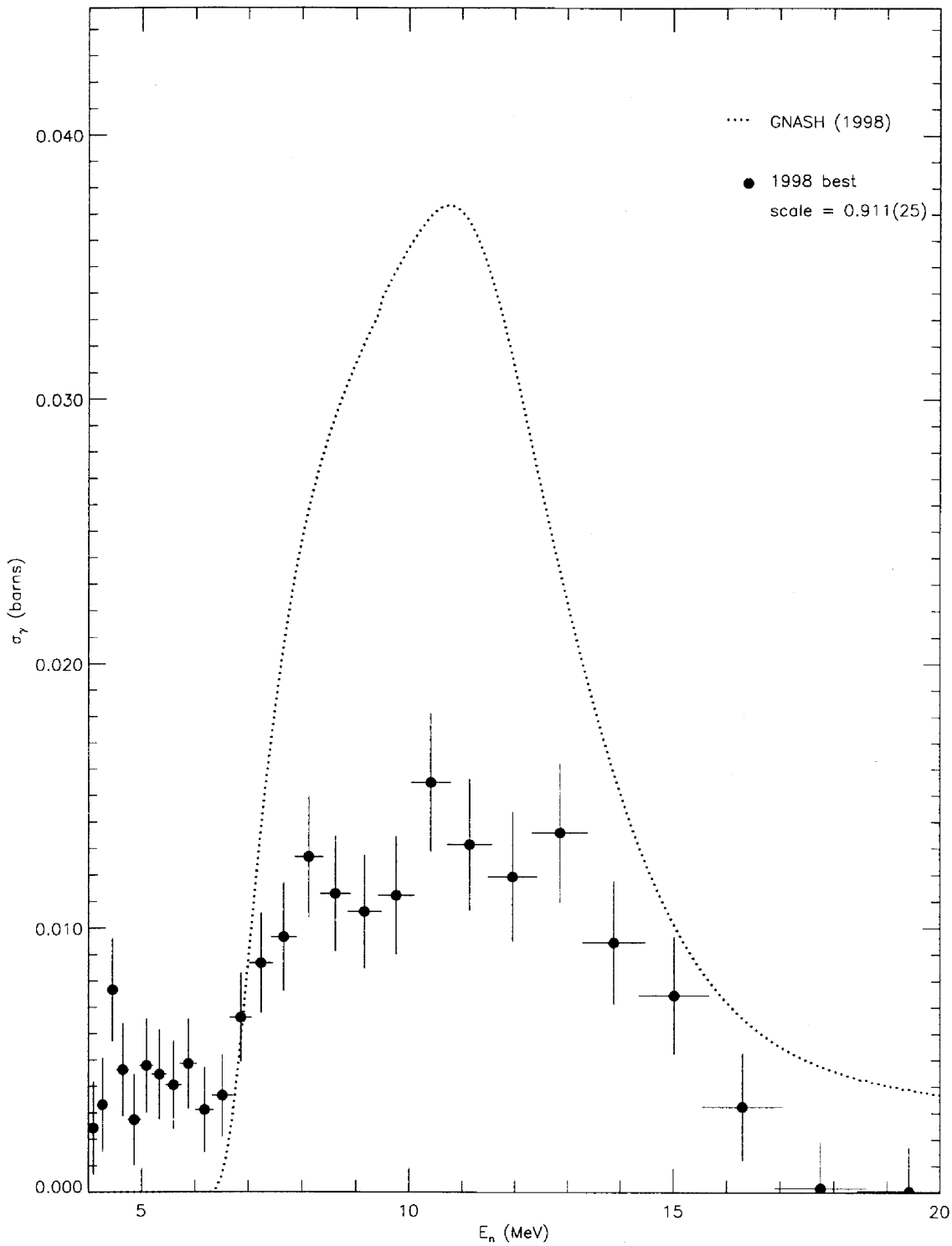

FIG. 64: Adopted E_γ = 819.2–keV partial cross section corresponding to the data in table LXXIV, and corrected for angular–distribution effects. The target–thickness correction factor is shown, and the recommended partial cross section (solid circles) is compared to GNASH.

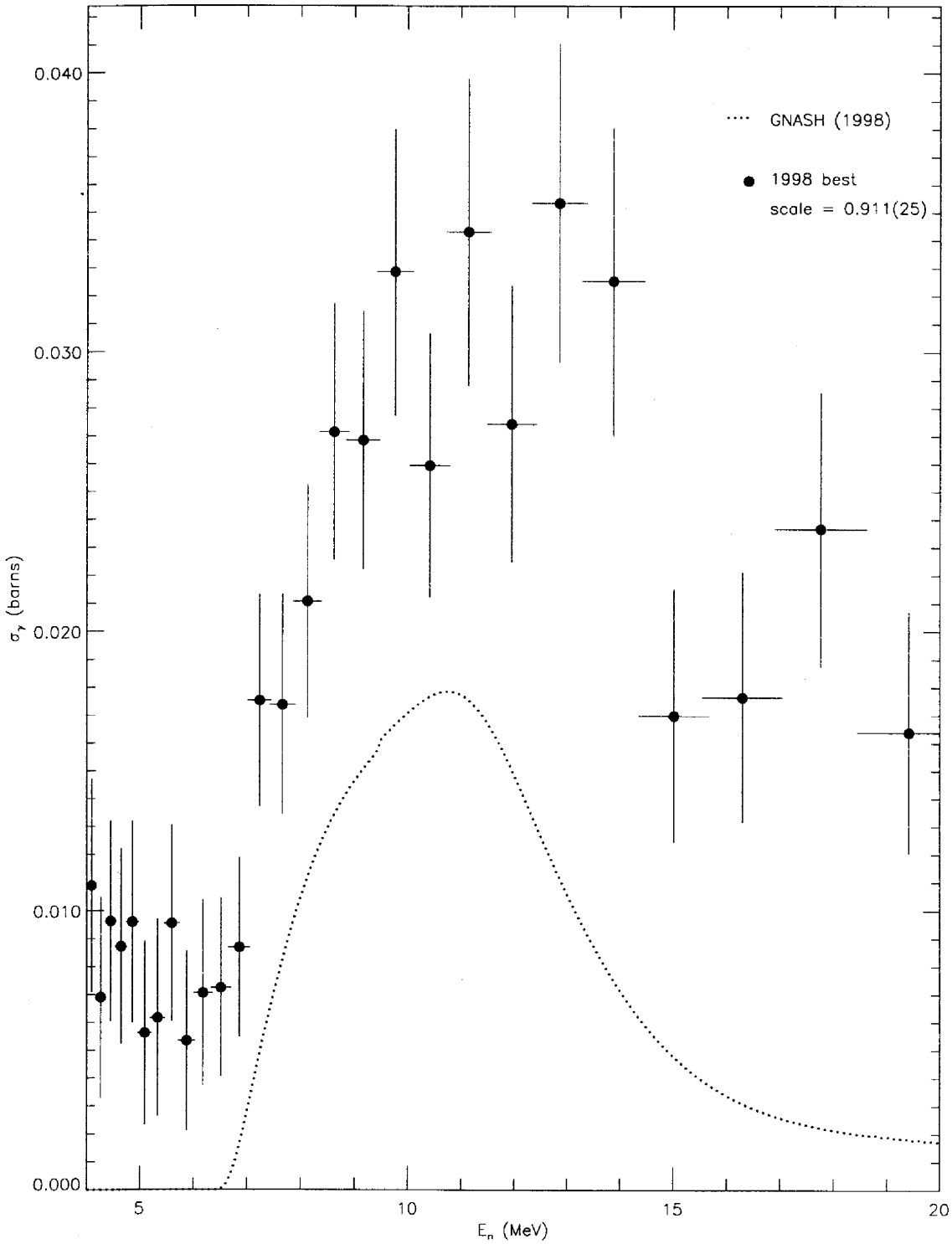

FIG. 66: Adopted E_γ = 831.6–keV partial cross section corresponding to the data in table LXXVI, and corrected for angular–distribution effects. The target–thickness correction factor is shown, and the recommended partial cross section (solid circles) is compared to GNASH.

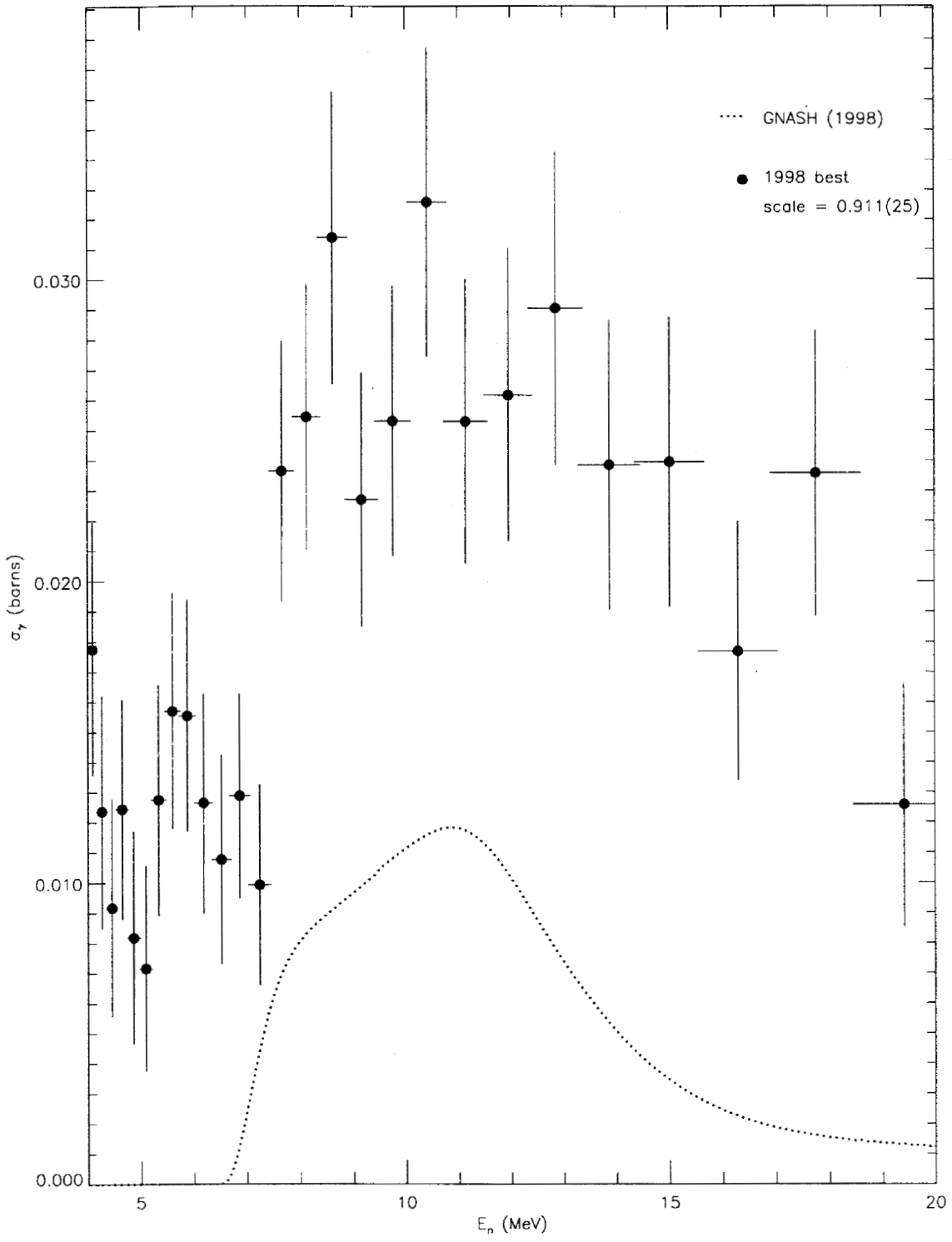

FIG. 67: Adopted E_γ = 875.5–keV partial cross section corresponding to the data in table LXXVII, and corrected for angular–distribution effects. The target–thickness correction factor is shown, and the recommended partial cross section (solid circles) is compared to GNASH.

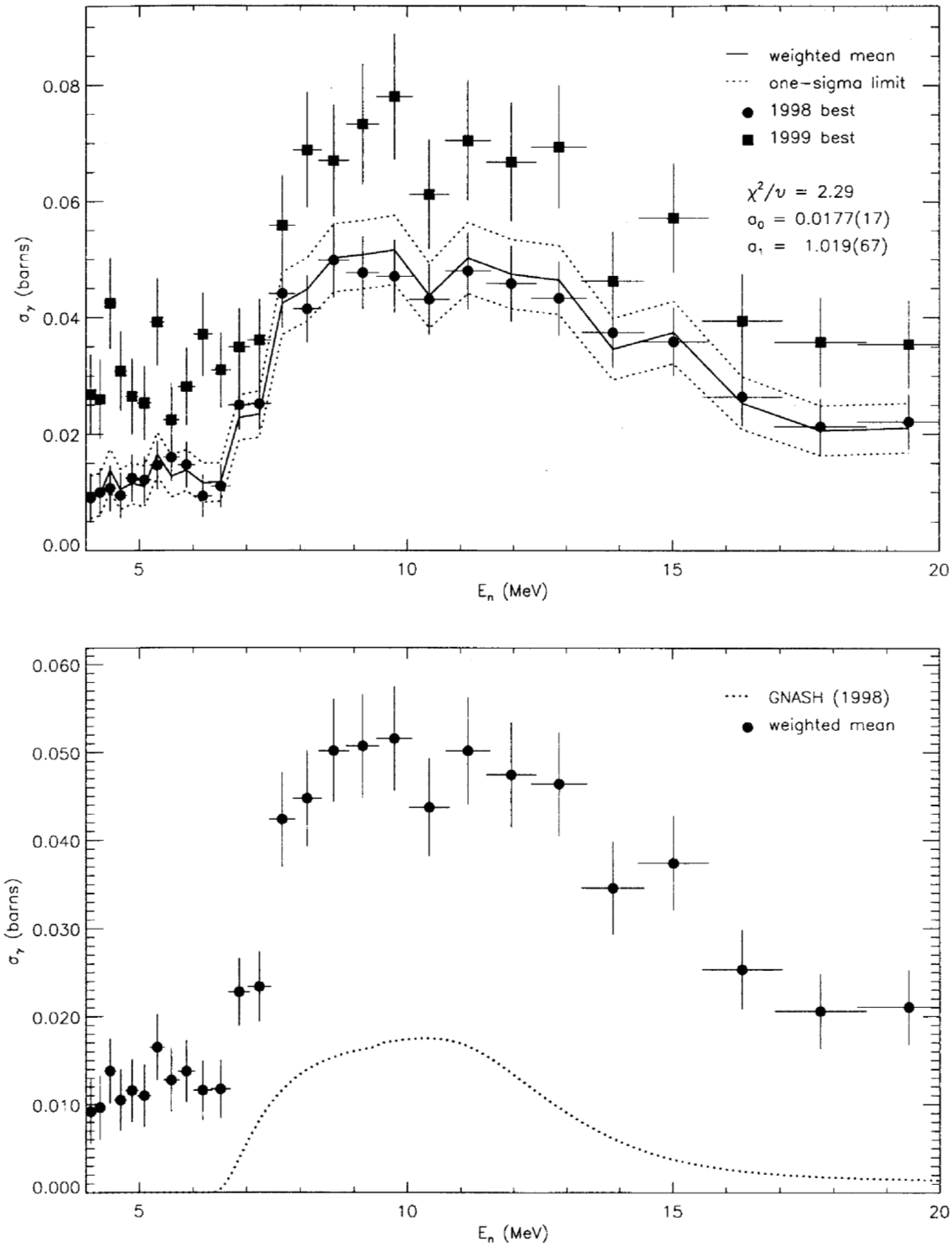

FIG. 68: Adopted E_γ = 880.6–keV partial cross section corresponding to the data in table LXXVIII. The top panel shows the 1998 and 1999 partial cross sections (corrected for angular–distribution effects) and the recommended value, plotted as a solid line with a one-sigma confidence band (dotted lines). The bottom panel shows this recommended partial cross section (solid circles) compared to GNASH.

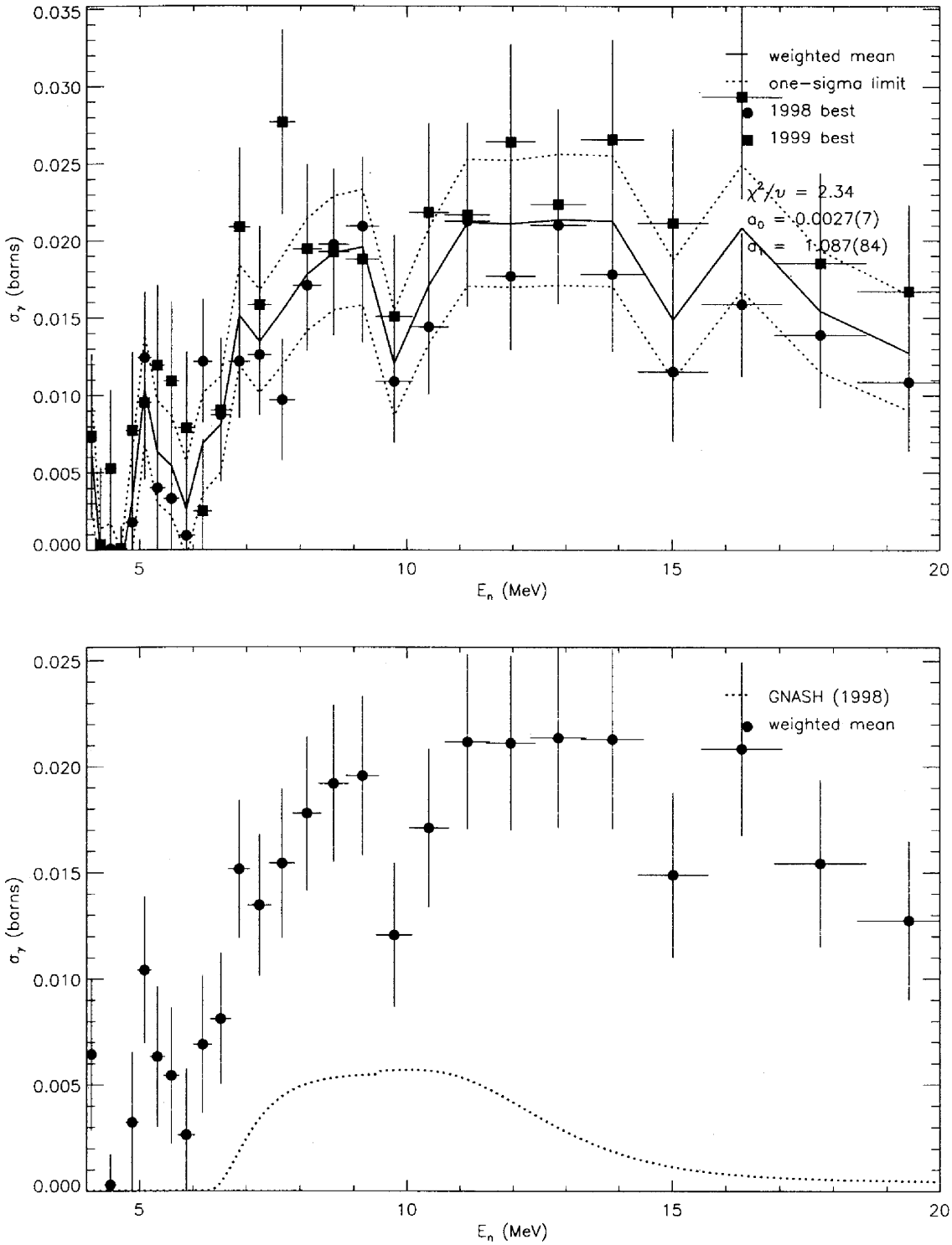

FIG. 69: Adopted E_γ = 883.4–keV partial cross section corresponding to the data in table LXXIX. The top panel shows the 1998 and 1999 partial cross sections (corrected for angular–distribution effects) and the recommended value, plotted as a solid line with a one-sigma confidence band (dotted lines). The bottom panel shows this recommended partial cross section (solid circles) compared to GNASH.

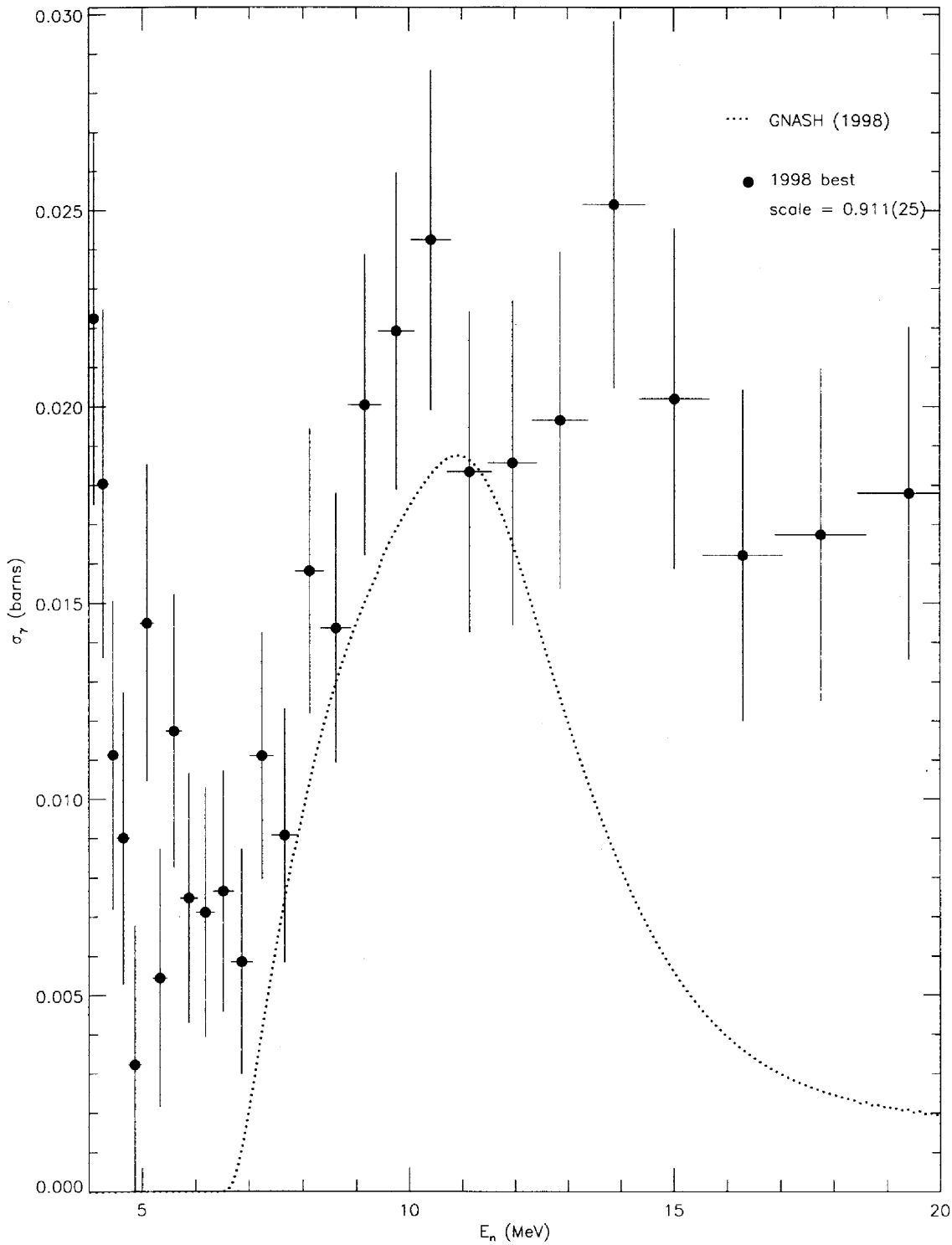

FIG. 70: Adopted E_γ = 898.3–keV partial cross section corresponding to the data in table LXXX, and corrected for angular–distribution effects. The target–thickness correction factor is shown, and the recommended partial cross section (solid circles) is compared to GNASH.

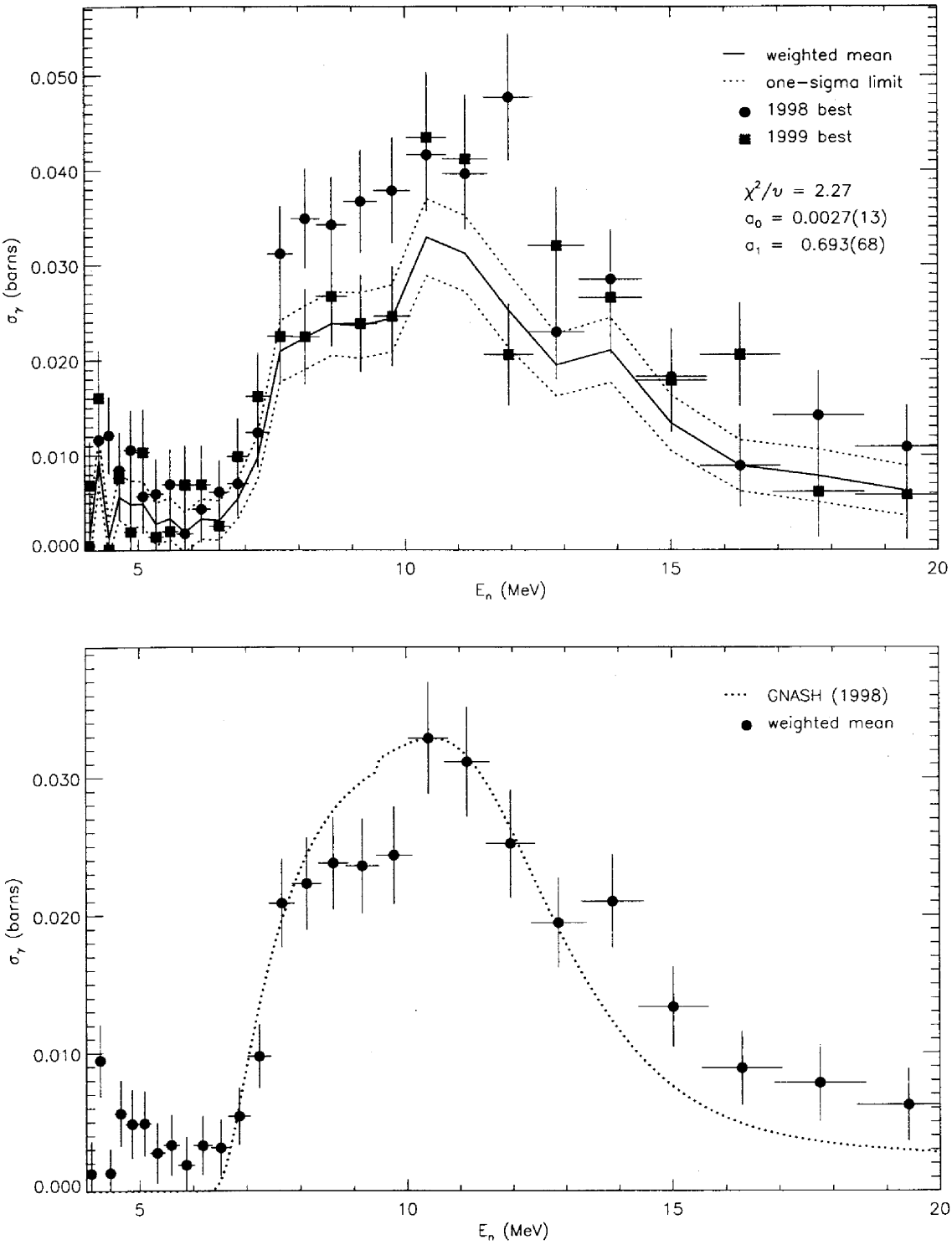

FIG. 71: Adopted E_γ = 925.3–keV partial cross section corresponding to the data in table LXXXI. The top panel shows the 1998 and 1999 partial cross sections (corrected for angular–distribution effects) and the recommended value, plotted as a solid line with a one-sigma confidence band (dotted lines). The bottom panel shows this recommended partial cross section (solid circles) compared to GNASH.

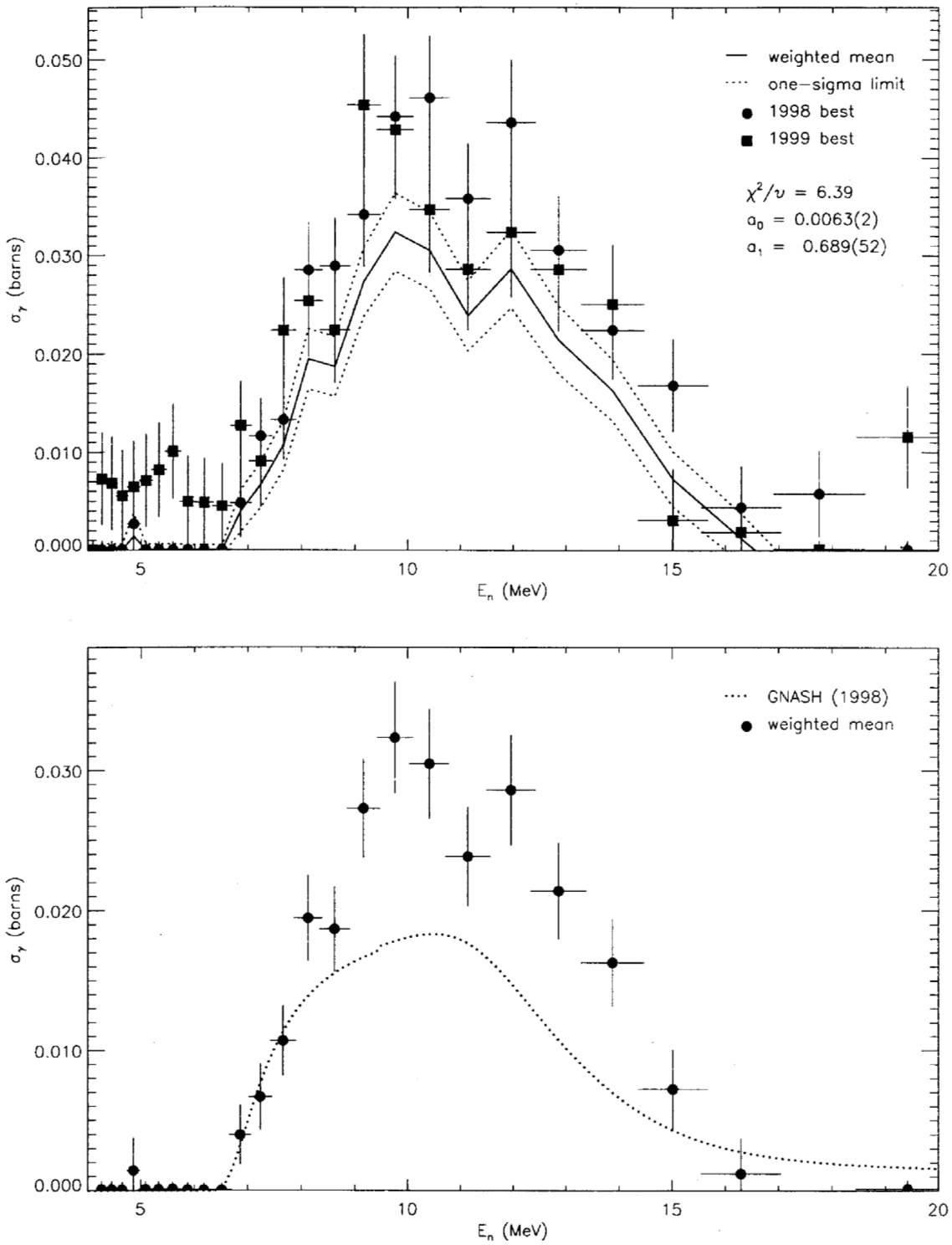

FIG. 72: Adopted E_γ = 946.1–keV partial cross section corresponding to the data in table LXXXII. The top panel shows the 1998 and 1999 partial cross sections (corrected for angular–distribution effects) and the recommended value, plotted as a solid line with a one-sigma confidence band (dotted lines). The bottom panel shows this recommended partial cross section (solid circles) compared to GNASH.

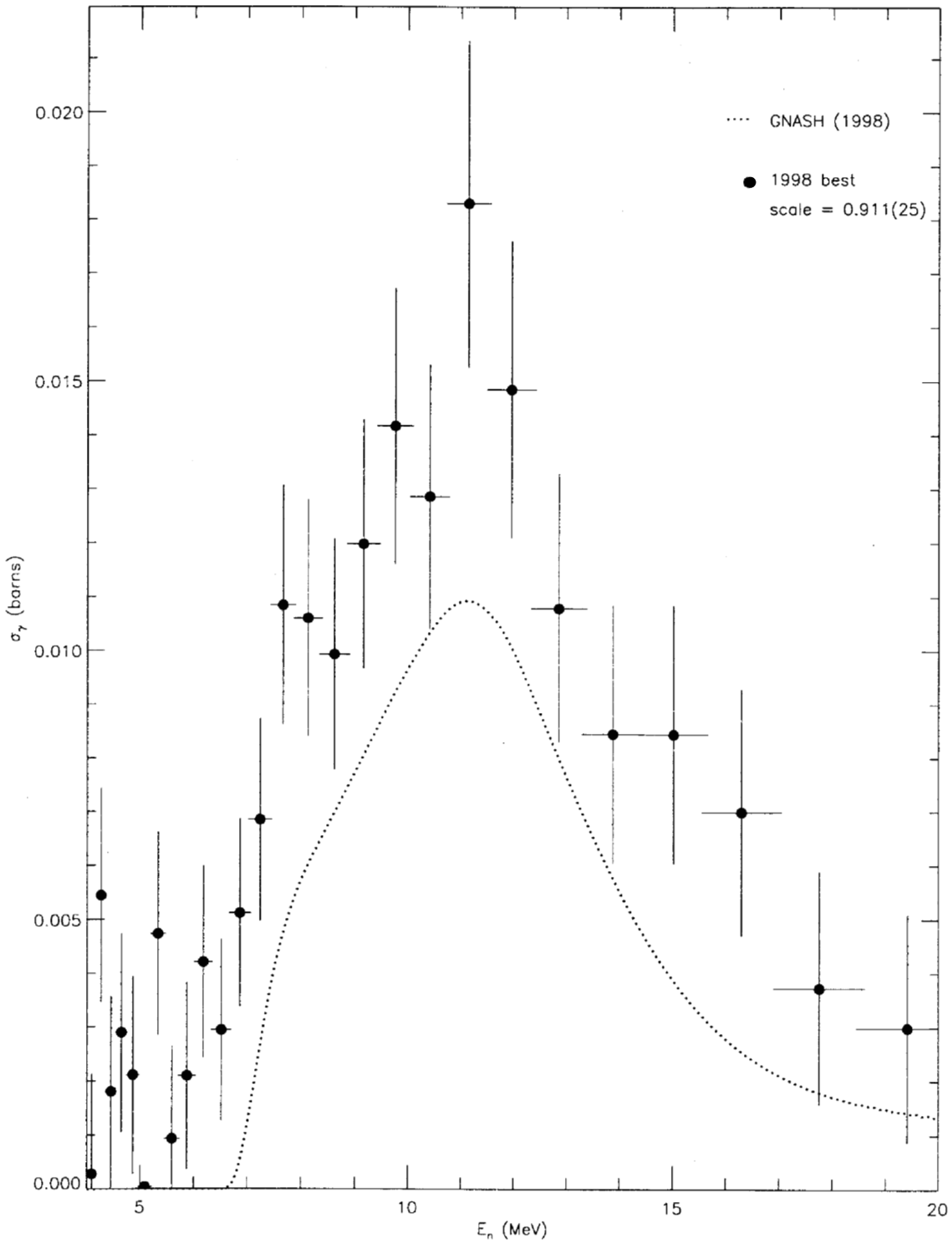

FIG. 73: Adopted E_γ = 966.3–keV partial cross section corresponding to the data in table LXXXIII, and corrected for angular–distribution effects. The target–thickness correction factor is shown, and the recommended partial cross section (solid circles) is compared to GNASH.

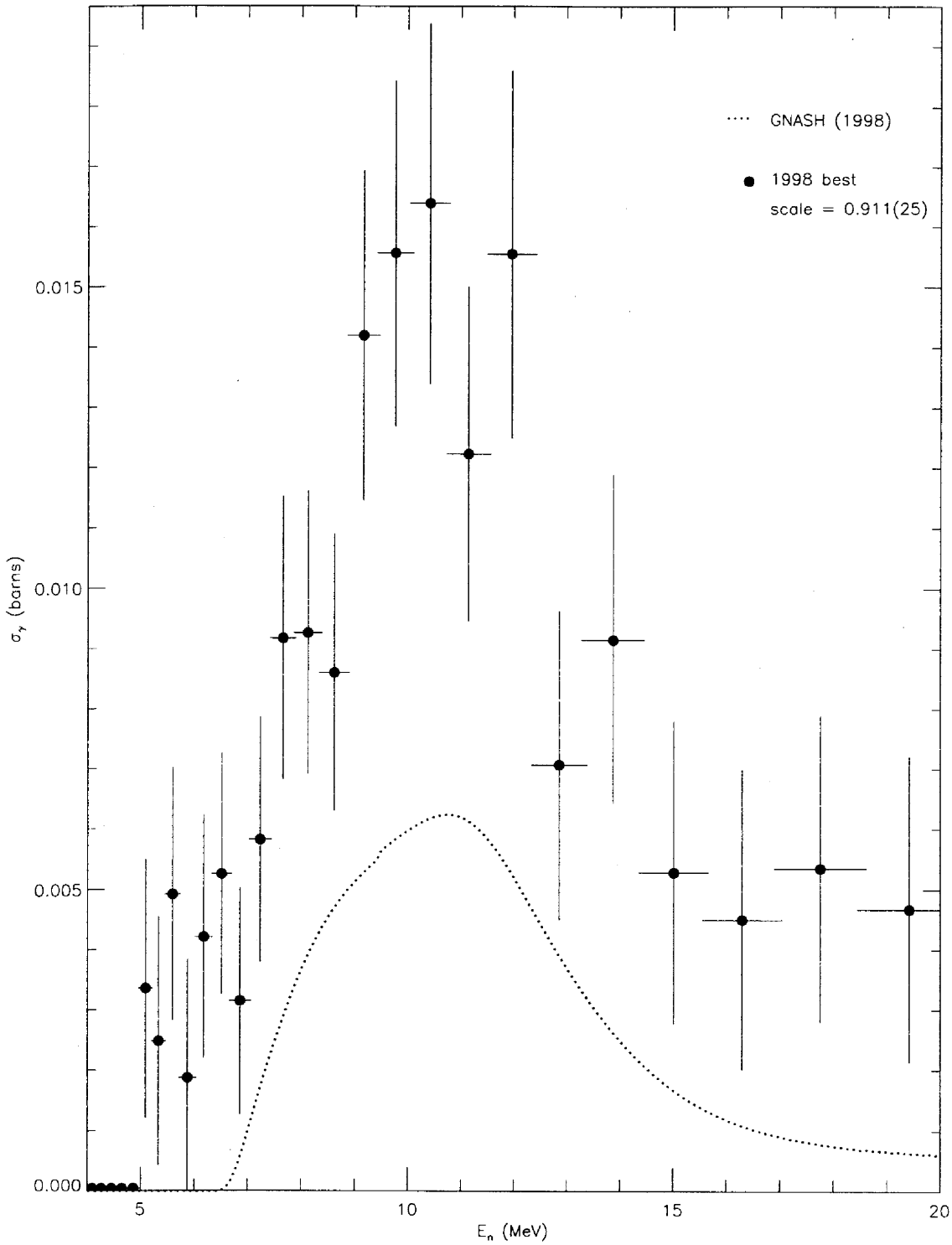

FIG. 75: Adopted E_γ = 984.8–keV partial cross section corresponding to the data in table LXXXV, and corrected for angular–distribution effects. The target–thickness correction factor is shown, and the recommended partial cross section (solid circles) is compared to GNASH.

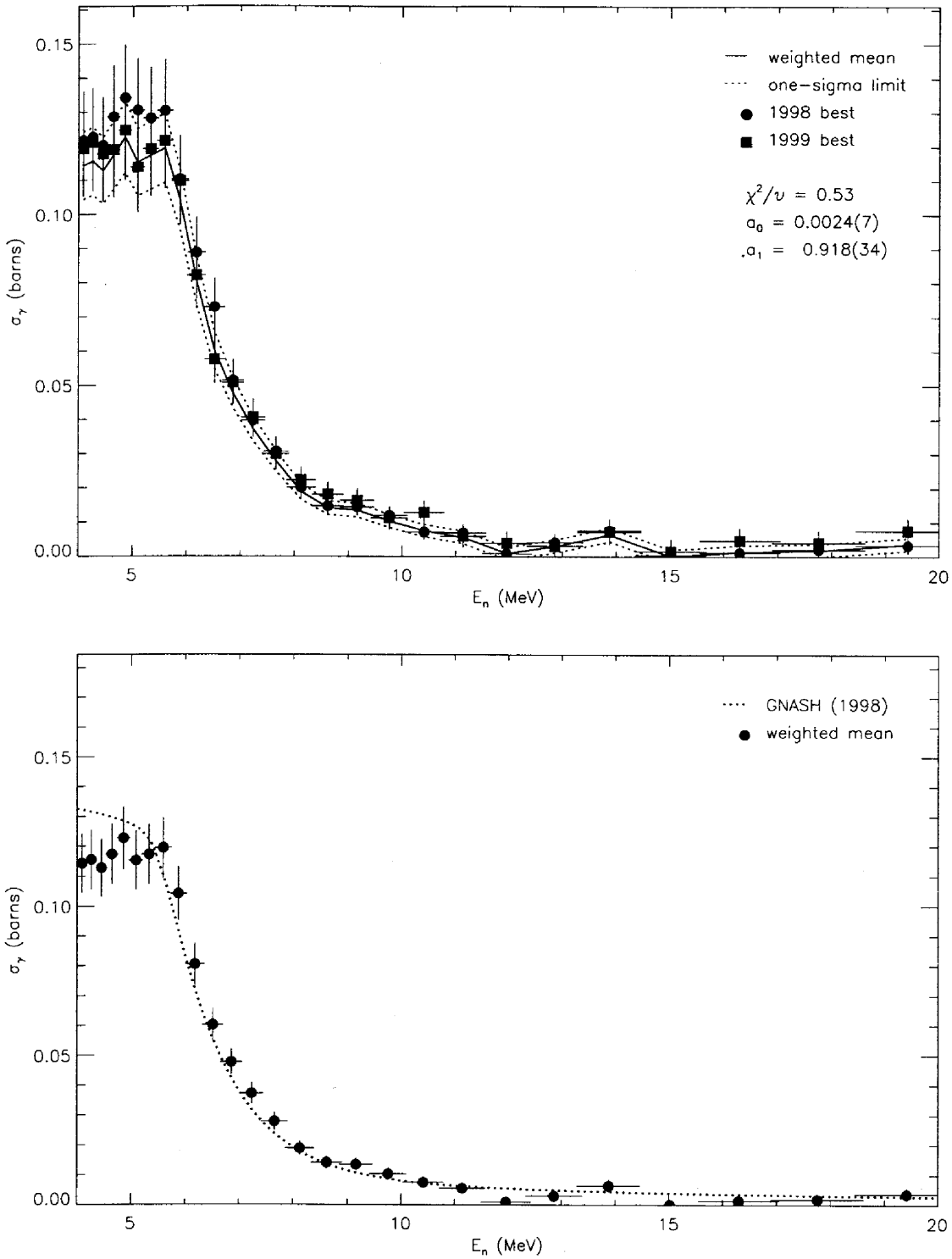

FIG. 80: Adopted E_γ = 129.3–keV partial cross section corresponding to the data in table LXXXVII. The top panel shows the 1998 and 1999 partial cross sections and the recommended value, plotted as a solid line with a one-sigma confidence band (dotted lines). The bottom panel shows this recommended partial cross section (solid circles) compared to GNASH.

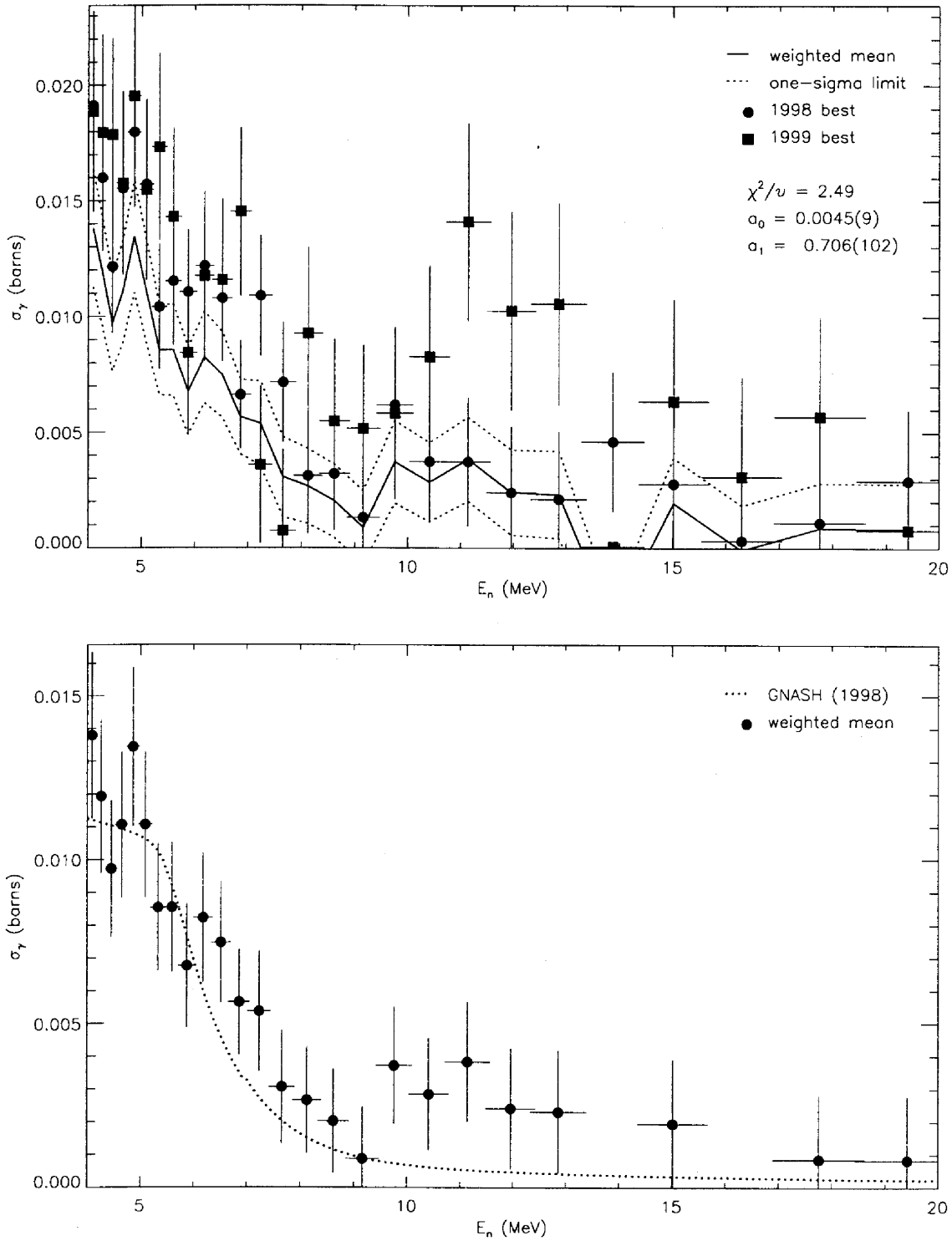

FIG. 81: Adopted E_γ = 316.5–keV partial cross section corresponding to the data in table LXXXVIII. The top panel shows the 1998 and 1999 partial cross sections and the recommended value, plotted as a solid line with a one-sigma confidence band (dotted lines). The bottom panel shows this recommended partial cross section (solid circles) compared to GNASH.

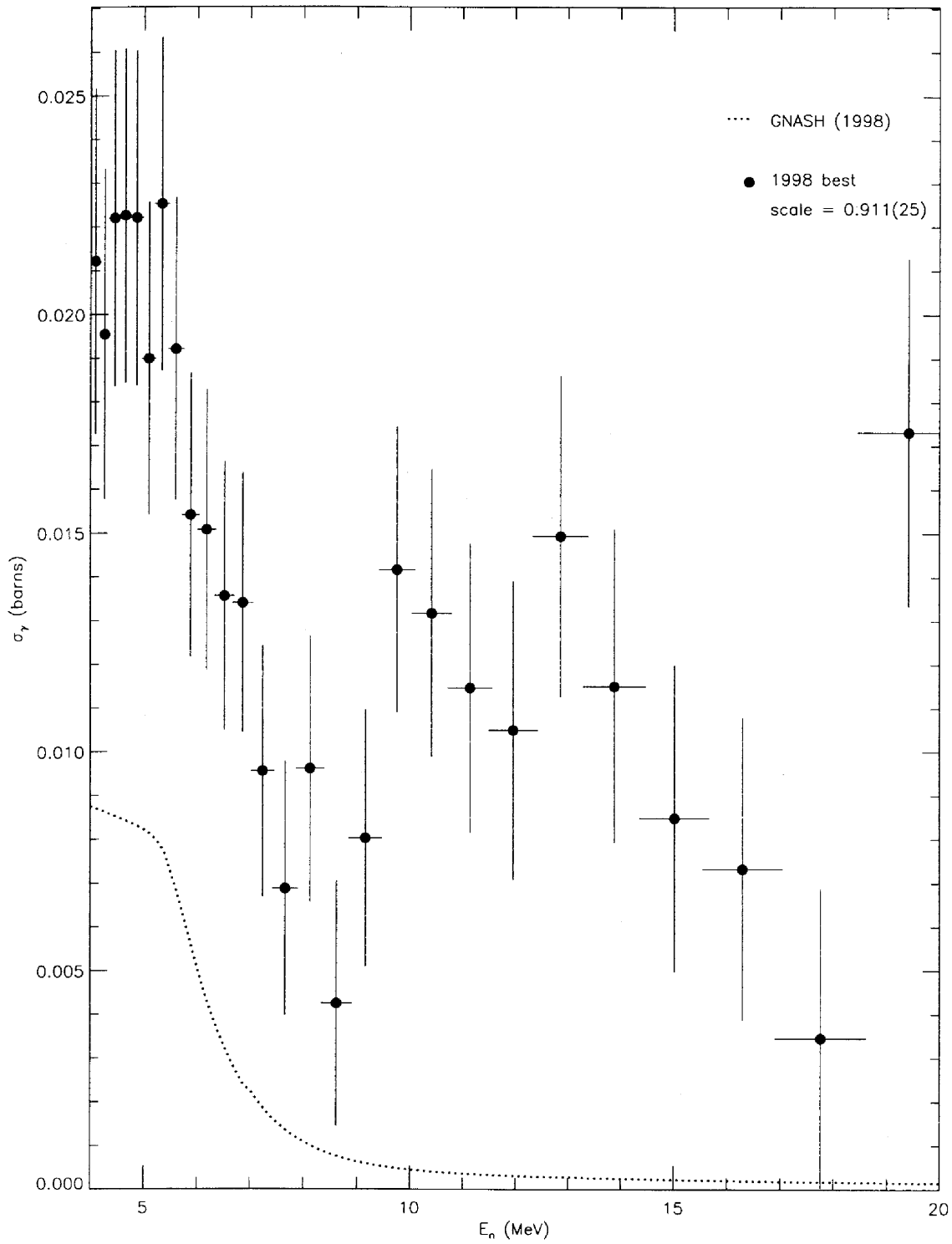

FIG. 82: Adopted E_γ = 375.1–keV partial cross section corresponding to the data in table LXXXIX. The target–thickness correction factor is shown, and the recommended partial cross section (solid circles) is compared to GNASH.

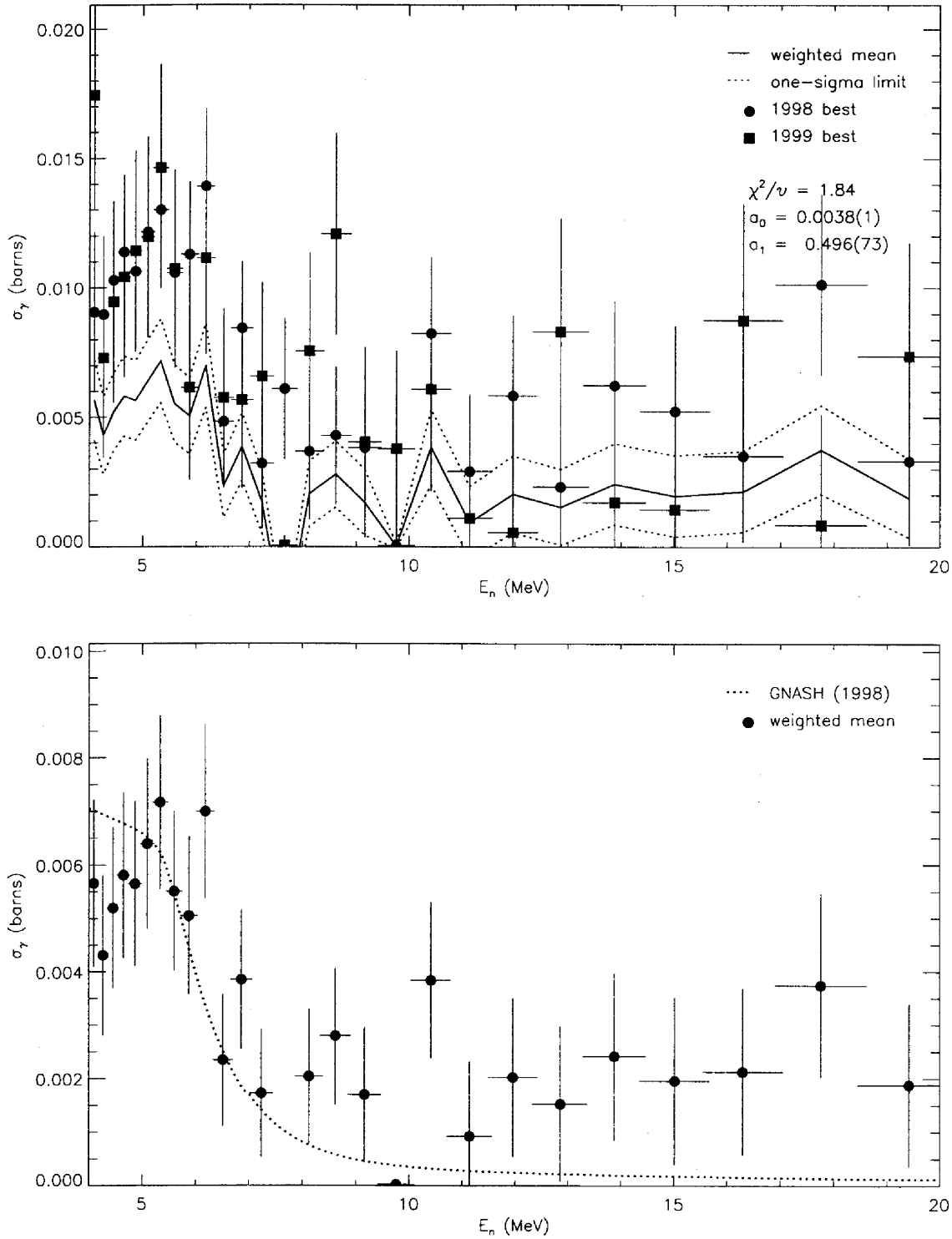

FIG. 83: Adopted $E_\gamma = 380.1$–keV partial cross section corresponding to the data in table XC. The top panel shows the 1998 and 1999 partial cross sections and the recommended value, plotted as a solid line with a one-sigma confidence band (dotted lines). The bottom panel shows this recommended partial cross section (solid circles) compared to GNASH.

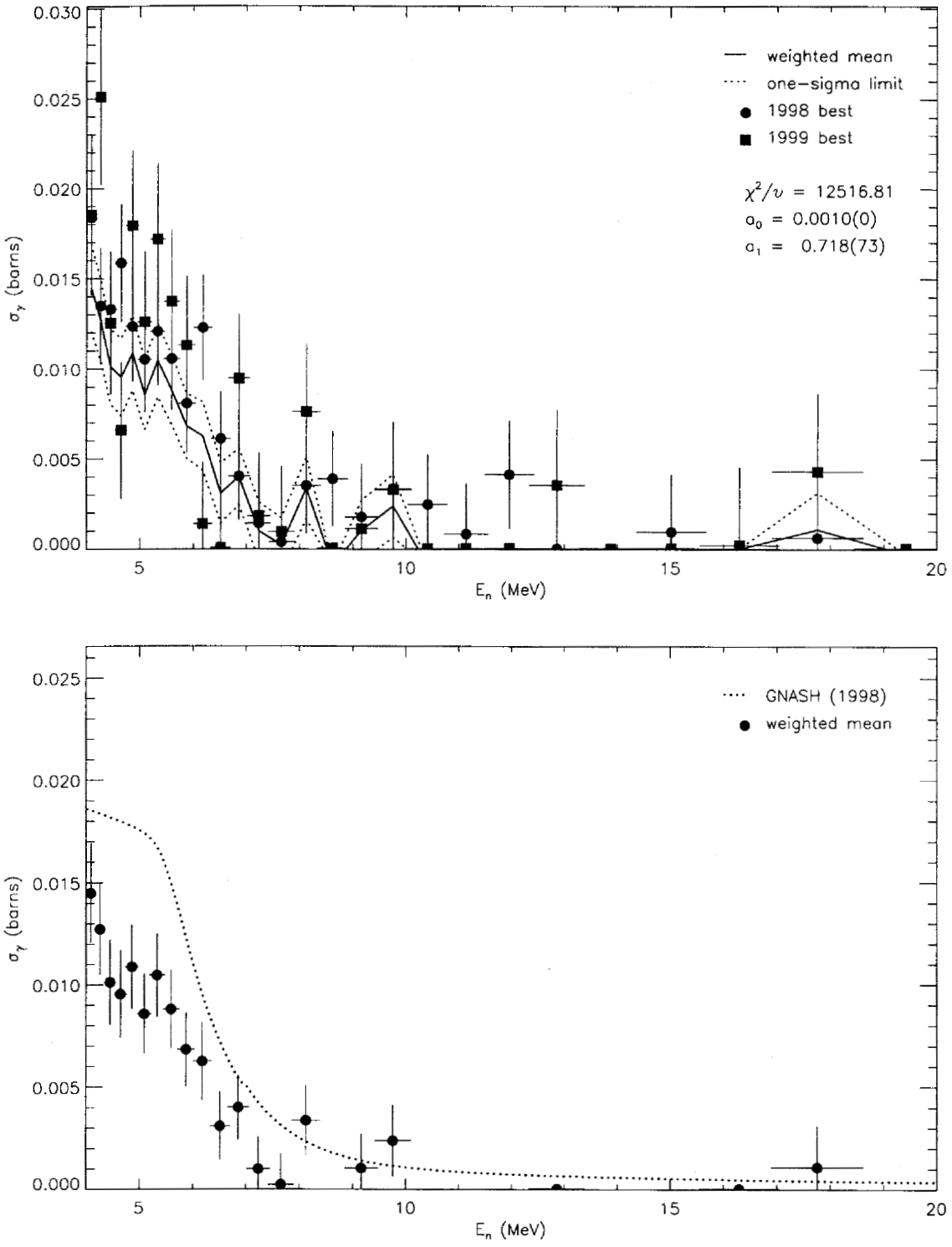

FIG. 84: Adopted E_γ = 392.5–keV partial cross section corresponding to the data in table XCI. The top panel shows the 1998 and 1999 partial cross sections and the recommended value, plotted as a solid line with a one-sigma confidence band (dotted lines). The bottom panel shows this recommended partial cross section (solid circles) compared to GNASH.

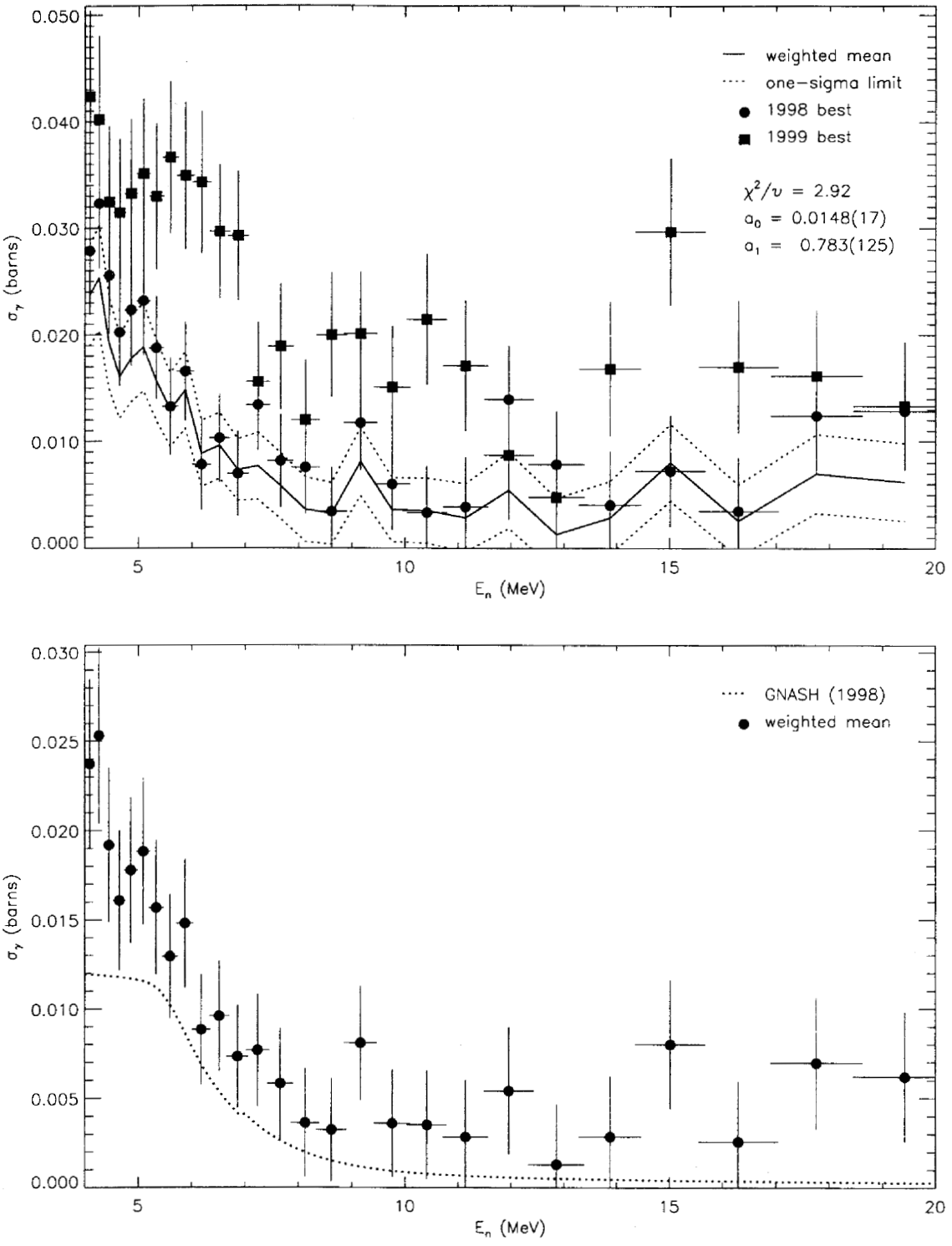

FIG. 86: Adopted E_γ = 617.6–keV partial cross section corresponding to the data in table XCIII. The top panel shows the 1998 and 1999 partial cross sections and the recommended value, plotted as a solid line with a one-sigma confidence band (dotted lines). The bottom panel shows this recommended partial cross section (solid circles) compared to GNASH.

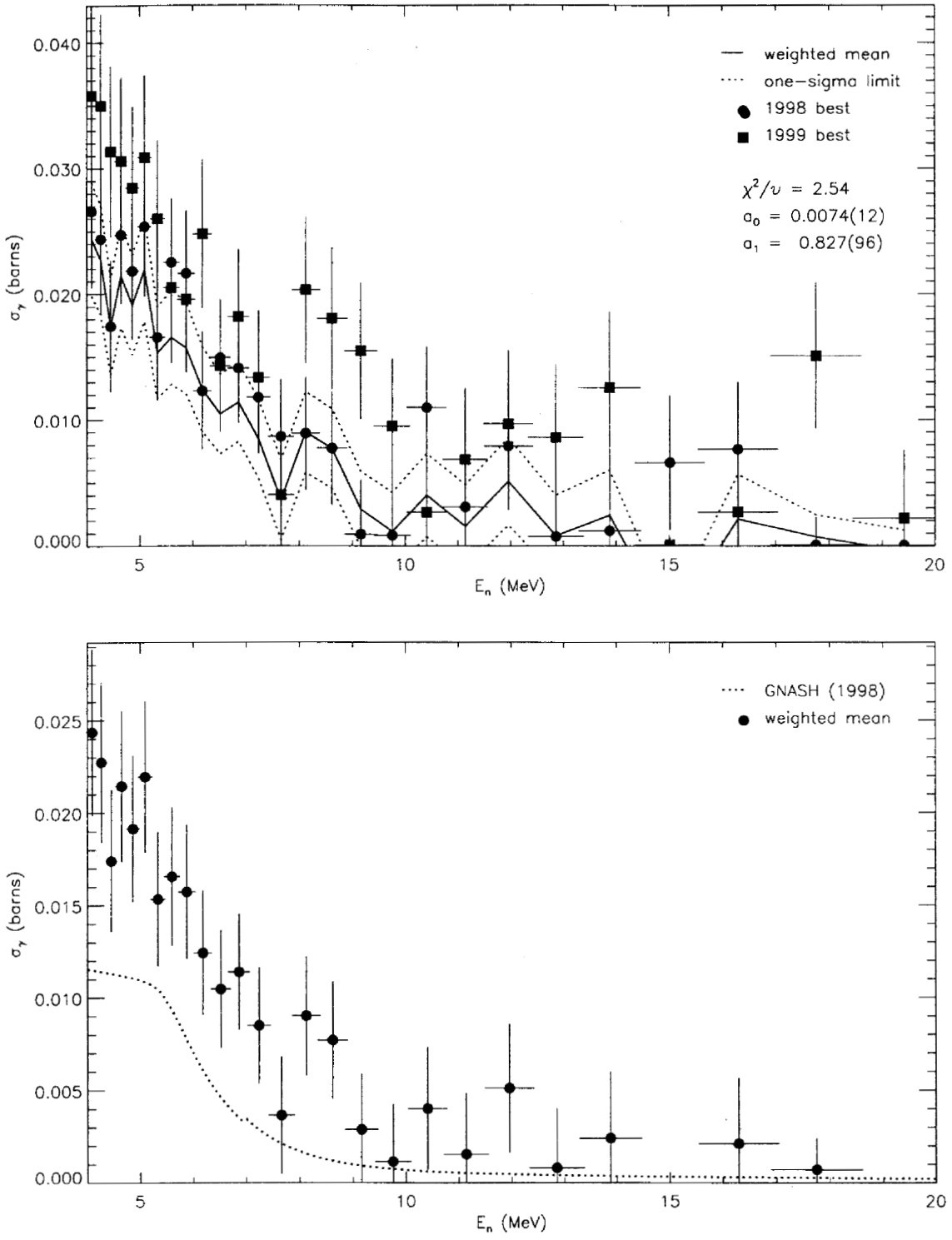

FIG. 87: Adopted E_γ = 624.9–keV partial cross section corresponding to the data in table XCIV. The top panel shows the 1998 and 1999 partial cross sections and the recommended value, plotted as a solid line with a one-sigma confidence band (dotted lines). The bottom panel shows this recommended partial cross section (solid circles) compared to GNASH.

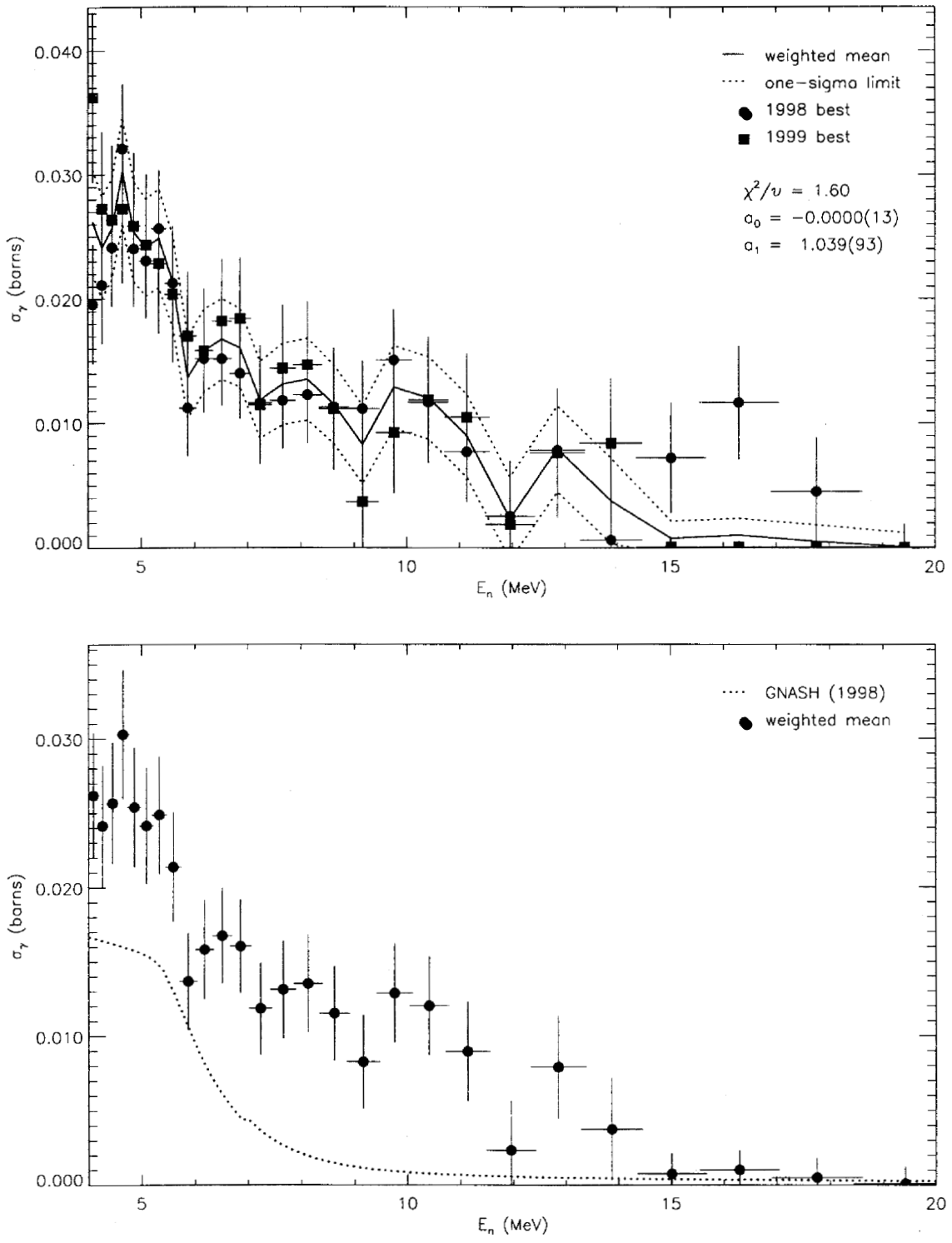

FIG. 88: Adopted E_γ = 633.1–keV partial cross section corresponding to the data in table XCV. The top panel shows the 1998 and 1999 partial cross sections and the recommended value, plotted as a solid line with a one-sigma confidence band (dotted lines). The bottom panel shows this recommended partial cross section (solid circles) compared to GNASH.

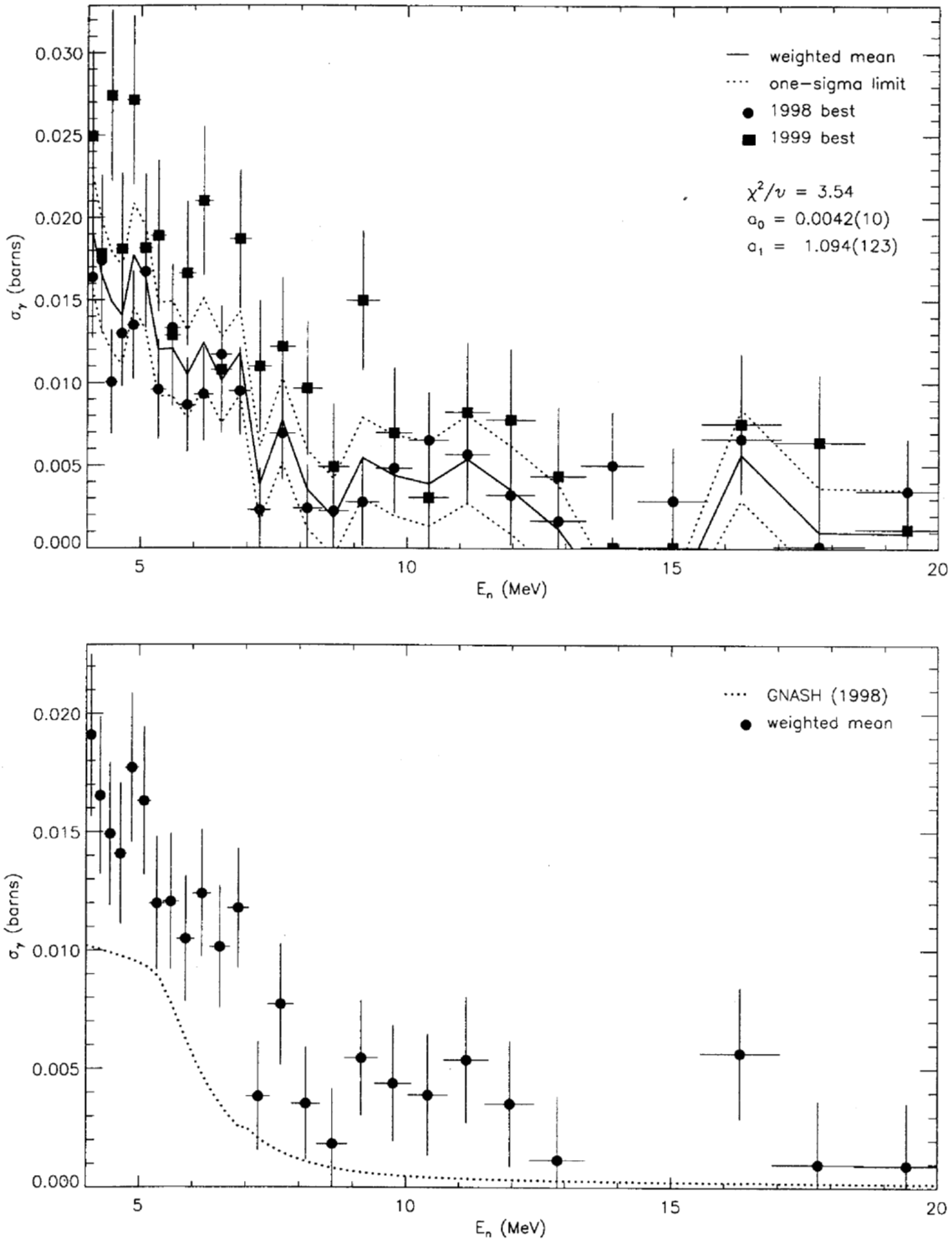

FIG. 89: Adopted E_γ = 637.7-keV partial cross section corresponding to the data in table XCVI. The top panel shows the 1998 and 1999 partial cross sections and the recommended value, plotted as a solid line with a one-sigma confidence band (dotted lines). The bottom panel shows this recommended partial cross section (solid circles) compared to GNASH.

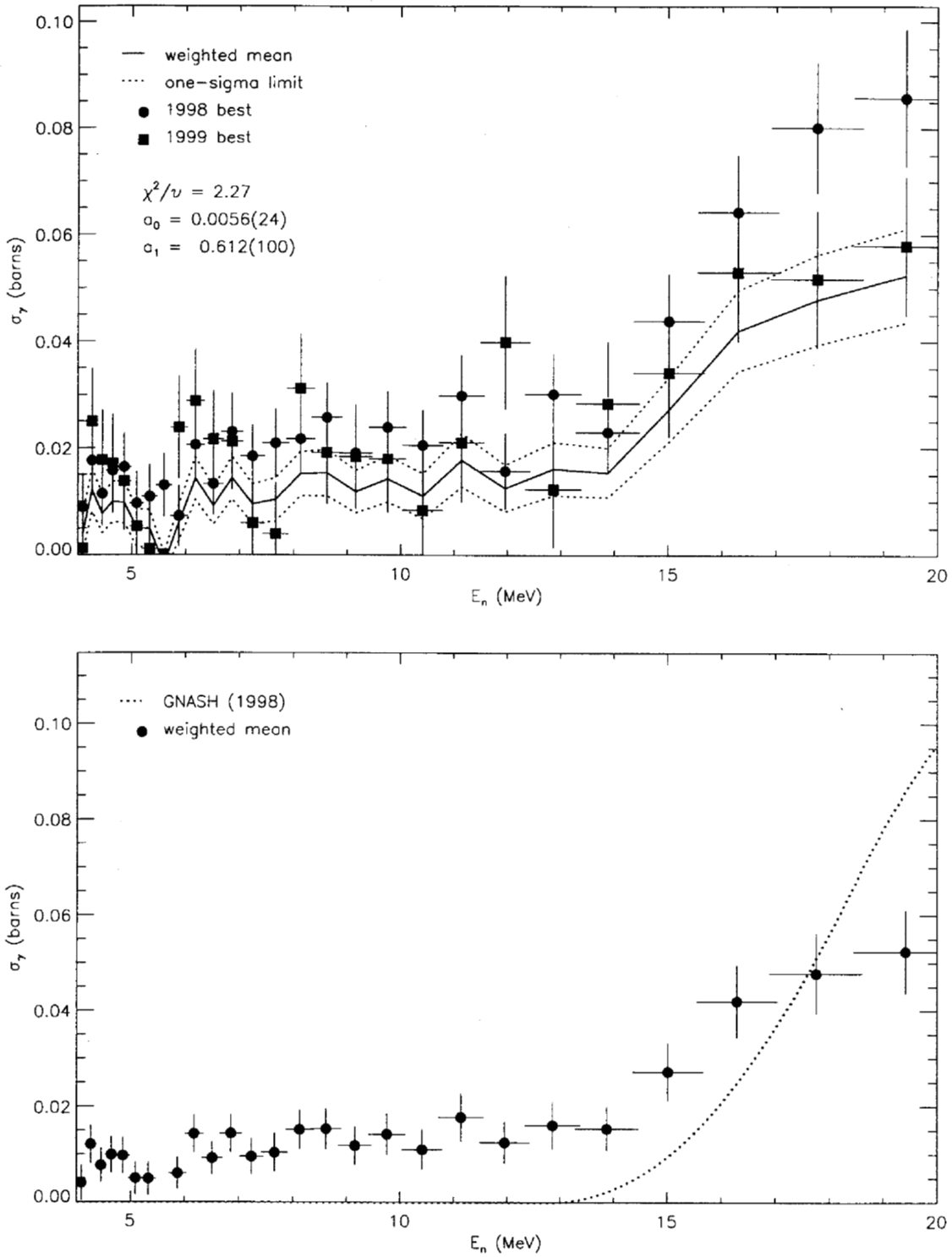

FIG. 92: Adopted E_γ = 137.6–keV partial cross section corresponding to the data in table XCIX. The top panel shows the 1998 and 1999 partial cross sections (corrected for angular–distribution effects) and the recommended value, plotted as a solid line with a one-sigma confidence band (dotted lines). The bottom panel shows this recommended partial cross section (solid circles) compared to GNASH.

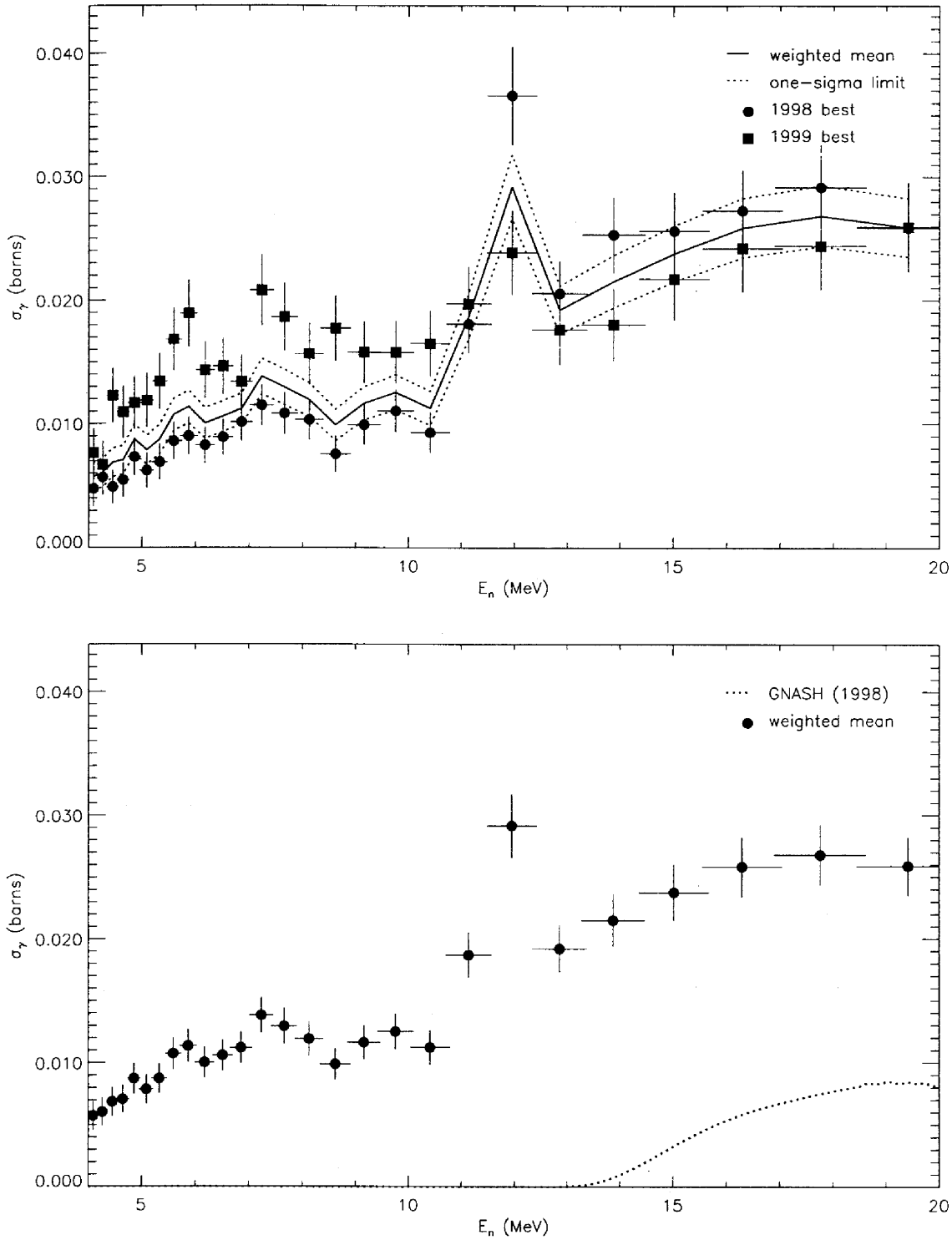

FIG. 94: Adopted $E_\gamma = 298.5$–keV partial cross section corresponding to the data in table CI. The top panel shows the 1998 and 1999 partial cross sections (corrected for angular–distribution effects) and the recommended value, plotted as a solid line with a one-sigma confidence band (dotted lines). The bottom panel shows this recommended partial cross section (solid circles) compared to GNASH.

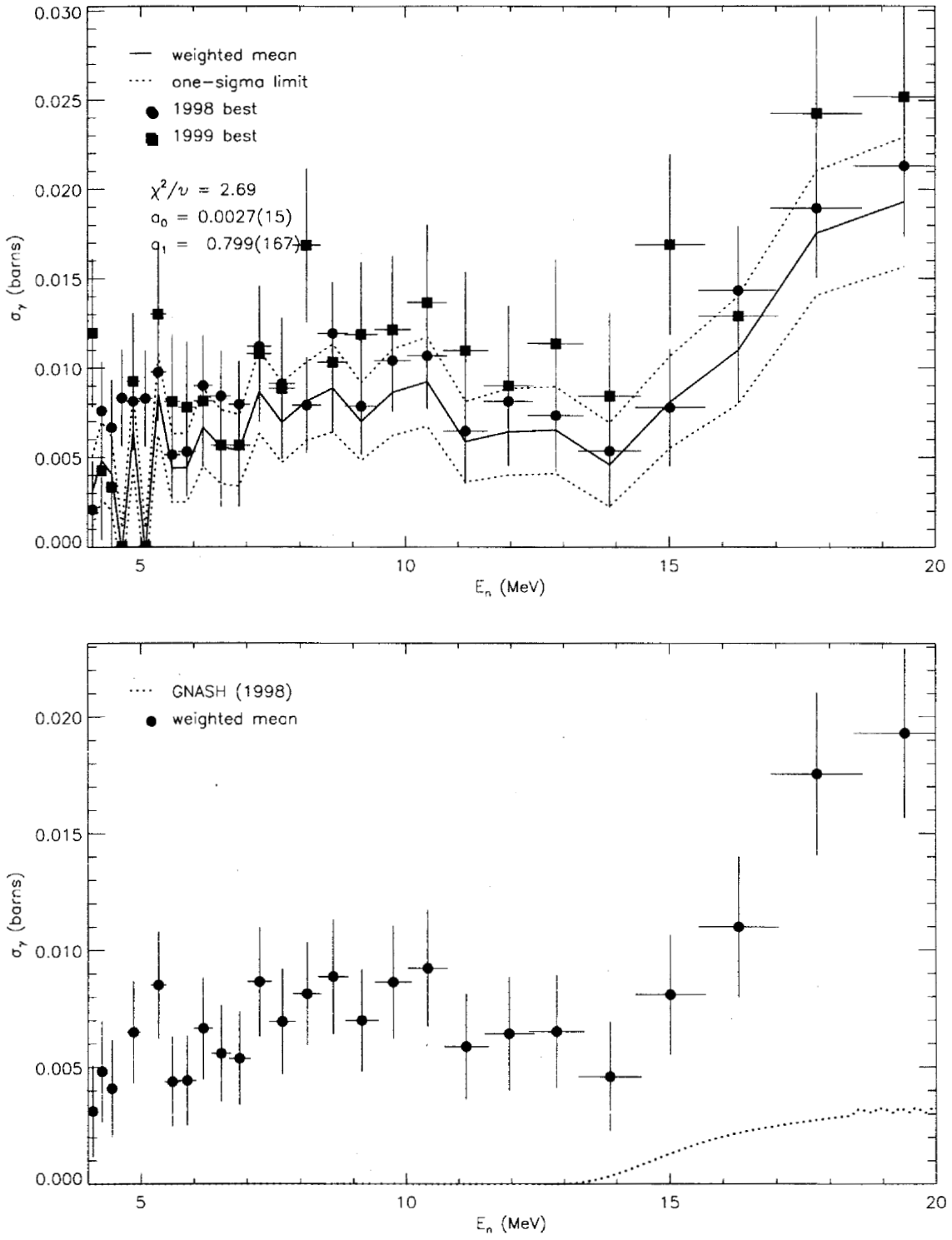

FIG. 95: Adopted E_γ = 300.5–keV partial cross section corresponding to the data in table CII. The top panel shows the 1998 and 1999 partial cross sections (corrected for angular–distribution effects) and the recommended value, plotted as a solid line with a one-sigma confidence band (dotted lines). The bottom panel shows this recommended partial cross section (solid circles) compared to GNASH.

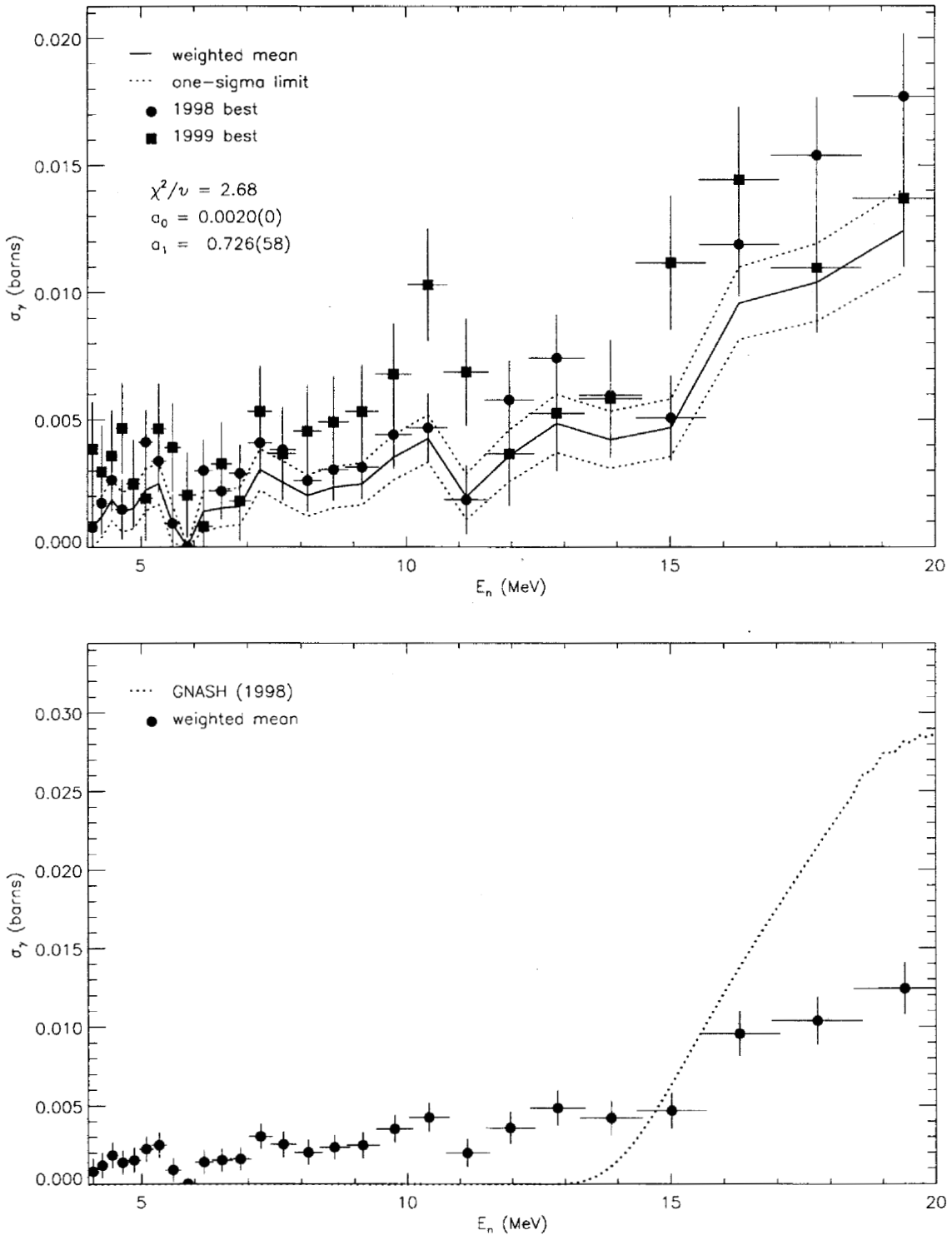

FIG. 96: Adopted E_γ = 305.2–keV partial cross section corresponding to the data in table CIII. The top panel shows the 1998 and 1999 partial cross sections (corrected for angular–distribution effects) and the recommended value, plotted as a solid line with a one-sigma confidence band (dotted lines). The bottom panel shows this recommended partial cross section (solid circles) compared to GNASH.

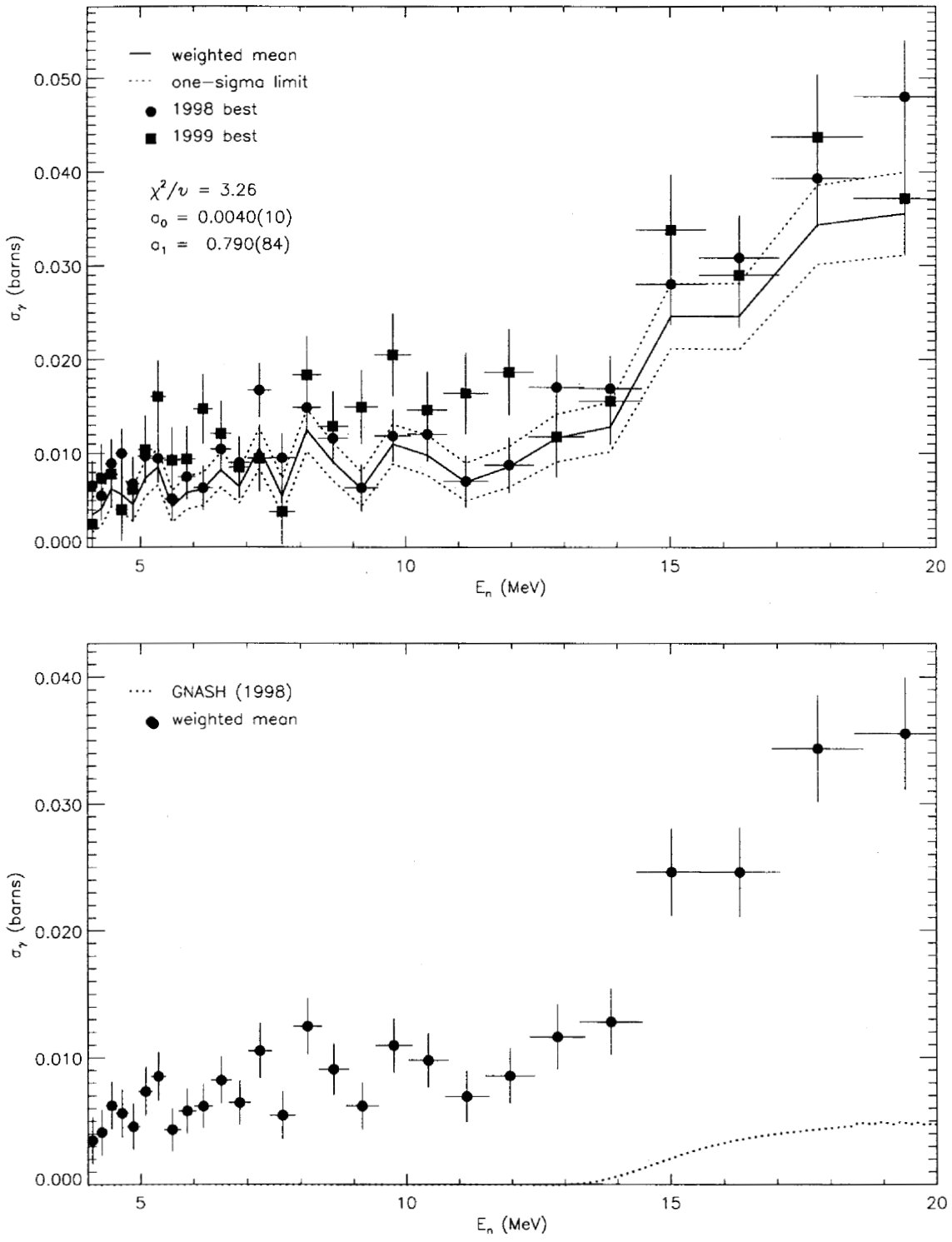

FIG. 97: Adopted E_γ = 312.0-keV partial cross section corresponding to the data in table CIV. The top panel shows the 1998 and 1999 partial cross sections (corrected for angular–distribution effects) and the recommended value, plotted as a solid line with a one-sigma confidence band (dotted lines). The bottom panel shows this recommended partial cross section (solid circles) compared to GNASH.

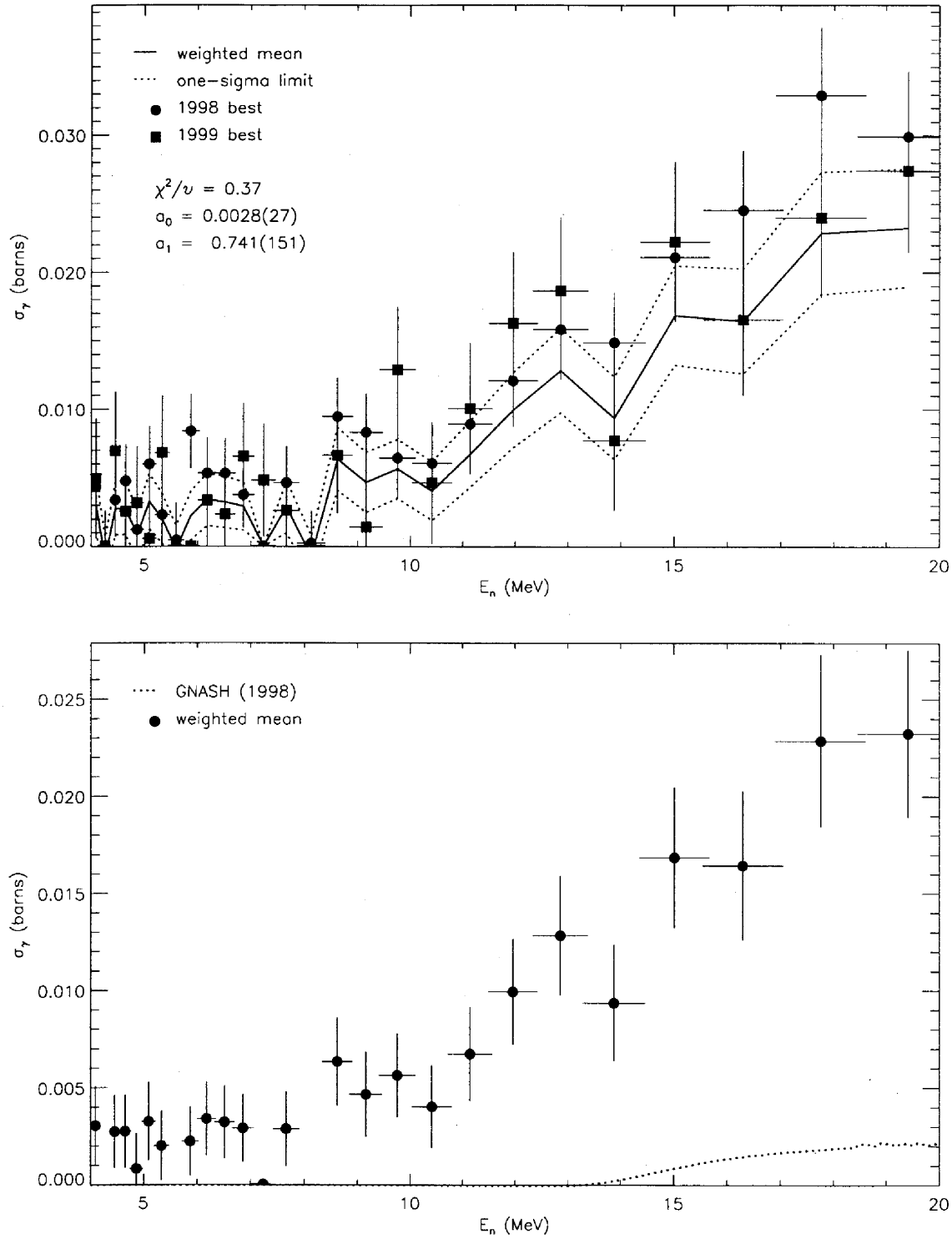

FIG. 98: Adopted E_γ = 340.6–keV partial cross section corresponding to the data in table CV. The top panel shows the 1998 and 1999 partial cross sections (corrected for angular–distribution effects) and the recommended value, plotted as a solid line with a one-sigma confidence band (dotted lines). The bottom panel shows this recommended partial cross section (solid circles) compared to GNASH.

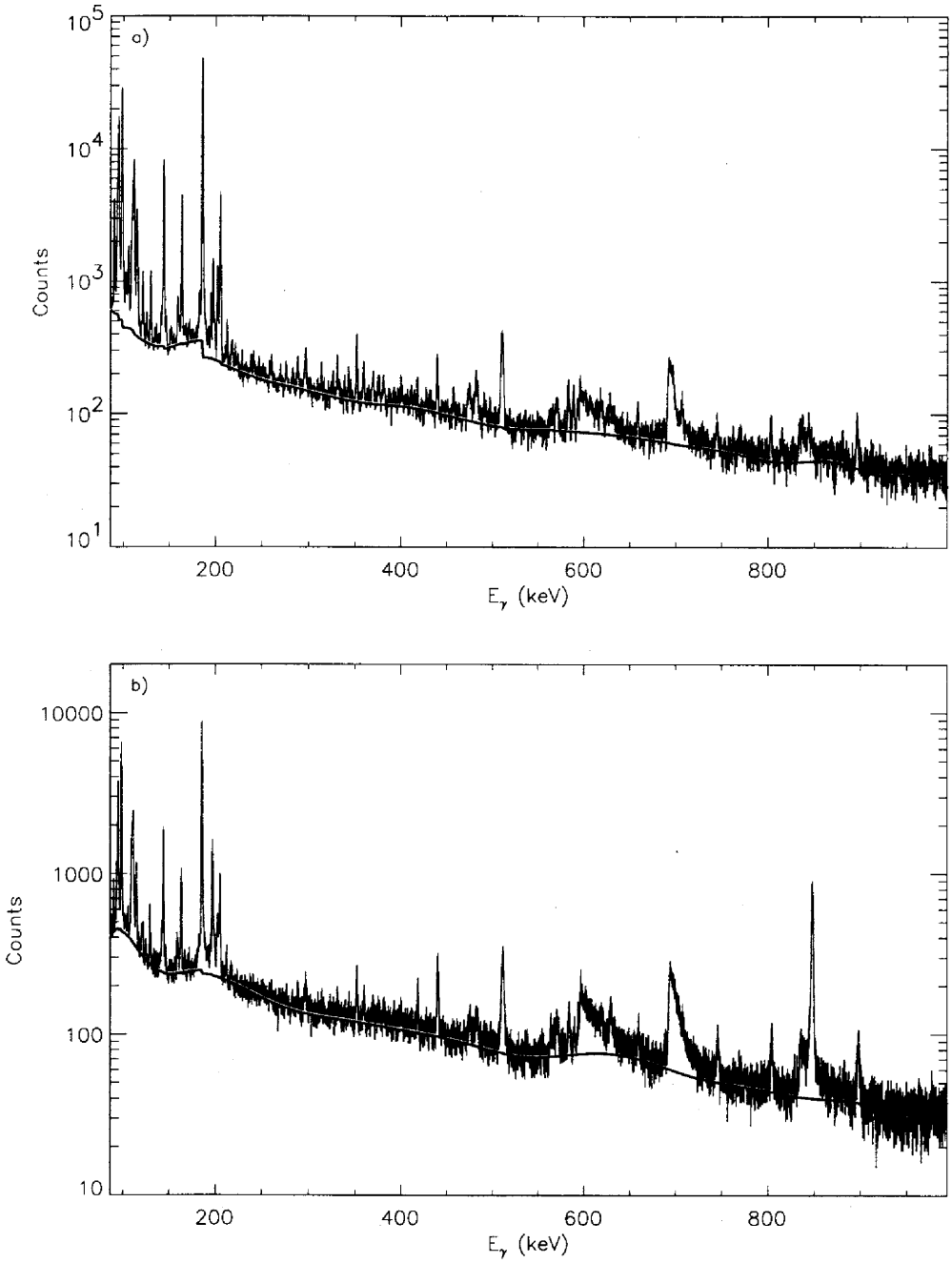

FIG. 99: Background used in the XGAM fit of bin 7 ($\overline{E}_n$ = 5.3 MeV) for the a) **98Thin** and b) **99Thin** γ–ray spectra.

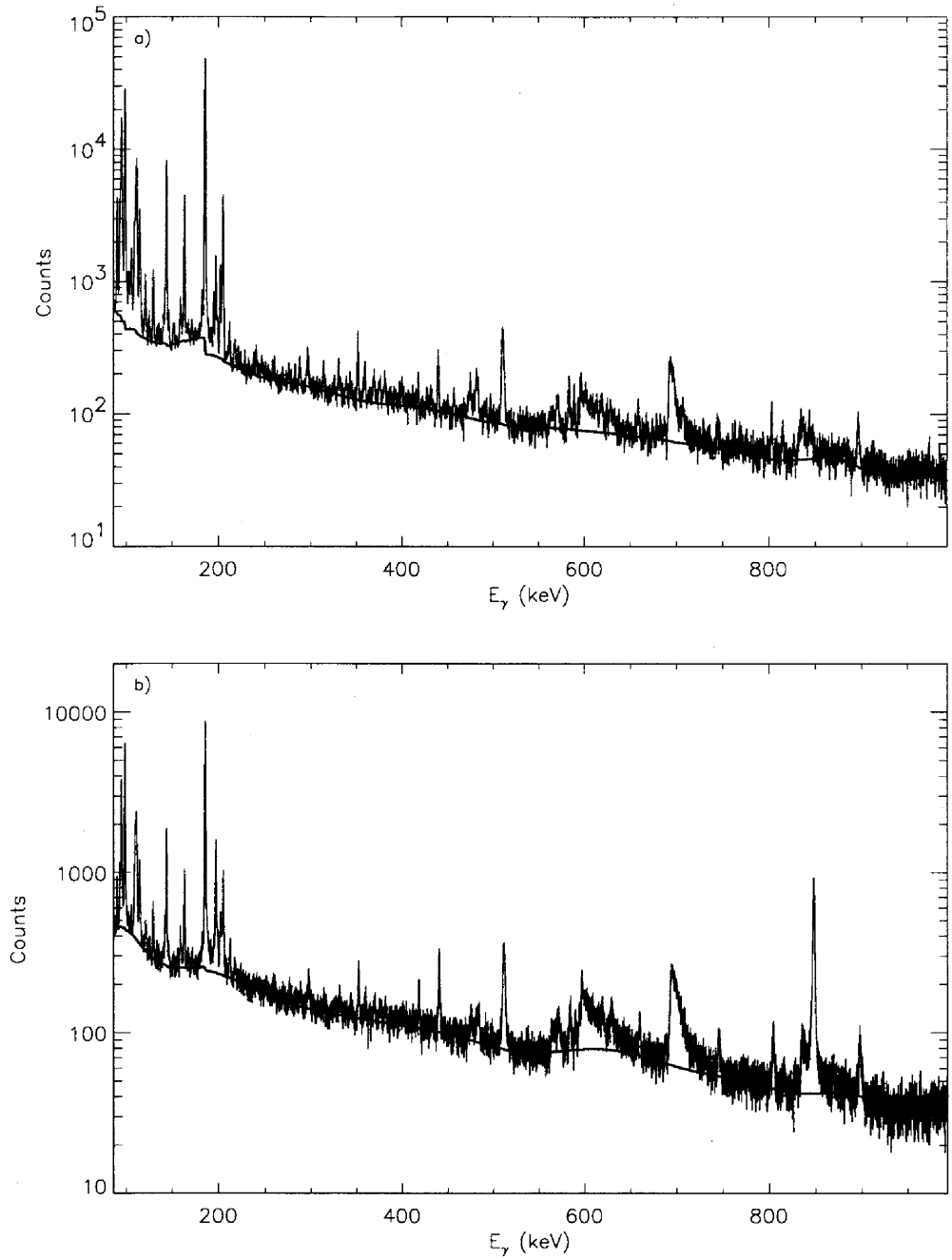

FIG. 100: Background used in the XGAM fit of bin 8 ($\overline{E}_n$ = 5.6 MeV) for the a) **98Thin** and b) **99Thin** γ–ray spectra.

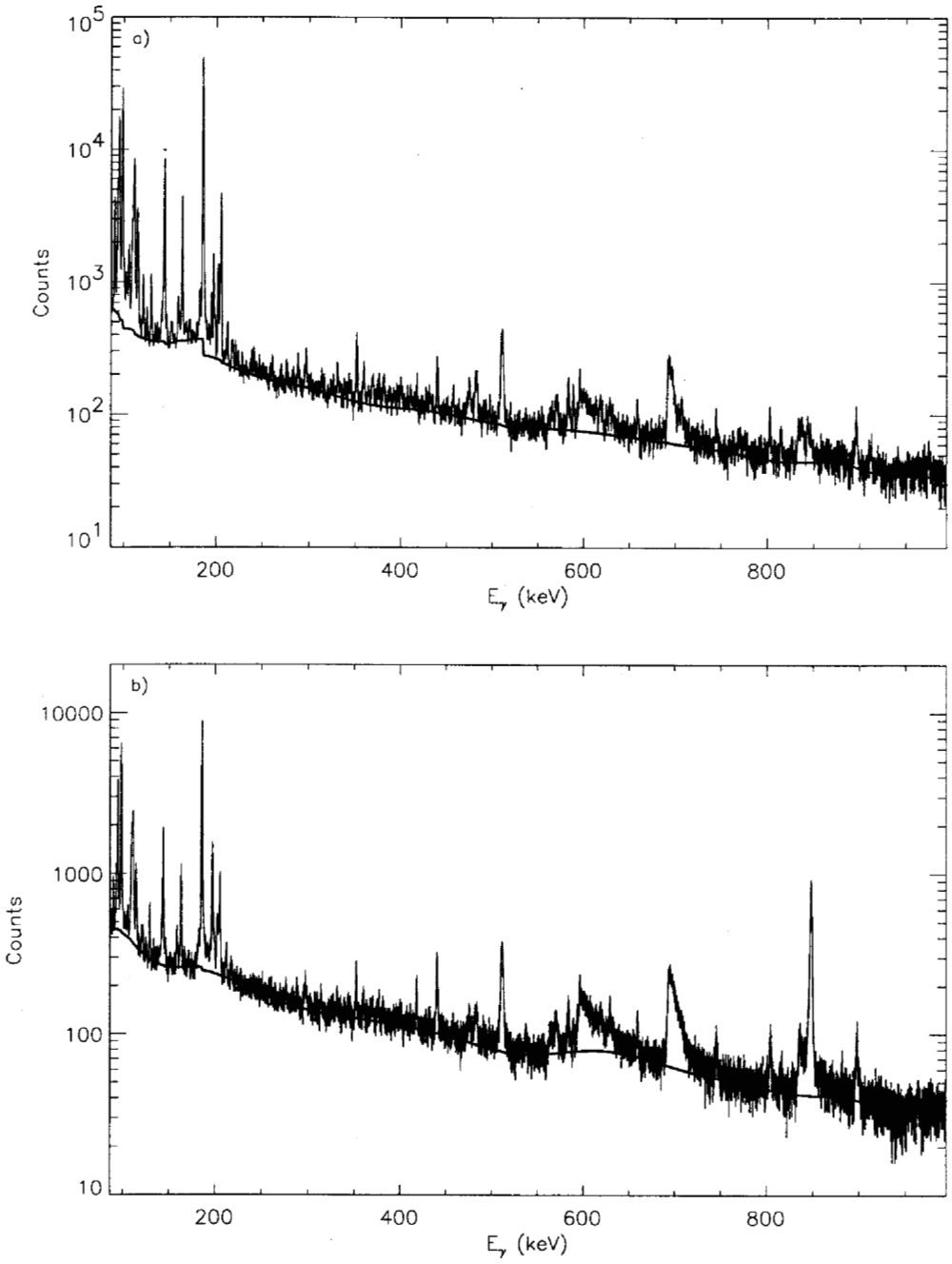

FIG. 101: Background used in the XGAM fit of bin 9 ($\overline{E}_n$ = 5.9 MeV) for the a) **98Thin** and b) **99Thin** γ–ray spectra.

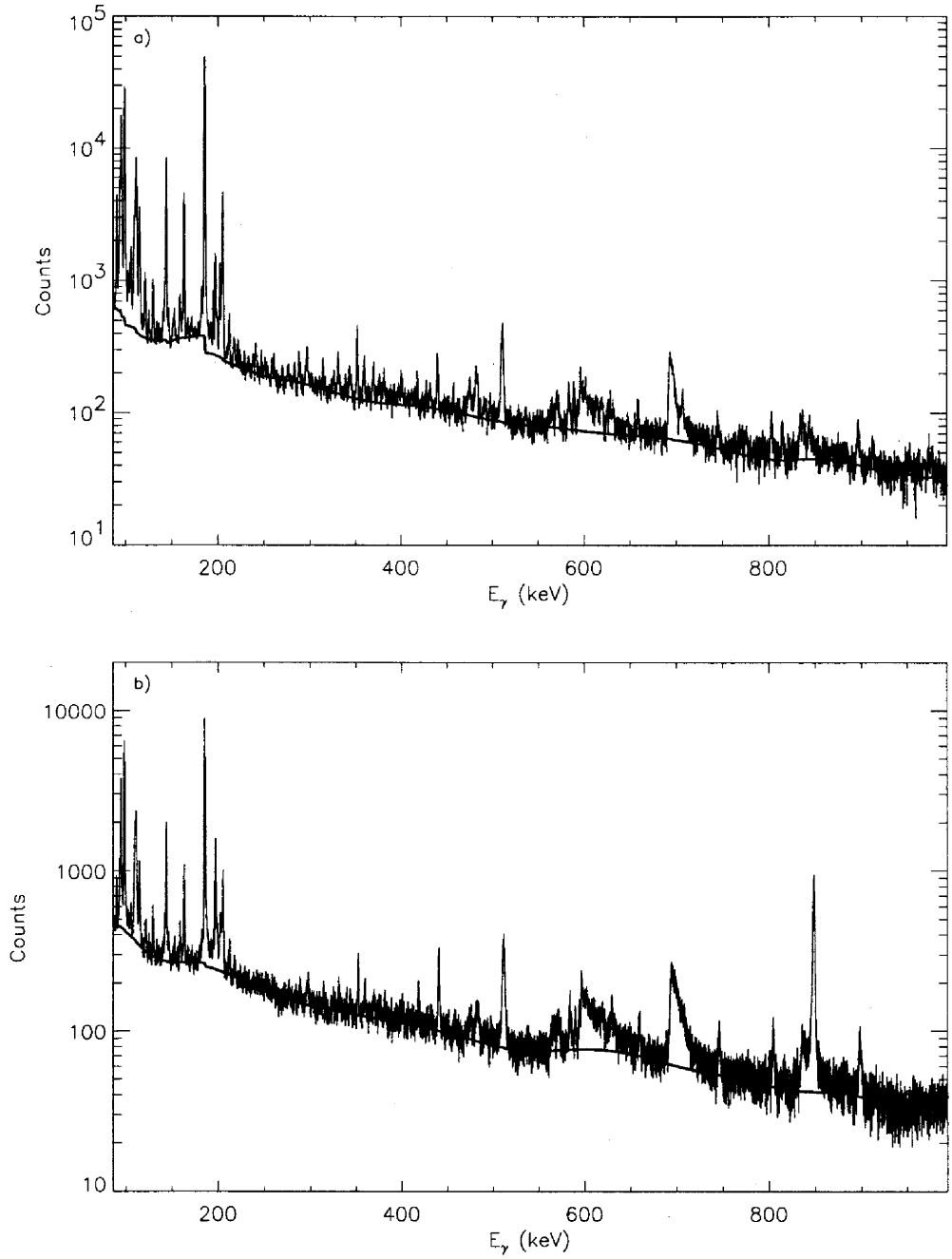

FIG. 102: Background used in the XGAM fit of bin 10 ($\overline{E}_n$ = 6.2 MeV) for the a) **98Thin** and b) **99Thin** γ–ray spectra.

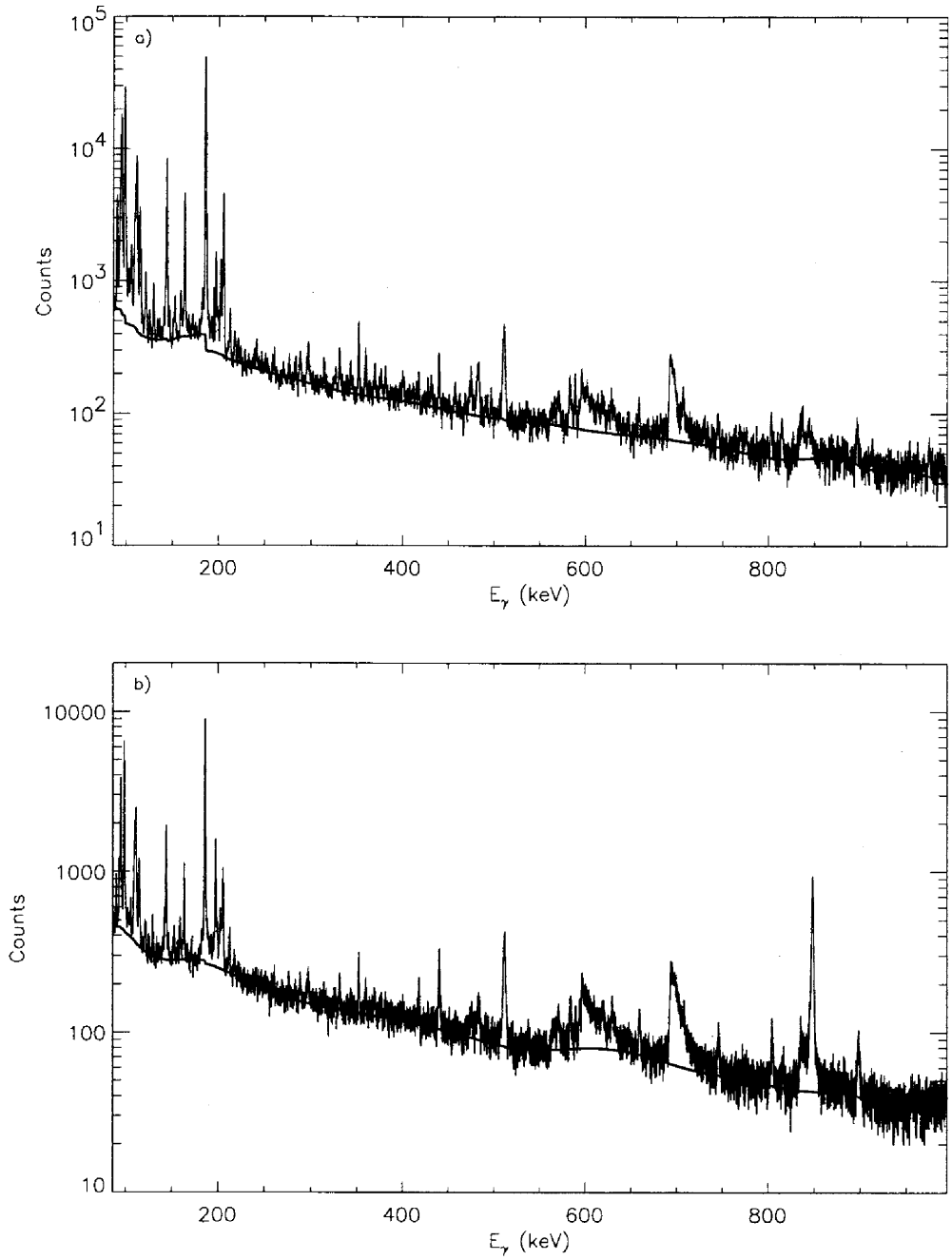

FIG. 103: Background used in the XGAM fit of bin 11 ($\overline{E}_n$ = 6.5 MeV) for the a) **98Thin** and b) **99Thin** γ–ray spectra.

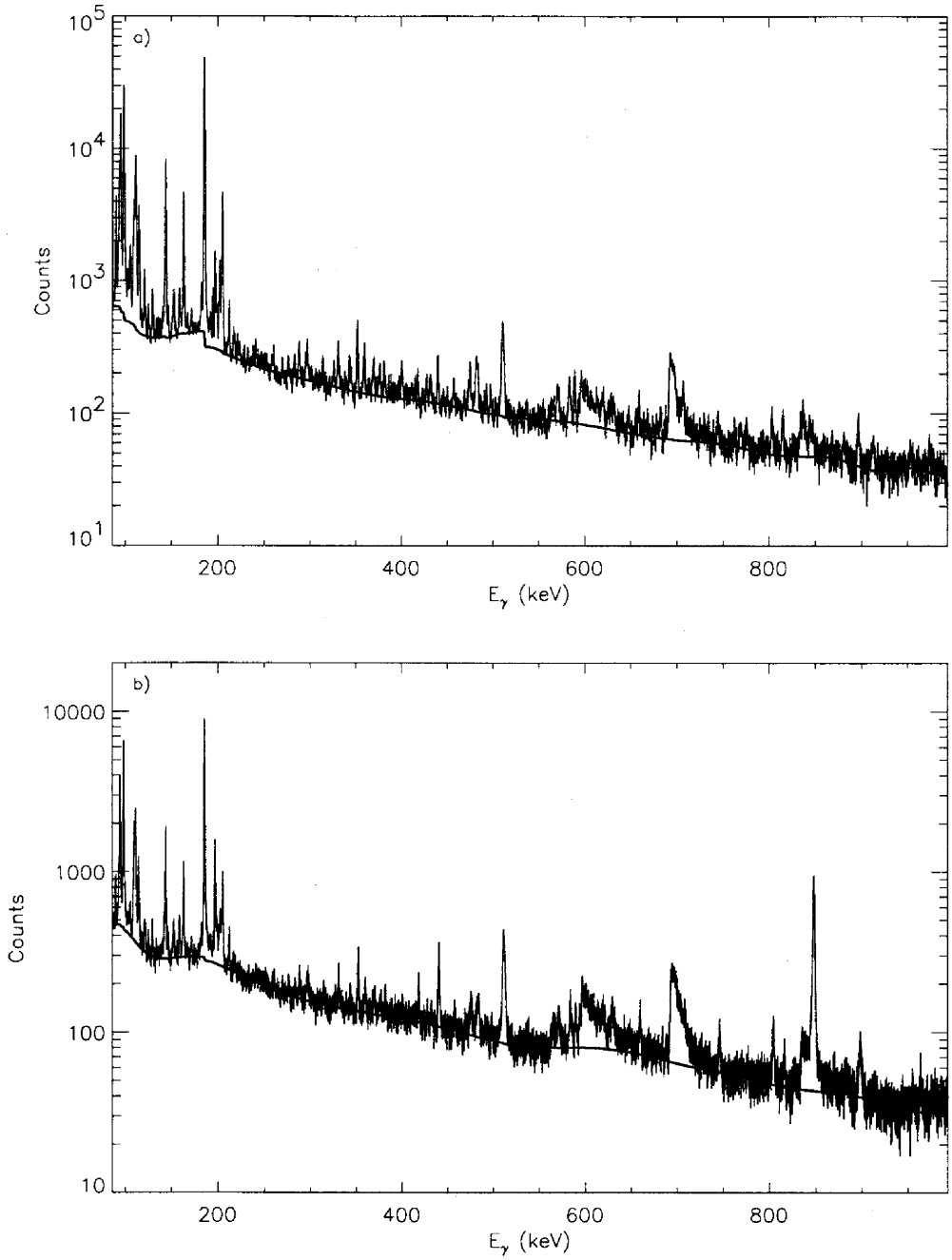

FIG. 104: Background used in the XGAM fit of bin 12 ($\overline{E}_n$ = 6.9 MeV) for the a) **98Thin** and b) **99Thin** γ–ray spectra.

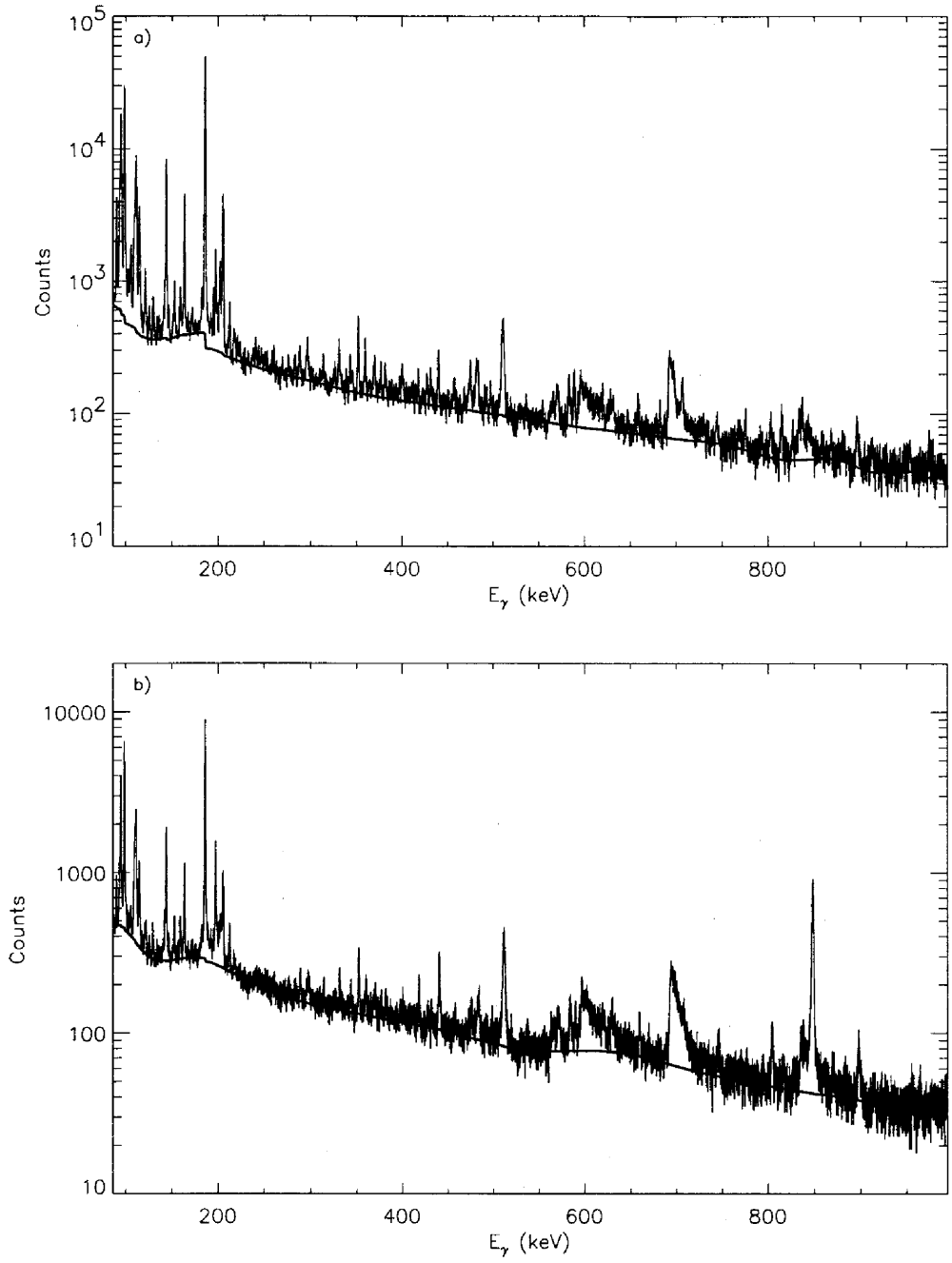

FIG. 105: Background used in the XGAM fit of bin 13 ($\overline{E}_n$ = 7.2 MeV) for the a) **98Thin** and b) **99Thin** γ–ray spectra.

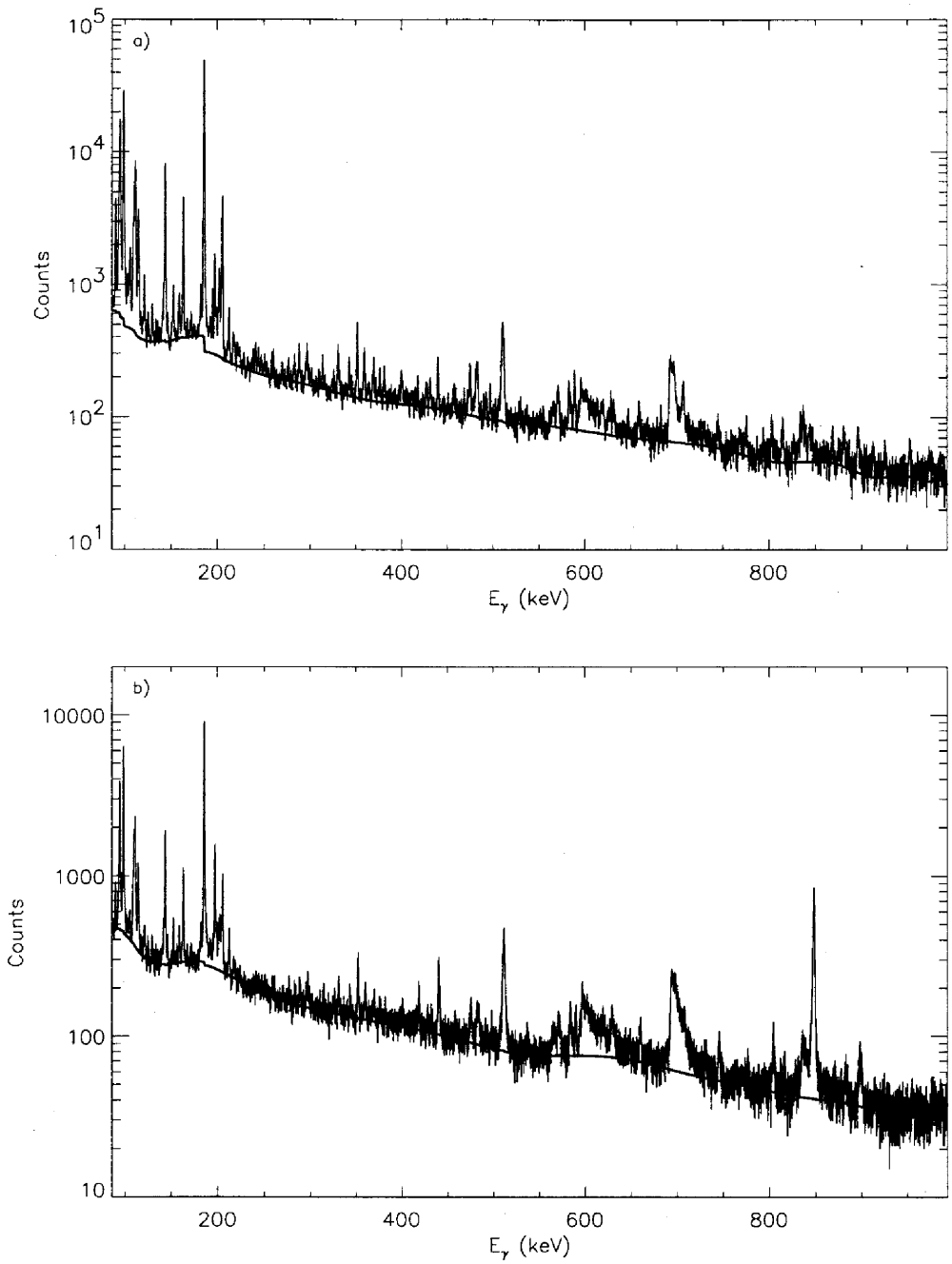

FIG. 106: Background used in the XGAM fit of bin 14 ($\overline{E}_n$ = 7.6 MeV) for the a) **98Thin** and b) **99Thin** γ–ray spectra.

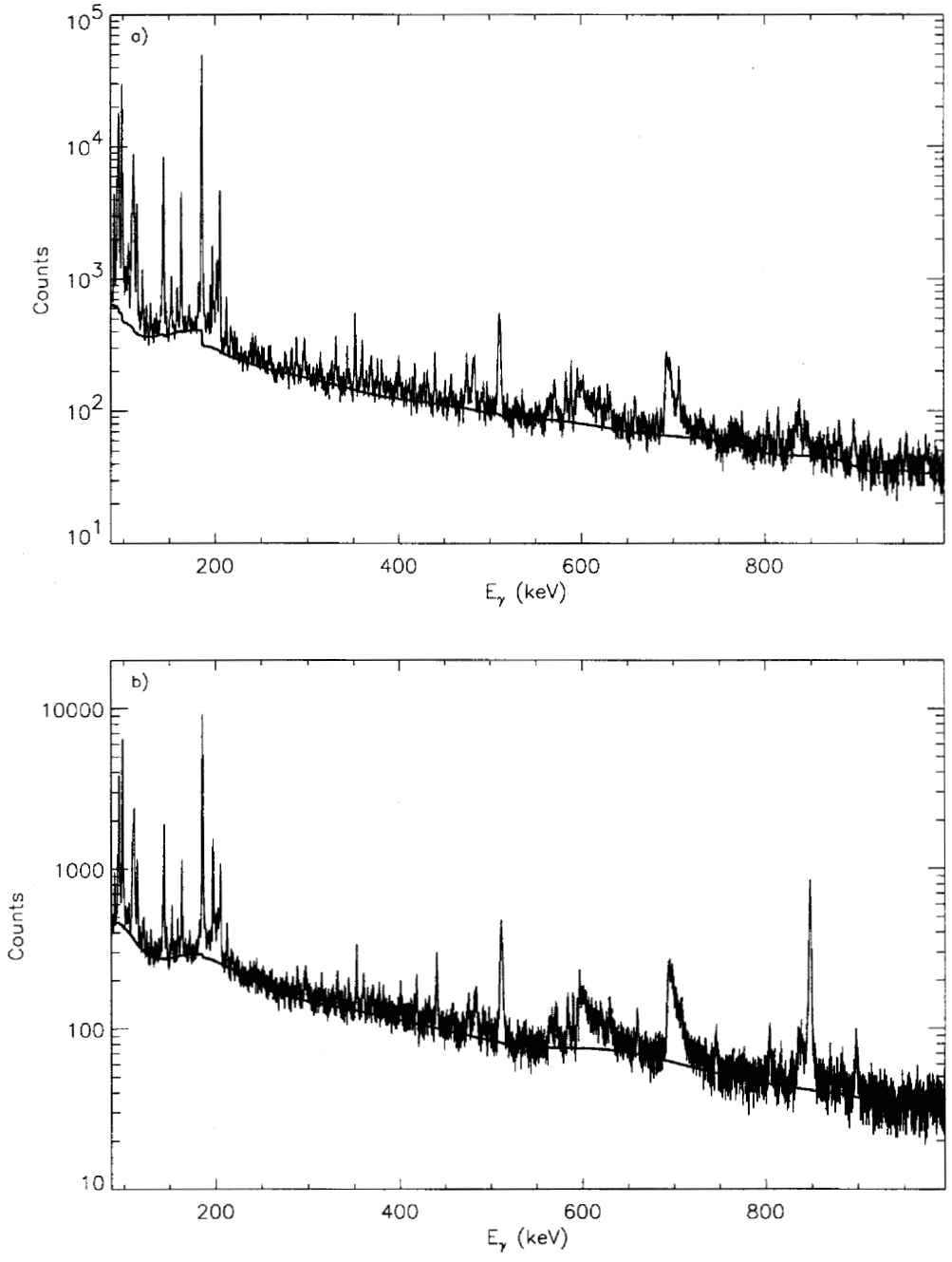

FIG. 107: Background used in the XGAM fit of bin 15 ($\overline{E}_n$ = 8.1 MeV) for the a) **98Thin** and b) **99Thin** γ-ray spectra.

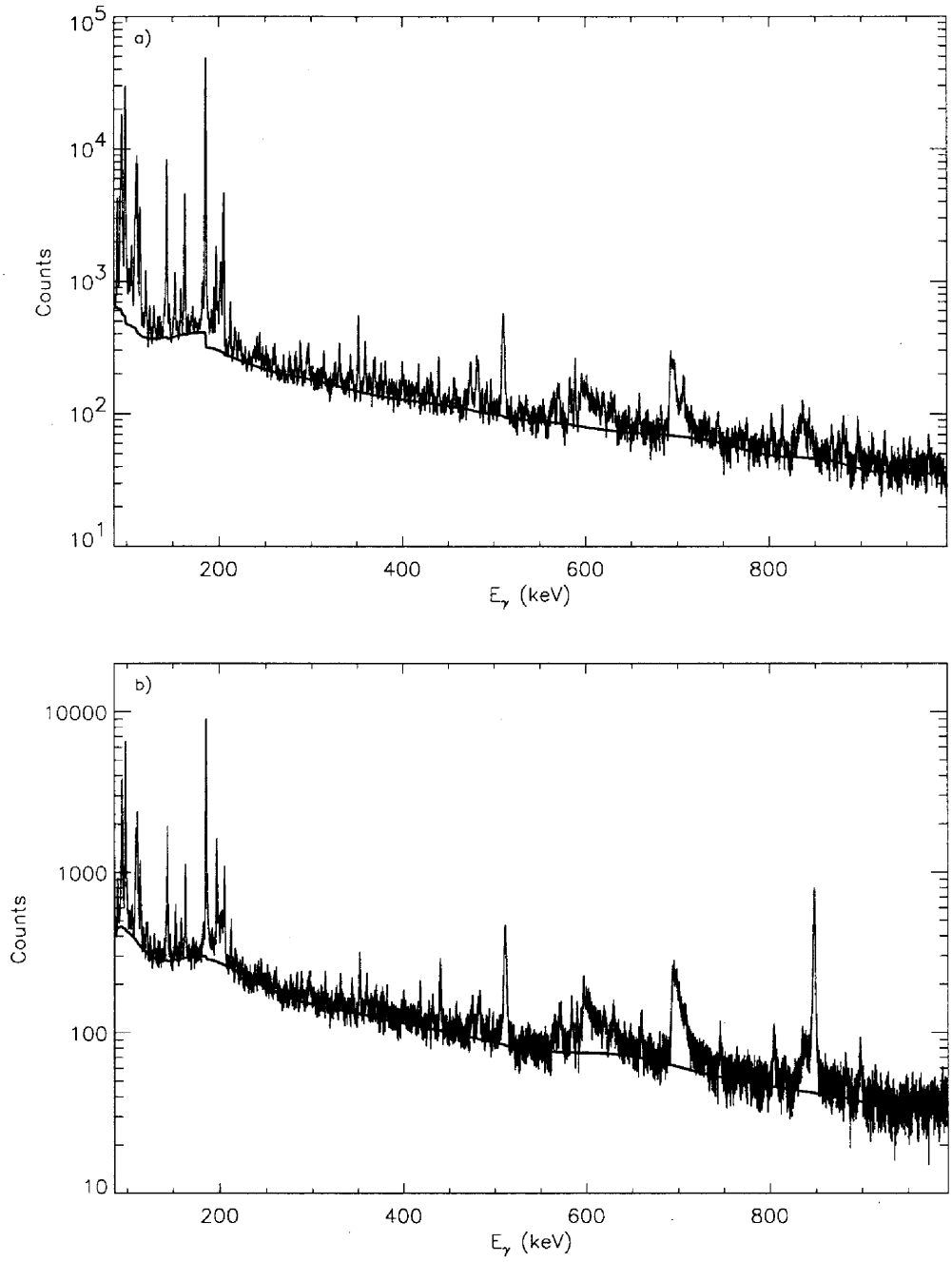

FIG. 108: Background used in the XGAM fit of bin 16 ($\overline{E}_n$ = 8.6 MeV) for the a) **98Thin** and b) **99Thin** γ–ray spectra.

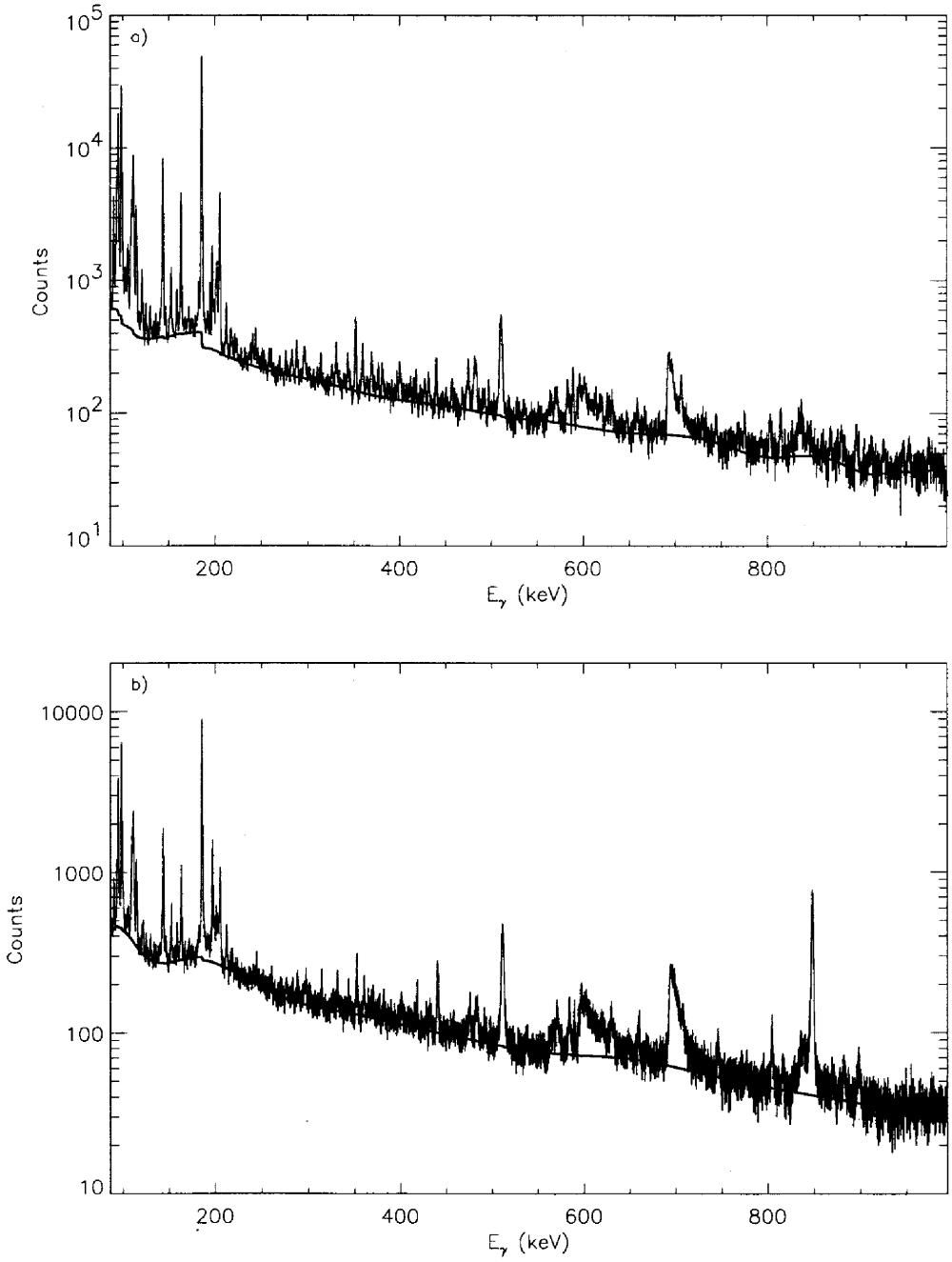

FIG. 109: Background used in the XGAM fit of bin 17 ($\overline{E}_n$ = 9.2 MeV) for the a) **98Thin** and b) **99Thin** γ–ray spectra.

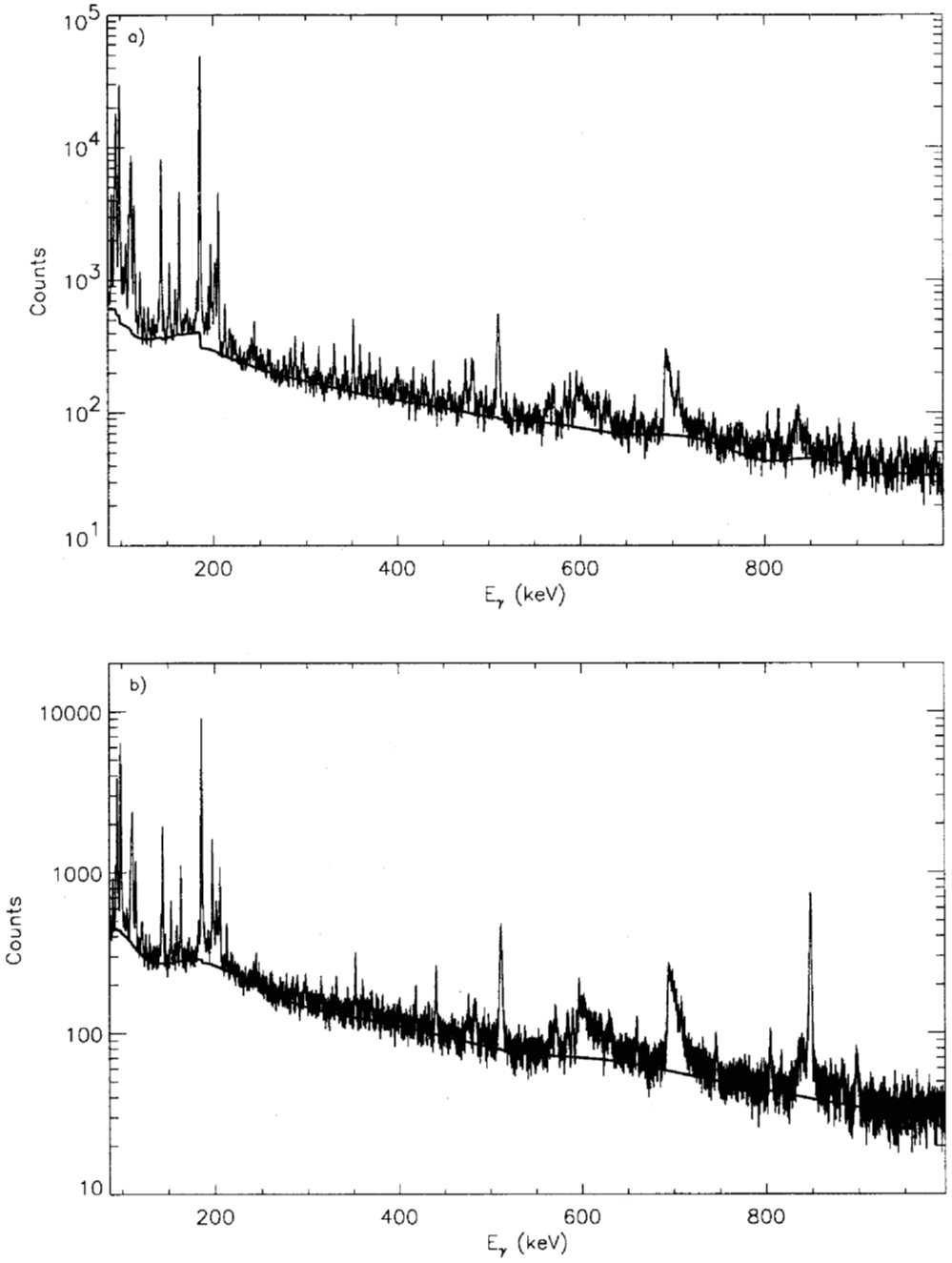

FIG. 110: Background used in the XGAM fit of bin 18 ($\overline{E}_n$ = 9.8 MeV) for the a) **98Thin** and b) **99Thin** γ–ray spectra.

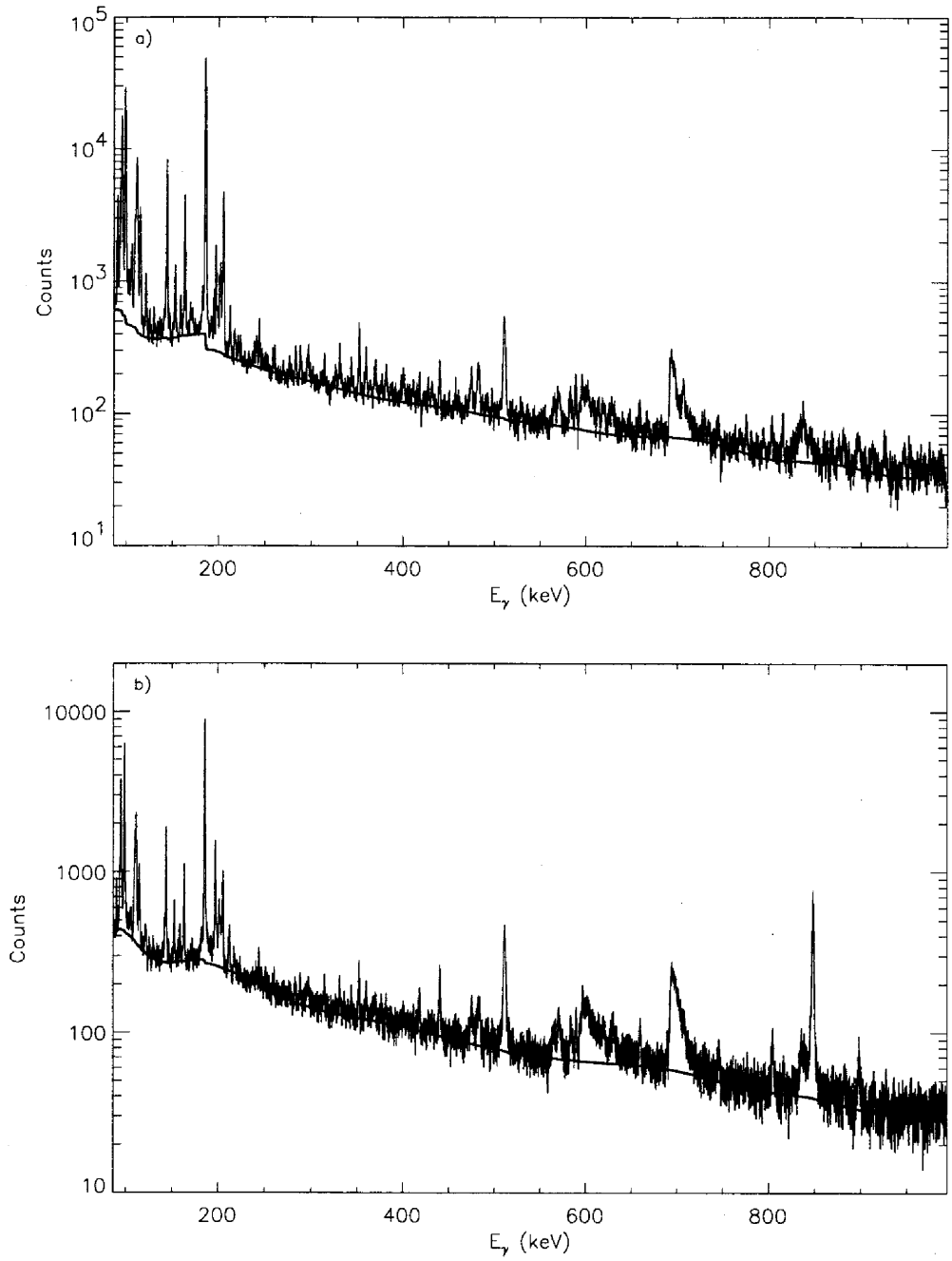

FIG. 111: Background used in the XGAM fit of bin 19 ($\overline{E}_n$ = 10.4 MeV) for the a) **98Thin** and b) **99Thin** γ–ray spectra.

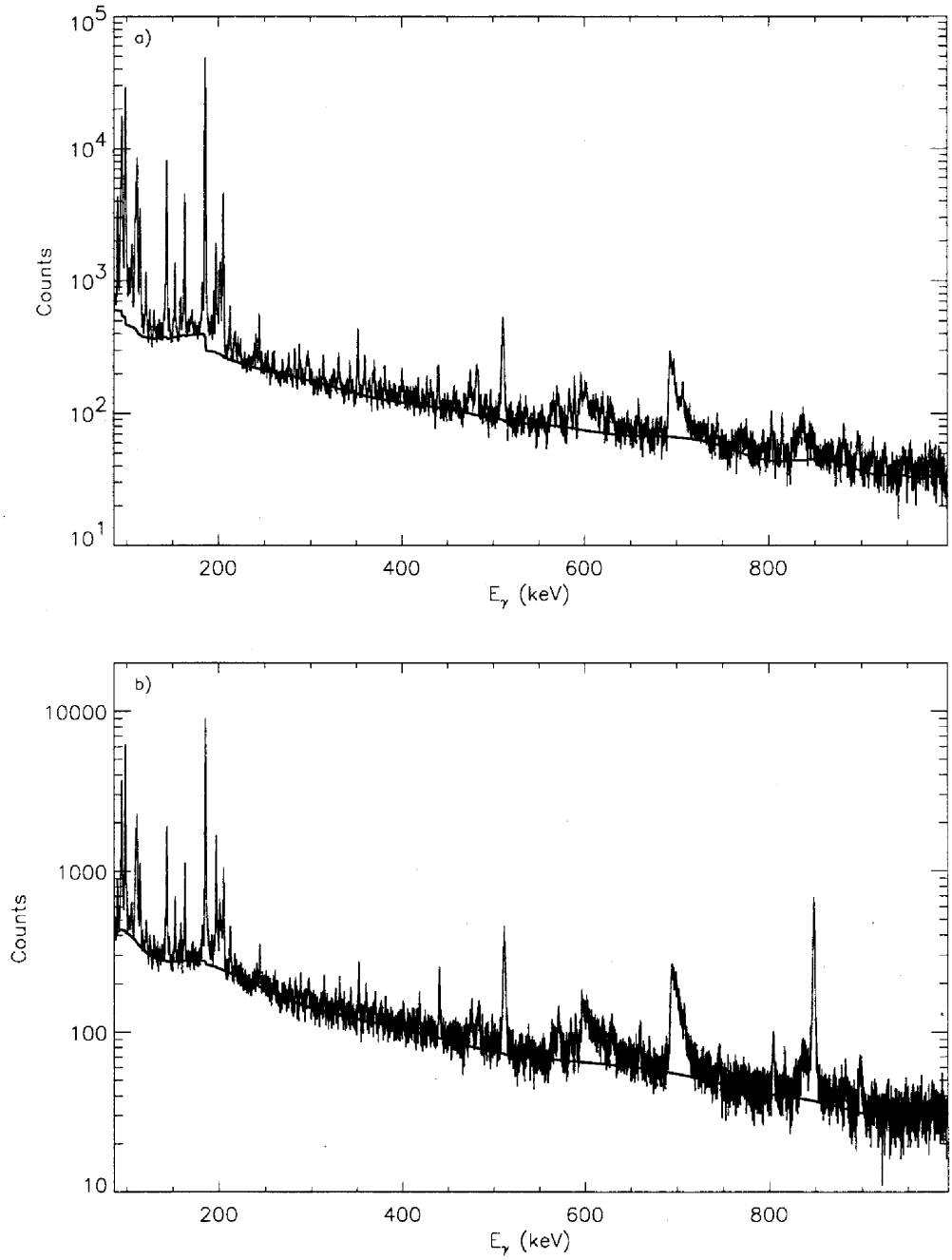

FIG. 112: Background used in the XGAM fit of bin 20 ($\overline{E}_n$ = 11.1 MeV) for the a) **98Thin** and b) **99Thin** γ–ray spectra.

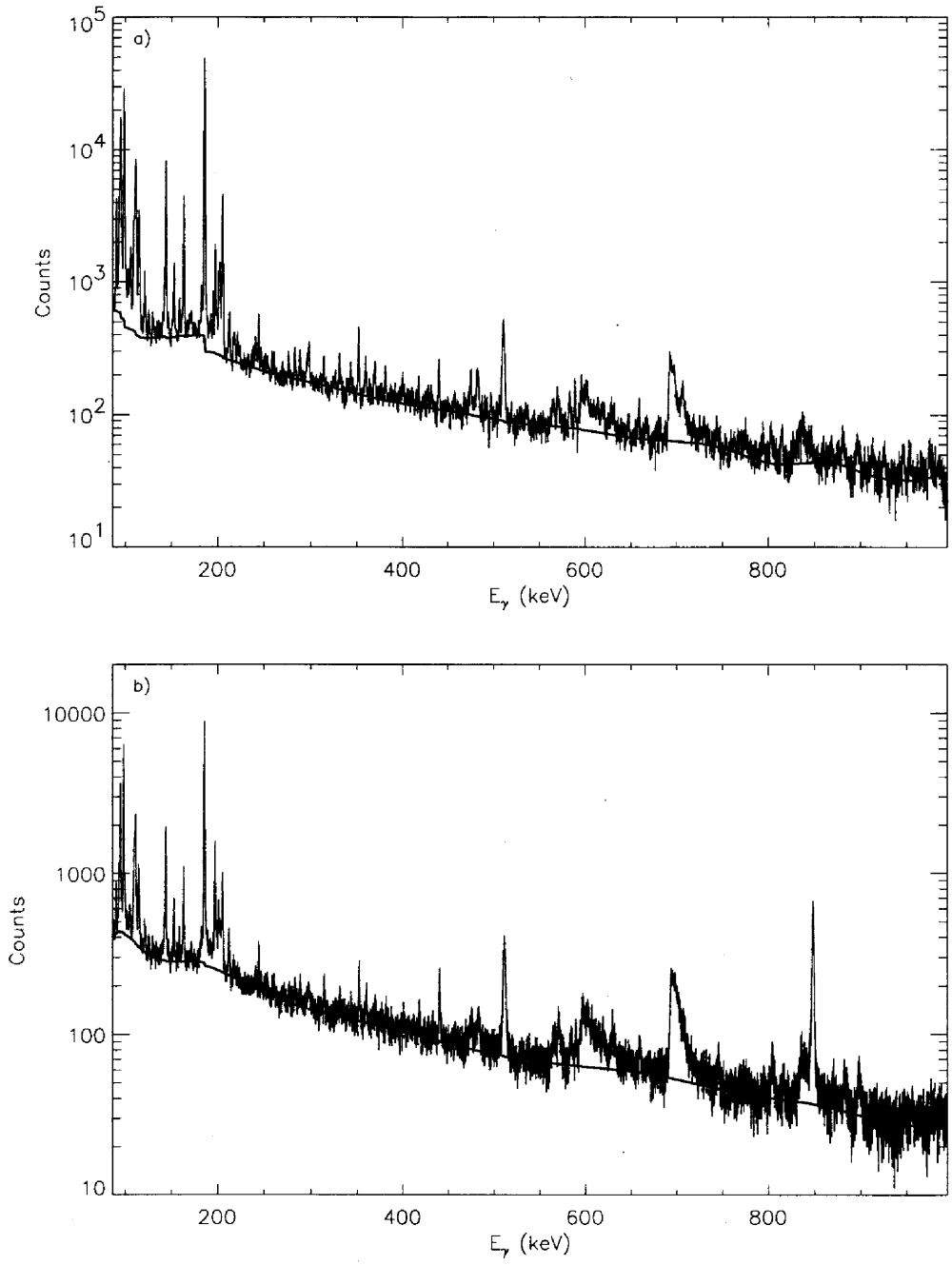

FIG. 113: Background used in the XGAM fit of bin 21 ($\overline{E}_n$ = 12.0 MeV) for the a) **98Thin** and b) **99Thin** γ–ray spectra.

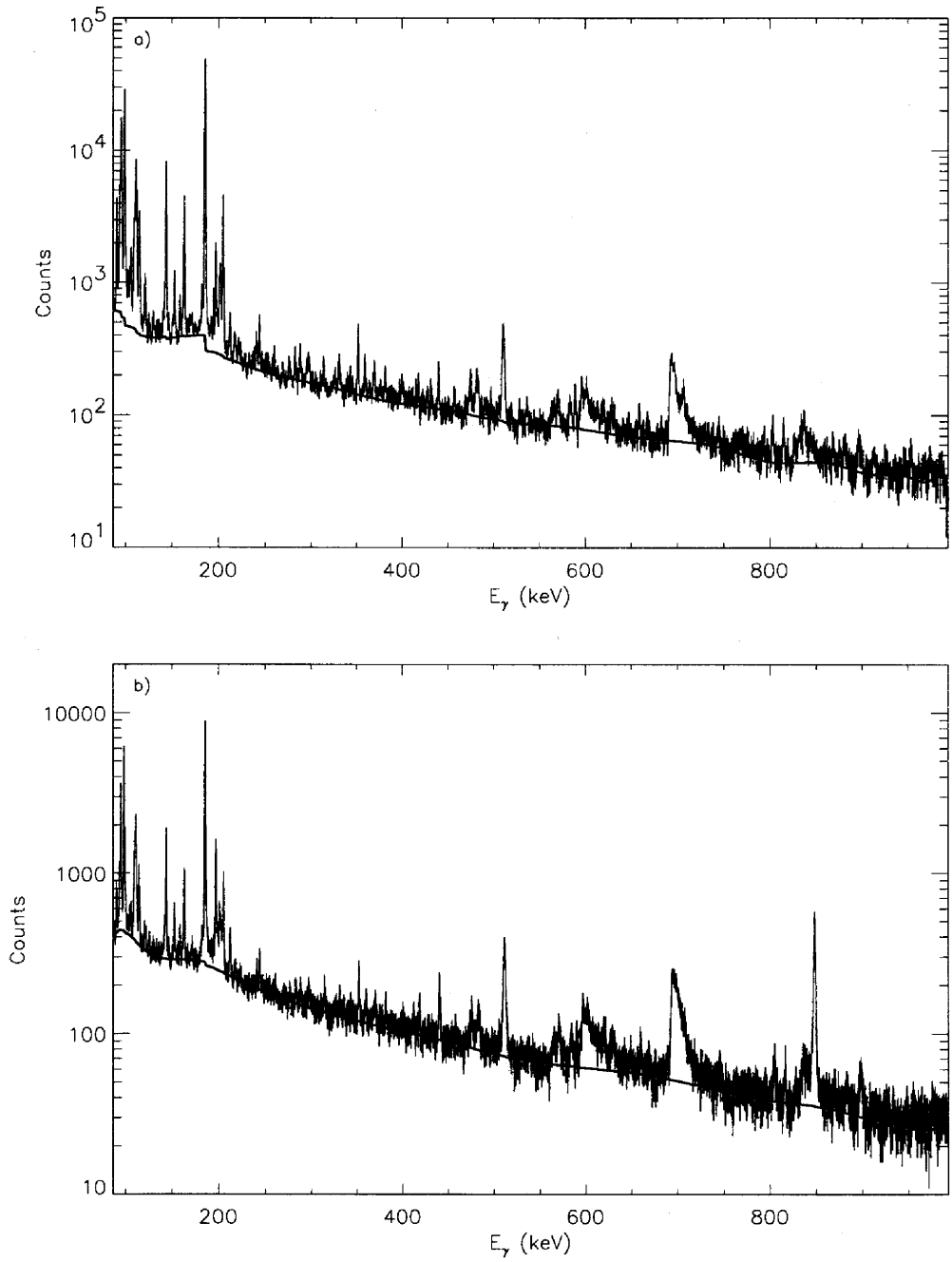

FIG. 114: Background used in the XGAM fit of bin 22 ($\overline{E}_n$ = 12.9 MeV) for the a) **98Thin** and b) **99Thin** γ–ray spectra.

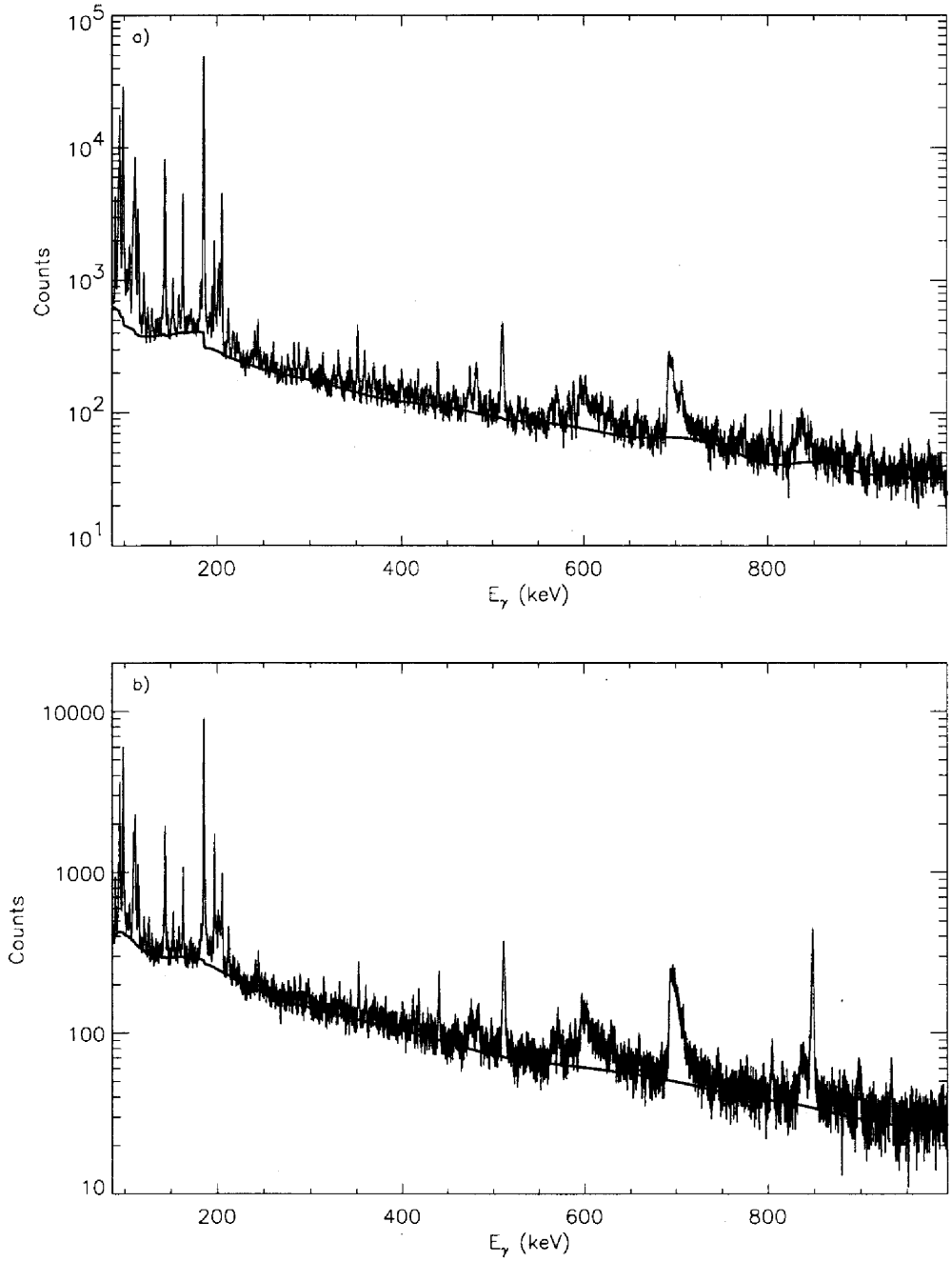

FIG. 115: Background used in the XGAM fit of bin 23 ($\overline{E}_n$ = 13.9 MeV) for the a) **98Thin** and b) **99Thin** γ–ray spectra.

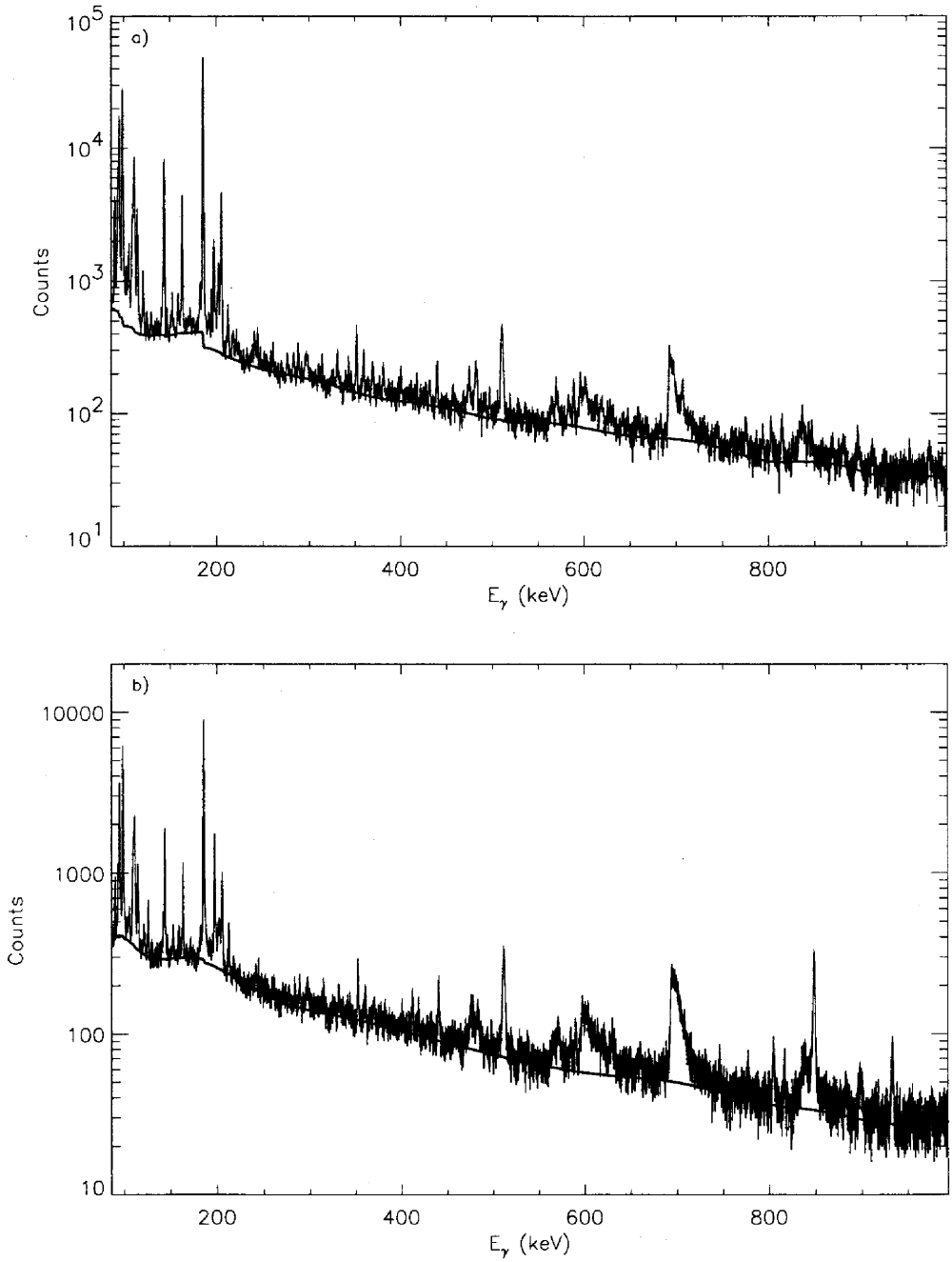

FIG. 116: Background used in the XGAM fit of bin 24 ($\overline{E}_n$ = 15.0 MeV) for the a) **98Thin** and b) **99Thin** γ–ray spectra.

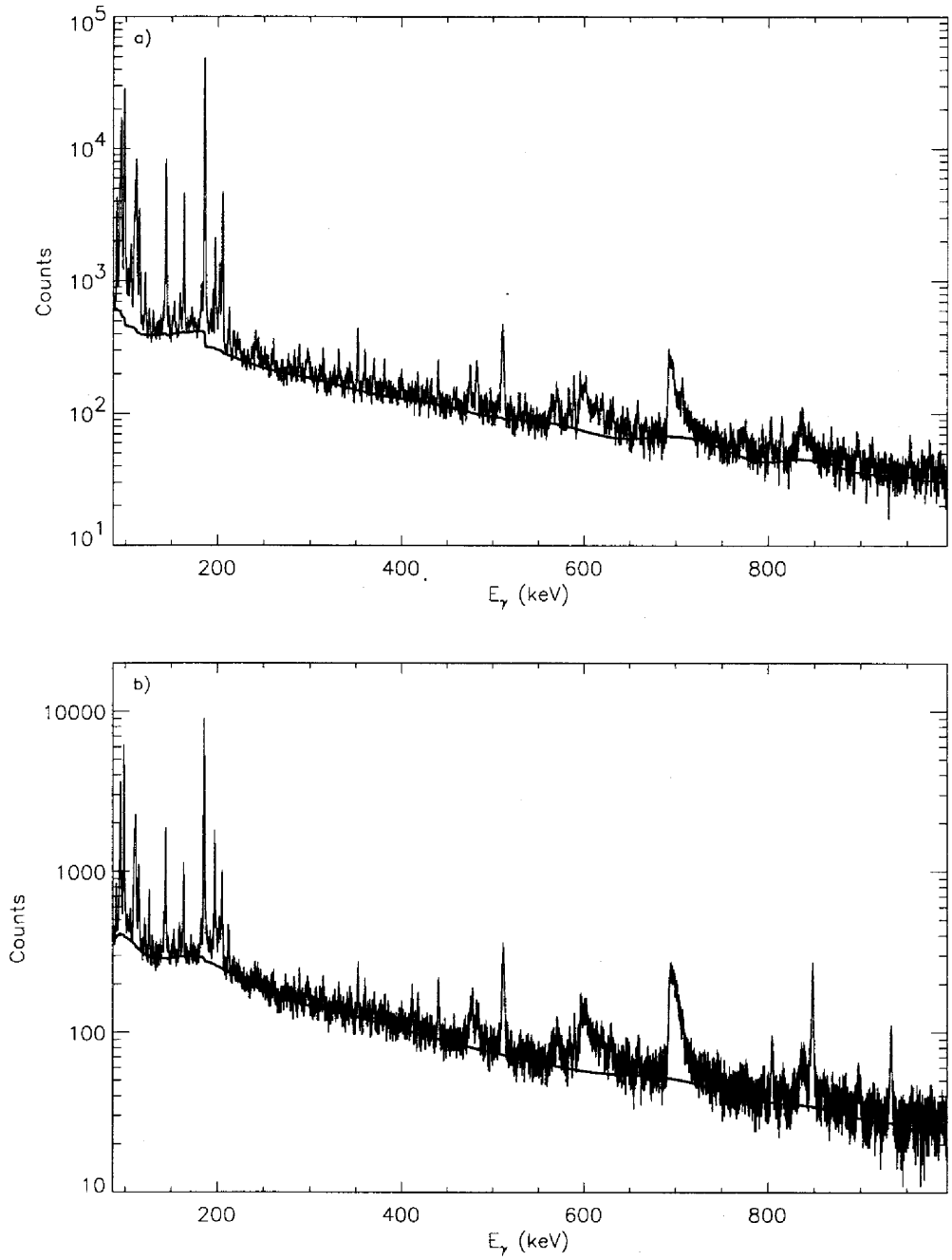

FIG. 117: Background used in the XGAM fit of bin 25 ($\overline{E}_n$ = 16.3 MeV) for the a) **98Thin** and b) **99Thin** γ–ray spectra.

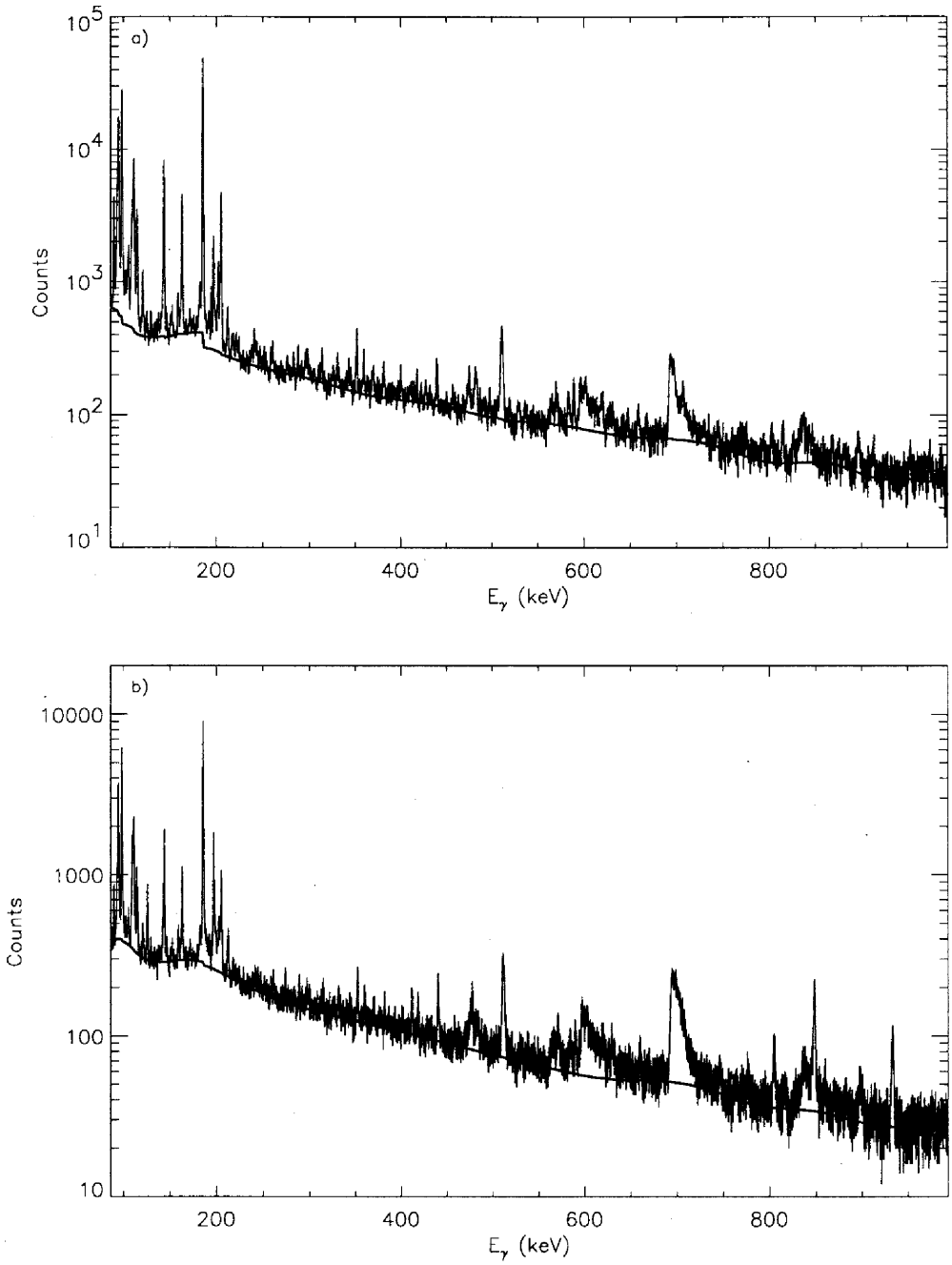

FIG. 118: Background used in the XGAM fit of bin 26 ($\overline{E}_n$ = 17.8 MeV) for the a) **98Thin** and b) **99Thin** γ–ray spectra.

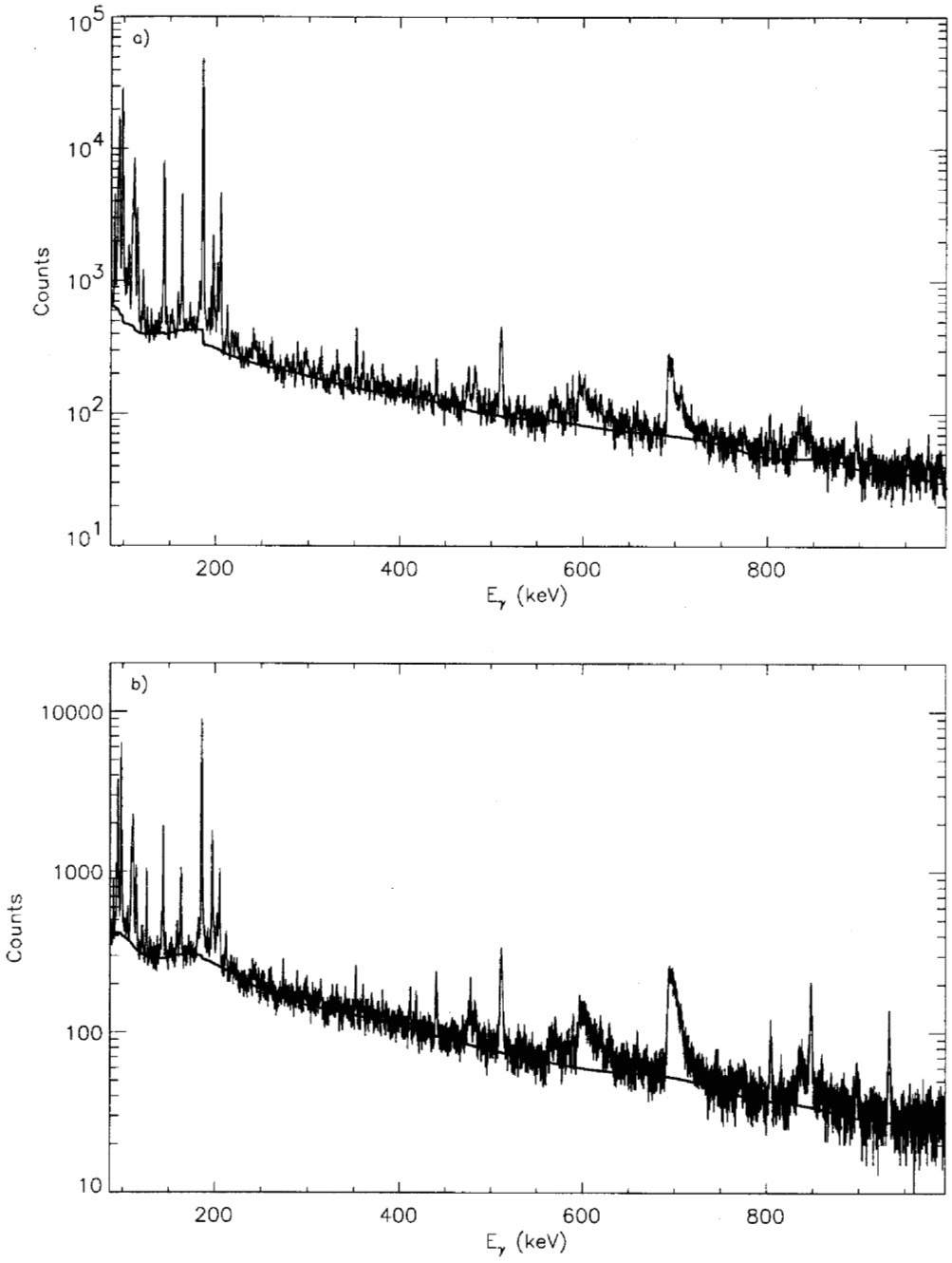

FIG. 119: Background used in the XGAM fit of bin 27 ($\overline{E}_n$ = 19.4 MeV) for the a) **98Thin** and b) **99Thin** γ–ray spectra.

University of California
Lawrence Livermore National Laboratory
Technical Information Department
Livermore, CA 94551